1. AGENCY USE ONLY (Leave blank)	2. REPORT DATE 10 Sep 95	3. REPORT TYPE AND DATES COVERED

4. TITLE AND SUBTITLE
Calibration of The Scanning Spectral Polarimeter and
Measurement of The Sky Light Polarization

5. FUNDING NUMBERS

6. AUTHOR(S)
Vincent T. Ries

7. PERFORMING ORGANIZATION NAME(S) AND ADDRESS(ES)

AFIT Students Attending:

Colorado State University

8. PERFORMING ORGANIZATION REPORT NUMBER

95-100

9. SPONSORING/MONITORING AGENCY NAME(S) AND ADDRESS(ES)
DEPARTMENT OF THE AIR FORCE
AFIT/CI
2950 P STREET, BLDG 125
WRIGHT-PATTERSON AFB OH 45433-7765

10. SPONSORING/MONITORING AGENCY REPORT NUMBER

DTIC
ELECTED
OCT 1 8 1995

11. SUPPLEMENTARY NOTES

12a. DISTRIBUTION/AVAILABILITY STATEMENT
Approved for Public Release IAW AFR 190-1
Distribution Unlimited
BRIAN D. GAUTHIER, MSgt, USAF
Chief of Administration

12b. DISTRIBUTION CODE
F

13. ABSTRACT (Maximum 200 words)

19951017 161

DTIC QUALITY INSPECTED 5

14. SUBJECT TERMS			15. NUMBER OF PAGES 104
			16. PRICE CODE

17. SECURITY CLASSIFICATION OF REPORT	18. SECURITY CLASSIFICATION OF THIS PAGE	19. SECURITY CLASSIFICATION OF ABSTRACT	20. LIMITATION OF ABSTRACT

THESIS

CALIBRATION OF THE SCANNING SPECTRAL POLARIMETER AND MEASUREMENT OF THE SKY LIGHT POLARIZATION

Submitted by

Vincent T. Ries

Department of Atmospheric Science

In partial fulfillment of the requirements

for the degree of Masters of Science

Colorado State University

Fort Collins, Colorado
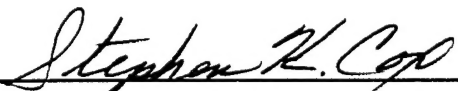
Fall 1995

COLORADO STATE UNIVERSITY

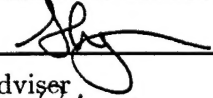JULY 17, 1995

WE HEREBY RECOMMEND THAT THE THESIS PREPARED UNDER OUR SU-PERVISION BY VINCENT T. RIES ENTITLED CALIBRATION OF THE SCANNING SPECTRAL POLARIMETER AND MEASUREMENT OF THE SKY LIGHT POLAR-IZATION BE ACCEPTED AS FULFILLING IN PART REQUIREMENTS FOR THE DEGREE OF MASTERS OF SCIENCE.
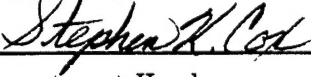
Committee on Graduate Work

Committee Member

Committee Member

Committee Member

Adviser

Department Head

ii

ABSTRACT OF THESIS

CALIBRATION OF THE SCANNING SPECTRAL POLARIMETER AND
MEASUREMENT OF THE SKY LIGHT POLARIZATION

The Scanning Spectral Polarimeter (SSP) measures 6 optical properties: flux, unpolarized radiance, and four polarized radiances (parallel, perpendicular, right hand circular, and left hand circular) through the spectral region from 400 nm - 4000nm. The SSP was designed for the measurement of reflected sunlight and a complete description is provided. This thesis asses the ability of the SSP to measure the clear sky spectral polarization. Initial calibration procedures and results are discussed. Instrument characteristics are provided to include, field of view, transmission function for the diffuse channel, and detector calibration coefficients.

A plane polarized radiative transfer model is used to study the effects local conditions have on the sky light polarization. The impacts of changing Rayleigh optical depth, surface albedo, solar position, and haze loading are examined. The SSP is used to measure the spectral sky light polarization and the results are compared to those values predicted by the model. The SSP can determine sky light polarization to within 10% error with respect to the model predictions and was capable of resolving the effects aerosol scattering and surface reflection have on sky polarization.

Vincent T. Ries
Department of Atmospheric Science
Colorado State University
Fort Collins, Colorado 80523
Fall 1995

ACKNOWLEDGEMENTS

I would like to thank Dr. Greame Stephens and the rest of my graduate committee, Dr. Stephen Cox and Dr. Roger Hoffer for their time and help.

I would like thank the members of the Stephens research group: Bob McCoy, Kirk Fuller, Paul Stackhouse, Tim Schneider, Philip Gabriel and Ian Wittmeyer for their help and sometimes redirection.

I also thank the United States Air Force for allowing me the opportunity to complete this research.

Most importantly, I thank my wife and family, Sharron, Nicole, Colleen, Kristen and Blaine for their tolerance, patience, and understanding.

CONTENTS

LIST OF FIGURES

LIST OF TABLES

Chapter 1

INTRODUCTION

1.1 Motivation

The earth's climate is controlled by the spatial and temporal variations of radiation received from the sun. Incoming solar radiation is balanced by energy that is reflected and emitted from the earth-atmosphere system. Variations in outgoing radiation are predominately influenced by clouds, whose temporal and spatial variations are not well understood. Even less understood are the radiative transfer properties of clouds (Takano and Liou, 1989) and how these properties relate to cloud microphysics and ultimately to radiative heating and cooling (Tsay et al., 1994).

Because of the complexities in modeling the radiation/cloud interaction there is a requirement for high quality, high resolution, spectral observations of cloud and aerosol properties which can be used to determine areas where our understanding is lacking. It is also important to compare albedos at both visible and selected near infrared windows as this relationship provides microphysical information including particle size (Nakajima and King, 1990) and (Stackhouse et al., 1994).

Sky light intensity and polarization calculations were pioneered by Chandrasekhar and Ebert (1954). The first studies involved only Rayleigh scattering. As computer power increased, methods were developed that included scattering from large spherical particles (Dave, 1970), then haze and aerosols (Kattawar et al., 1976), (Hitzfelder et al., 1976), and (Dave, 1978).

Coulson (1977) used skylight measurements to determine atmospheric turbidity. The effects on sky intensity and polarization from haze, ice crystal precipitation, and volcanic clouds have been studied by Bellver (1988), Fitch and Coulson (1983), and Coulson

(1983). The polarization and intensity of sky light from the zenith sky has been used to determine upper tropospheric and stratospheric turbid layers (Coulson, 1980), (Coulson, 1981), and (Beiying and Lu, 1988).

Interest in sky light intensity and polarization has again peaked with the advent of the Polarization and Directionality of Earth's Reflectances (POLDER) experiment that will fly on the Advanced Earth Observing System (ADEOS) satellite, scheduled to launch in 1996 (Deschamps et al., 1994). In preparation for this experiment an airborne version of the POLDER began flying in 1990. Data from the airborne version of POLDER have been used to estimate aerosol loading (Deuze et al., 1993), determine liquid phase of cloud particles, and derive cloud top altitude (Goloub et al., 1994).

1.2   Why the Scanning Spectral Polarimeter?

An instrument was developed that is capable of measuring the spectral properties of solar and near-IR radiation reflected from clouds at a resolution fine enough to adequately describe the spatial variation of this energy reflectance. The Scanning Spectral Polarimeter (SSP) provides radiance measurements as a function of wavelength from 400 nm through 4000 nm. As presently configured the SSP provides spectral measurements which are unique to the remote sensing of cloud, aerosol, and land surfaces in the solar wavelengths. From these data, the SSP will provide a wealth of information. The spectral nature of the data provides information on cloud optical depth and effective sizes of cloud water and ice particles (Stackhouse and Stephens, 1991). The polarization measurements are useful in determining cloud optical depth and microphysical properties. From the reflected and transmitted radiances, the fluxes of cloud and aerosol layers may be determined (Nakajima and King, 1990). The high resolution of radiance data will help in studying the spatial structure of cloud systems.

1.3   Research Objective

The SSP was constructed to measure the spectral and polarimetric reflected sunlight. The objective of this thesis is to assess the ability of the SSP to measure the spectral sky polarization to include:

1. Perform an initial calibration of the SSP to enable the observation of sky light polarization.

2. Evaluate the performance of the SSP in measuring the sky light polarization.

Part 1 was broken into three steps; installation of the polarization cubes, characterization of the optics, and determining the detector response to incident light. Part 2 involves the design of an experiment to measure the sky polarization with the SSP, using a polarized radiative transfer model to study the effects local conditions have on skylight polarization, and comparing the SSP measured sky light polarization with that predicted by the radiative transfer model.

1.4   Thesis Outline

Chapter 2 describes the design and specifications of the SSP and its data acquisition system. In Chapter 3 the optics installation and calibration procedures are discussed. The model used to predict the sky light intensity and polarization is described in Chapter 4 as well as the effects of Rayleigh optical depth, surface albedo, solar zenith angle, and haze loading. In Chapter 5 the measured sky light polarization is compared to the model predicted values.

Chapter 2

INSTRUMENT DESIGN

The Scanning Spectral Polarimeter (SSP) is a third generation radiometer which utilizes a rotating optical bandpass filter to measure the spectral region from 400 nm through 4000 nm with Half Bandwidths (HBW) of less than 17 nm to 60 nm. Earlier versions of this instrument are described by Stephens and Scott (1985) and Scott and Stephens (1985). Six optical channels allow the measurement of flux, unpolarized radiance, and the four polarized radiances: parallel, perpendicular, right hand circular, and left hand circular. The optical layout of the instrument, a brief discussion of the electronics and control systems, and the data rate and its format are described in this chapter.

2.1 Radiometer Overview

A photograph of the instrument is shown in Figure 2.1 and the instrument layout is shown in Figure 2.2. The instrument is composed of 3 main components, the motor drive assembly (A), a filter wheel and detector assembly (B), and the optics assembly (C). The optics are held in a vacuum to reduce the hazard of thermal shock and condensation problems. The modular feature of the instrument design offers a number of advantages, including the ability to use different optical assemblies (say with or without polarization optics) or different filter arrangements. A more detailed discussion of each of these main components is now presented.

2.2 The Optics Assembly

An expanded view of the optical configuration of the SSP is shown in Figure 2.3. Radiation enters the instrument through one of 6 windows which are more clearly shown in Figure 2.1, passes through the optical head where it is focused onto the Circular Variable
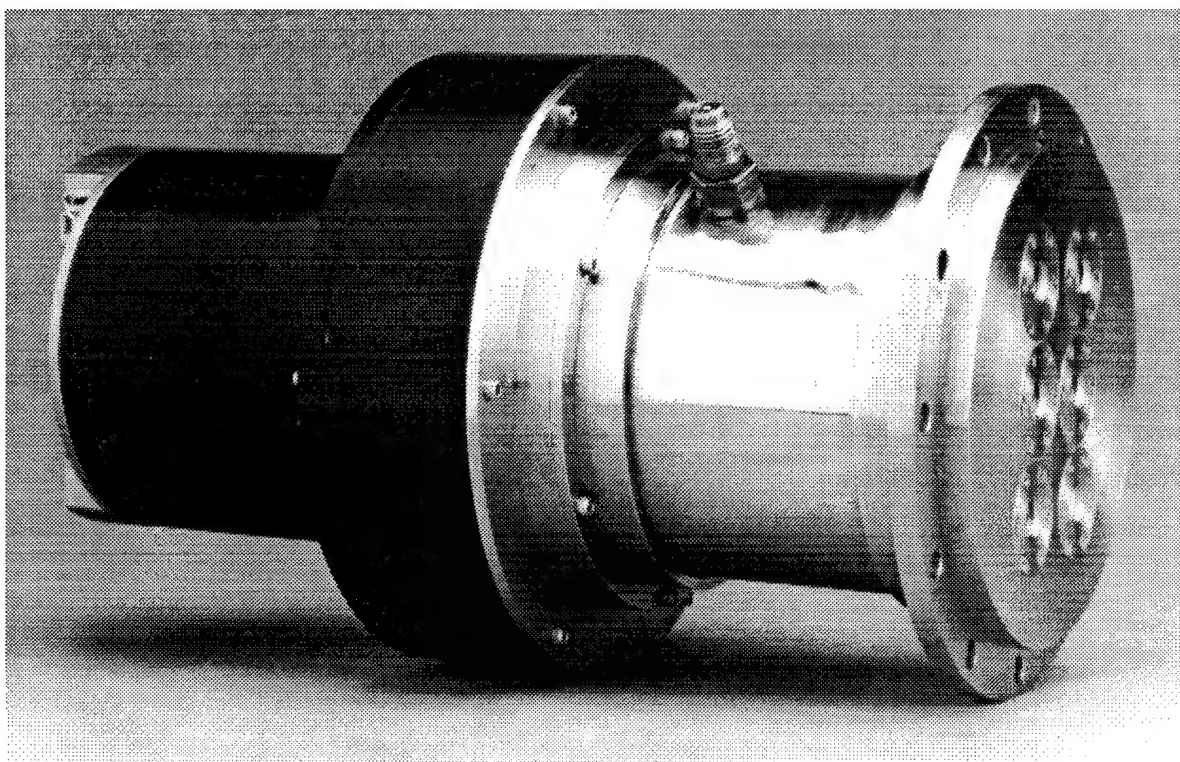
Figure 2.1: Scanning spectral polarimeter instrument head. The six windows through which radiation enters the instrument head are shown on the right. The valve on the top of the instrument is for evacuating the vacuum chamber. Cables attach to the back of the instrument shown on the left. Overall dimensions: 6 inch diameter and 10.5 inches long.

Filter (CVF) wheel, then through the field stop, and onto the detector assembly. The field stop is designed to underfill the detectors. The polarization and focusing optics are held in an optical tower, which allows each of the optics to be individually positioned. Radiation of different wavelengths will focus at different places since the index of refraction varies with wavelength. Achromatic focusing lenses are used to reduce this effect. Glan-Taylor polarization cubes are used instead of the more common Glan-Thompson. Glan-Taylors have the same optical configuration as the Glan-Thompson, except Glan-Taylors are air spaced instead of being cemented together. This reduces the thermal shock hazards.

The optics of the two circular polarization channels (5 and 6) are characterized by a fused silica window through which radiation enters the instrument. Radiation then travels through a Fresnel Rhomb and a Glan-Taylor polarization cube. The Fresnel Rhomb converts circular polarized radiation into linear polarized radiation oriented at 45° to the
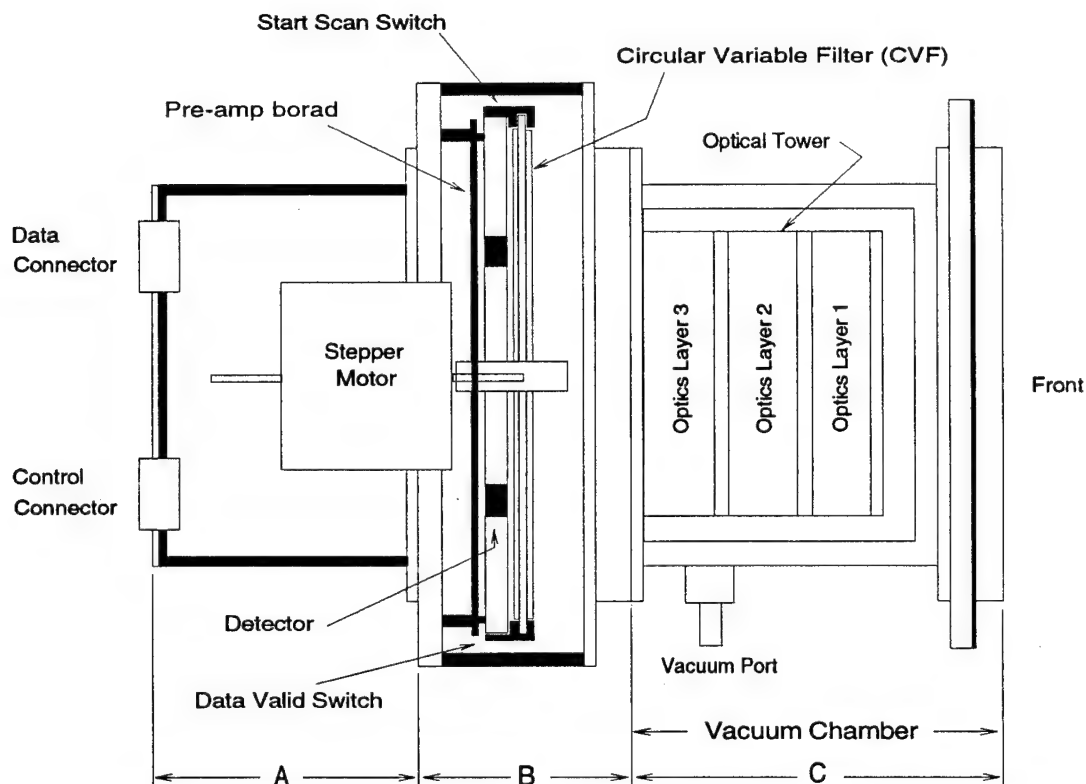
Figure 2.2: SSP components: the motor drive assembly (A), a filter wheel and detector assembly (B), and the optics assembly (C).

plane of incidence. The Glan-Taylor polarization cube transmits only the radiation that is parallel to its optical axis and this cube is oriented 45° to the left of the Fresnel Rhomb for detection of left hand circular polarized radiation and 45° to the right for detection of right hand circular polarized radiation. Radiation then travels through an achromatic focusing lens (made of BK7 optical glass), a second fused silica window as it exits the vacuum chamber, is focused onto the CVF, passes through the aperture and onto a detector.

The optics for the linear polarization channels (2 and 4) are defined by entering a fused silica window and a Glan-Taylor polarization cube so aligned to allow only perpendicular or parallel polarized light to pass. The latter is achieved by rotating the Glan-Taylor polarizing cube 90°. Radiation then travels through a BK7 achromatic focusing lens, through a second fused silica window to exit the vacuum chamber, focuses on the CVF, then through the aperture and onto the detector.
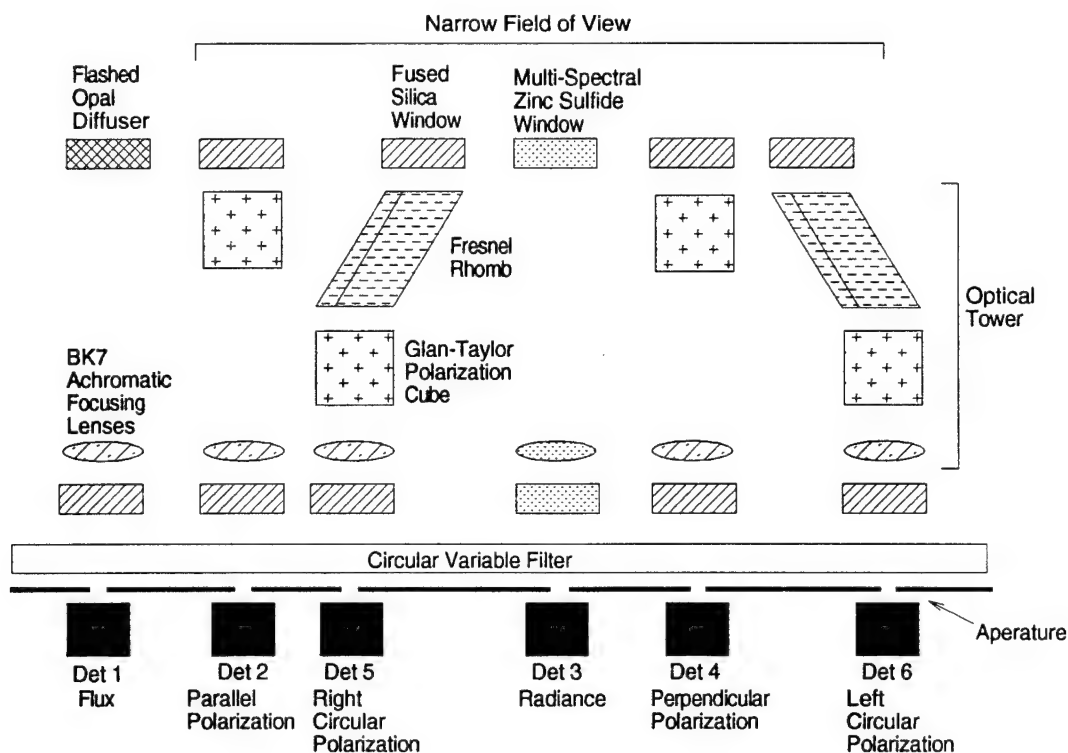
Figure 2.3: SSP optics.

The radiance channel (3) has a multi-spectral Zinc Sulfide (ZnS) window as the entrance port to the instrument, radiation then passes through a ZnS focusing lens at the bottom of the vacuum chamber and exits through a second ZnS window, focuses on the CVF, then through the aperture and onto a detector. Multi-spectral ZnS (also known as Cleartran) windows and lens are used for the path of this channel due to its flat transmission curve (approximately 70% transmission) from 400 nm - 9000 nm. The hemispheric flux channel (1) is similar to the radiance channel except that radiation enters through a flashed opal diffuser window, the entrance and exit windows are made of fused silica, and the achromatic focusing lens is made of BK7.

The radiance and polarization channels (2 - 6) all have narrow fields of view with a viewing half angle of approximately 20mRad. The diffuser in channel 1 provides a full hemispheric view.

2.3 The Filter and Detector Assembly

The CVF is made of four 90° section bandpass filters with a total bandpass of 400 nm - 4000 nm. Table 2.1 shows the nominal spectral region covered by each section and the measured spectral region for the filter sections used in this experiment. The CVFs were commercially available. Variance between the nominal and actual wavelengths is as much at 15%, and variance between individual filters with the same nominal spectral range can be as much as 5% of the central wavelength.
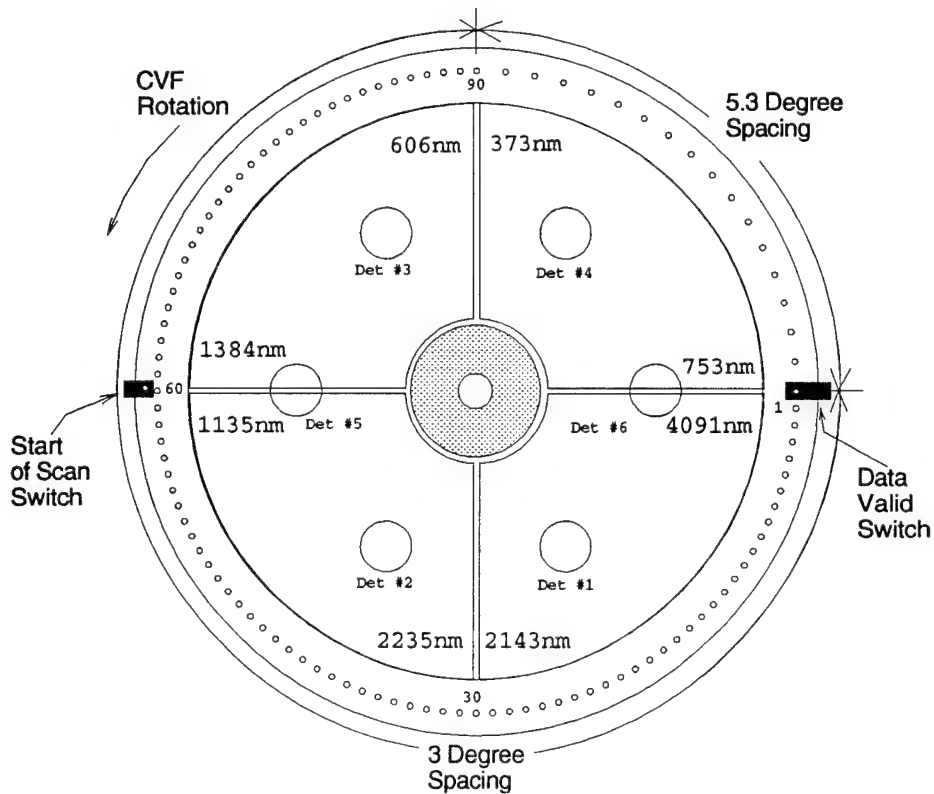
Figure 2.4: CVF wheel. The optical encoder holes and detector positions are shown. The detectors are stationary, mounted on a computer board below the CVF wheel. The CVF wheel rotates counter clock wise.

The CVF sections are mounted on an aluminum wheel with a 0.040 inch space between each segment. The space provides a clear aperture for the broadband measurements. Index holes located on the outside rim of the aluminum wheel specify points on the filter wheel

Table 2.1: Nominal and spectral regions covered by each section of the circular variable filter (CVF).

Section	Nominal Spectral Range	Measured Spectral Range
1	400 - 700 nm	373 - 753 nm
2	700 - 1235 nm	606 - 1384 nm
3	1235 - 2225 nm	1135 - 2235 nm
4	2225 - 4000 nm	2143 - 4091 nm

where radiation data are read by the data acquisition system, this provides a custom optical encoder. A diagram of the filter sections and encoder hole locations is shown in Figure 2.4. Encoder holes were originally placed to at 5.3° intervals along the visible section (400 - 700 nm) to eliminate overlap between adjacent measurements, however, since the detectors are evenly spaced around the sensor head, this sampling pattern was only valid for detector 6. The CVF sections used provided spectral overlap between consecutive sections. The central wavelengths are listed in Appendix A for all holes on the CVF as a function of index hole number and position around the filter wheel. Table 2.2 lists the central wavelengths from 390 - 1100 nm in ascending order. Bandwidths for each channel have not been measured, but are estimated at less than or equal to 4% of the central wavelength for sections 1 and 2, and less than 1.5% of the central wavelength for sections 3 and 4.

2.3.1 Detectors

The detectors, shown in Figure 2.5, are hybrid two color detectors with built in pre-amplifiers. A Silicon (Si) element is mounted over a Lead Selenide (PbSe) element. The Si element is used in the photovoltaic mode and the PbSe element is used in the photoconductive mode. The detector windows are also made of multispectral zinc sulfide (ZnS). The Si detector has a spectral range of 400 nm to 1100 nm with an 8 nanosecond response time. The Si element has a 50% transmission at wavelengths greater than 1100 nm. This allows radiation to pass through the element onto the PbSe detector

Table 2.2: Central wavelengths (nm) in ascending order for channels 1 - 4. * - Measurements where channels 2 - 4 all have the same central wavelength.

Value	Ch 1	Ch 2	Ch 3	Ch 4	Value	Ch 1	Ch 2	Ch 3	Ch 4
1	394	394	394	390	24	687	666.5	666.5	714
2	407	407	407	411	25	696	680	680	*719.5
3	420	420	420	432.5	26	712.5	687	687	*733
4	433	433	433	453.5	27	718	693	693	758
5	445	445	445	475	28	737.5	706	706	803.5
6	458	458	458	*496	29	761.5	712.5	712.5	848.5
7	470.5	470.5	470.5	*509	30	788.5	719.5	719.5	896
8	483	483	483	*521.5	31	814.5	733	733	943
9	496	496	496	*535	32	842	737.5	737.5	986
10	509	509	509	*548	33	867	761.5	761.5	1037
11	521.5	521.5	521.5	*561	34	892	788.5	788.5	1082
12	535	535	535	*575	35	918	814.5	814.5	
13	548	548	548	*588	36	944	842	842	
14	561	561	561	*601	37	971	867	867	
15	575	575	575	*614	38	993	892	912	
16	588	588	588	*627	39	1019	919	958	
17	601	601	601	*640	40	1041	945	1008	
18	614	614	614	*653.5	41	1077	970	1052	
19	627	627	627	*666.5	42		996	1098	
20	639	639	639	670	43		1025		
21	650	640	640	*680	44		1050		
22	664	653.5	653.5	*693	45		1077		
23	673	664	664	*706					

below. The PbSe detector has a spectral range of 1000 nm to 5200 nm with a response time of 1-3 micro-seconds. The upper wavelength limit of the PbSe element is temperature dependent.

2.3.2 Sensor Head Electronics

Figure 2.6 shows a block diagram of the SSP sensor head electronics. The circular variable filter is driven by a computer controlled stepper motor. Rotation rate can be varied from 0.1 revolution/second to 30 revolutions/second. Two optical switches are used, one to determine the start of a new scan and the second generates data valid signals from the index holes on the rim of the CVF. Signals from each of the 6 - 2 color detectors are amplified so the resulting analog signal sent to the data acquisition system varies

Figure 2.5: SSP two color detector. The Silicon element is the black square at the center of the detector. The Lead Selenide detector has two elements, a blind element shown as the white square below the Silicon element and an active element under the Silicon element. Amplifiers are mounted on the grid below the detectors. The entire setup fits in a TO-8 housing with overall dimensions of .6 inch diameter and .3 inch tall.

from 0 volts/32500 counts (no signal) to -10 volts/0 counts (max signal). Temperature is monitored at four locations: the polarization and focusing optics, the CVF air chamber, the detector block, and the motor.

2.4 Data Acquisition

The SSP is designed to use two different data acquisition systems (DAS) to collect information from the sensor head. Both systems use a micro controller that runs all timing and data handling issues. Analog signals are received from the sensor head on 16 different channels. Descriptions of the 16 data channels are listed in Table 2.3. Each of the 16 data channels has its own sampling, 16 bit analog to digital converter. After the A-D
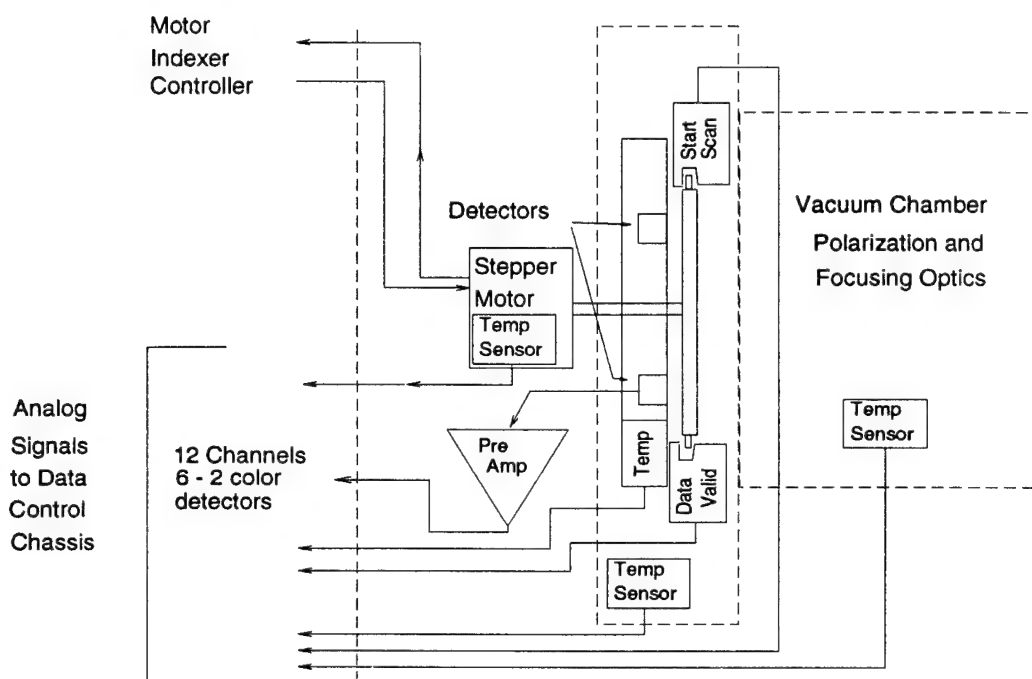
Figure 2.6: Sensor head electronics.

conversion, digital data is put into two parallel first in first out (FIFO) outputs. Two FIFO ports are provided to allow two computer systems to read the same data from the SSP data acquisition system without rewiring. A real time clock is used to flag each data scan with the acquisition time. The data pattern from the FIFO is shown in Table 2.4

The first DAS is rack mounted and was designed for manned airborne platforms, calibration, and ground testing. A block diagram of this system is shown in Figure 2.7. This system has full diagnostic outputs, real time graphical display, and large data storage capacity.

The second DAS, a small footprint system, was designed for unmanned aerospace vehicles (UAV) or experiments where unattended operation is required. This system provides no graphical output, storage capacity, or input voltage. The user must provide the input voltage, download data from the FIFO ports, and transmit or store data from the sensor head. A block diagram of this system is shown in Figure 2.8. This small footprint version does provide diagnostic output for an external computer to aid in debugging.

Table 2.3: Data channel definitions.

Data Ch.	Det.	Det. Type	Wavelength Region	Optical Properties
1	1	Si	400-1100 nm	Hemispherical
2	2	Si	400-1100 nm	Parallel Pol.
3	3	Si	400-1100 nm	Radiance
4	4	Si	400-1100 nm	Perpendicular Pol.
5	5	Si	400-1100 nm	Left Circular Pol.
6	6	Si	400-1100 nm	Right Circular Pol.
7	1	PbSe	1000-4000 nm	Hemispherical,
8	2	PbSe	1000-4000 nm	Parallel Pol.
9	3	PbSe	1000-4000 nm	Radiance
10	4	PbSe	1000-4000 nm	Perpendicular Pol.
11	5	PbSe	1000-4000 nm	Left Circular Pol.
12	6	PbSe	1000-4000 nm	Right Circular Pol.
13	Detector Block Temperature			
14	Motor Temperature			
15	CVF Air Chamber Temperature			
16	Polarizing and Focusing Optics Temperature			
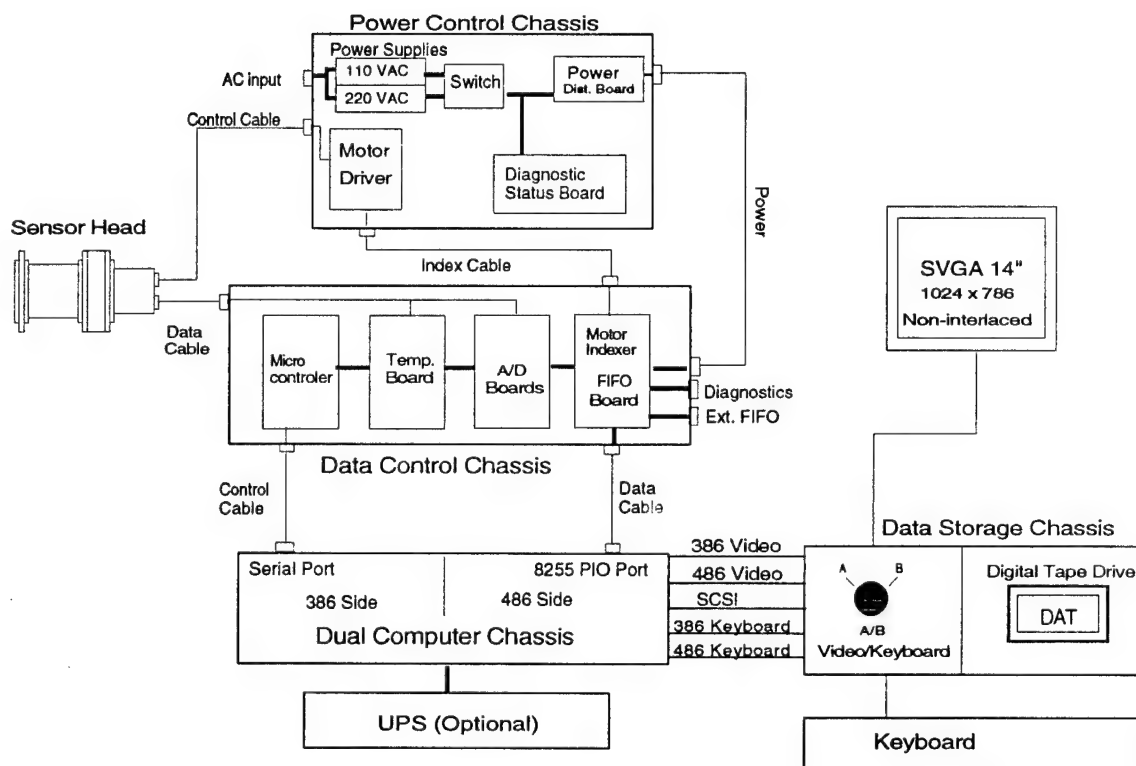
Figure 2.7: Rack mounted data acquisition system.

Table 2.4: FIFO byte pattern.

Scan Header		First of 107 Data Sets	
Byte	Description	Byte	Description
1	Clock (0.01 Seconds)	27	Ch 1 (Low Byte)
2	Clock (Seconds)	28	Ch 2 (Low Byte)
3	Clock (Minutes)	29	Ch 3 (Low Byte)
4	Clock (Hours)	30	Ch 4 (Low Byte)
5	Gain Ch 1	31	Ch 5 (Low Byte)
6	Gain Ch 2	32	Ch 6 (Low Byte)
7	Gain Ch 3	33	Ch 7 (Low Byte)
8	Gain Ch 4	34	Ch 8 (Low Byte)
9	Gain Ch 5	35	Ch 9 (Low Byte)
10	Gain Ch 6	36	Ch 10 (Low Byte)
11	Gain Ch 7	37	Ch 11 (Low Byte)
12	Gain Ch 8	38	Ch 12 (Low Byte)
13	Gain Ch 9	39	Ch 1 (High Byte)
14	Gain Ch 10	40	Ch 2 (High Byte)
15	Gain Ch 11	41	Ch 3 (High Byte)
16	Gain Ch 12	42	Ch 4 (High Byte)
17	Motor Speed (Low Byte)	43	Ch 5 (High Byte)
18	Motor Speed (High Byte)	44	Ch 6 (High Byte)
19	Temp Ch 13 (Low Byte)	45	Ch 7 (High Byte)
20	Temp Ch 14 (Low Byte)	46	Ch 8 (High Byte)
21	Temp Ch 15 (Low Byte)	47	Ch 9 (High Byte)
22	Temp Ch 16 (Low Byte)	48	Ch 10 (High Byte)
23	Temp Ch 13 (High Byte)	49	Ch 11 (High Byte)
24	Temp Ch 14 (High Byte)	50	Ch 12 (High Byte)
25	Temp Ch 15 (High Byte)		
26	Temp Ch 16 (High Byte)		
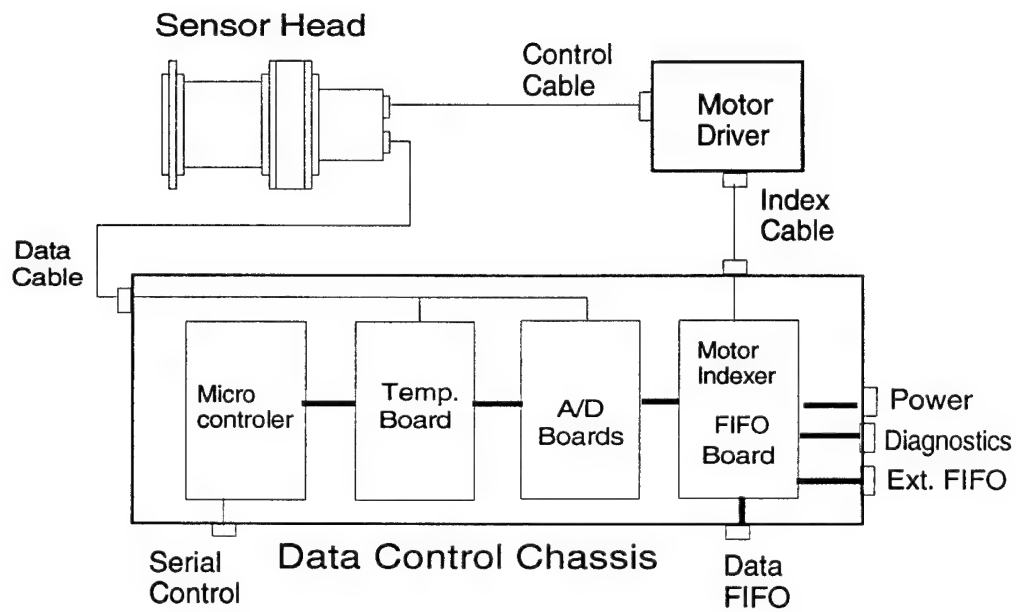
Figure 2.8: Small footprint data acquisition system.

Chapter 3

INSTRUMENT CHARACTERIZATION AND CALIBRATION

3.1 Experiment Description

For the experiments described in this thesis, only four channels were used; the radiance, irradiance, perpendicular polarization, and parallel polarizations. These channels measured radiation only from 400 - 1100 nm (data from the silicon detector) and the broadband holes at each end of the CVF section 1 (400 - 700 nm) were covered.

The first step is to install and align the polarization cubes in the SSP optical tower. The SSP must then be calibrated using a known light source. However, absolute calibration is not crucial for the experiments described here, since we are concerned with the change in sky polarization as a function of view angle. Polarization is calculated by a ratio of radiance values, so an accurate relative calibration will yield accurate polarization values. The pattern of sky polarization can then be measured and compared to the calculated pattern for a Rayleigh atmosphere. These steps will now be discussed.

3.2 Optics Alignment

The Glan-Taylor polarization cube in the perpendicular channel must be aligned 90° from the Glan-Taylor in the parallel channel. The equipment layout for this alignment exercise is illustrated in Figure 3.1. A red unpolarized 10mW Helium-Neon laser was used as the light source. The laser beam was reflected off two movable mirrors which allow easy adjustment of the laser beam. The first mirror is used to adjust the originating point of the laser beam as it reflects off the second mirror and passes through the optics tower. The second mirror adjusts the beam direction. The SSP optical tower was mounted on a jig that was built to allow the optical tower to be rotated precisely 180°. Optical channels
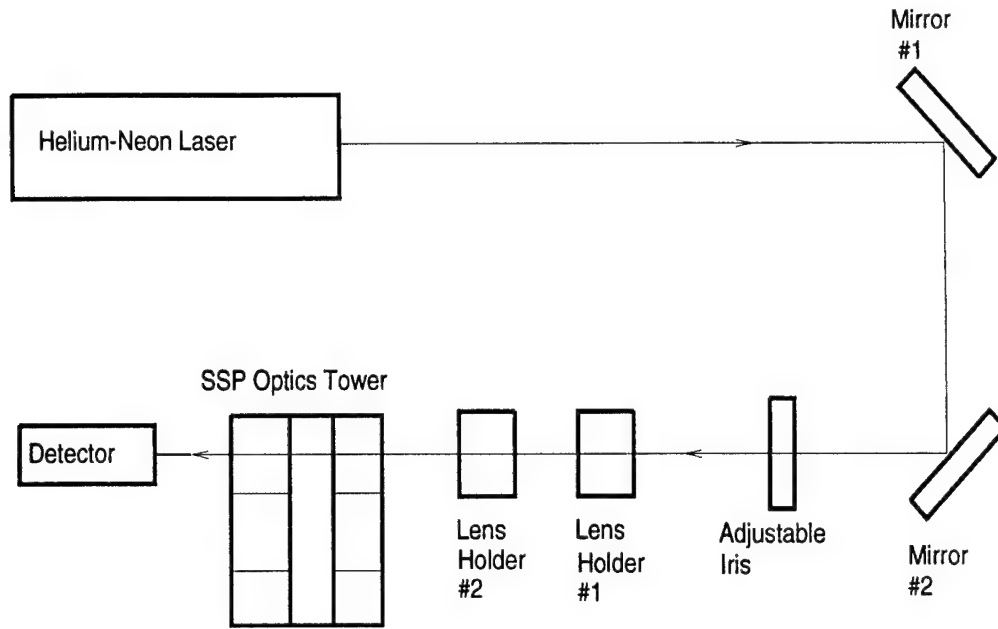
Figure 3.1: Equipment setup for Glan-Taylor polarization cube alignment.

2 and 4 are used for the perpendicular and parallel polarization so the Glan-Taylor for channel 4 is in the same location as the Glan-Taylor for channel 2 after the 180° rotation. A silicon photo detector was mounted behind the optical tower to measure the radiation transmitted through the calibration optics. Lens centering guides were built from a piece of aluminum turned down to the same diameter as the lens with a 1/8 inch hole in the center.

To install the optics, all equipment was aligned with the laser. A reference polarization cube was installed in lens holder 1 that allowed only perpendicular polarized radiation to pass. The polarization cube for channel 2 was installed in the optics tower 90° to this reference cube. The SSP Optics tower was rotated 180°. A second reference cube was installed in lens holder 2, 90° from the first. The polarization cube for channel 4 was installed 90° from the second reference cube. Final alignment of the polarization cubes was 90° ± .183°. The exact procedure used for this exercise is described further in Appendix B.

3.3 Calibration

To enable data from the SSP to be accurately related to atmospheric spectrum, the instrument must be calibrated to a standardized source. For this exercise a 1000 watt Quartz Halogen DC light bulb was used. The bulb was calibrated by Eppley Lab over the range of 250 nm to 2400 nm, traceable to NIST standards. The calibration curve for the lamp is shown in Figure 3.2. Of note are the low irradiance in the spectral region below 500 nm and the irradiance peak at 900 nm. These characteristics appear in the following calibration experiments.
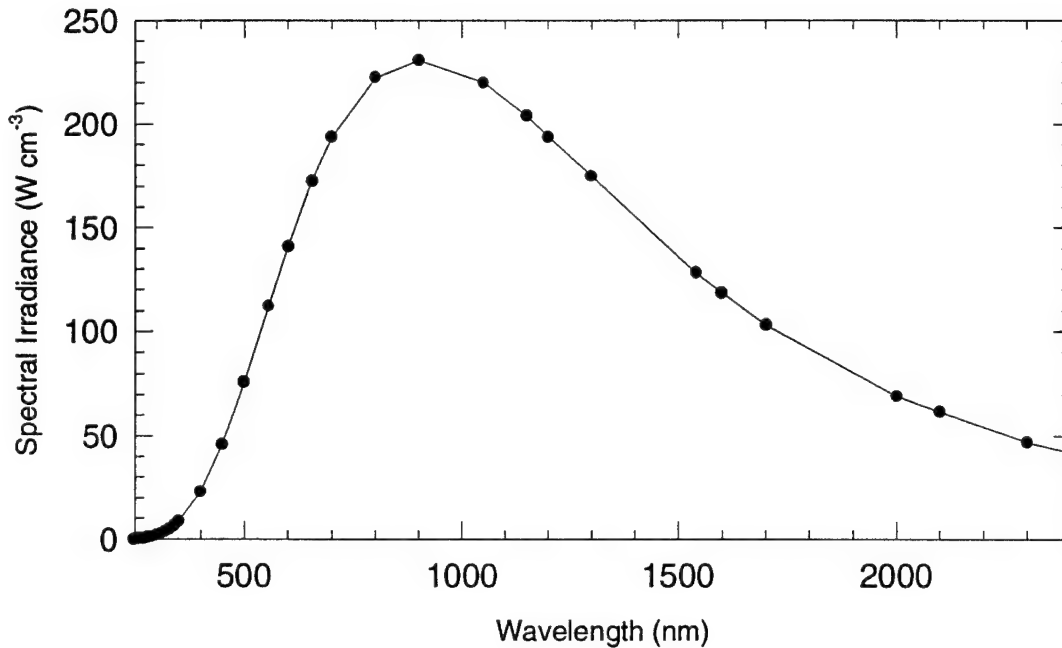
Figure 3.2: Calibration curve for the 1000 watt quartz halogen lamp.

Three different calibrations of the SSP were performed; determining the field of view (for channels 2, 3, and 4), measuring the angular response of transmission for the flashed optical diffuser in channel 1, and determining the detector response to incident spectral intensity. Procedures and results of these calibrations will now be discussed.
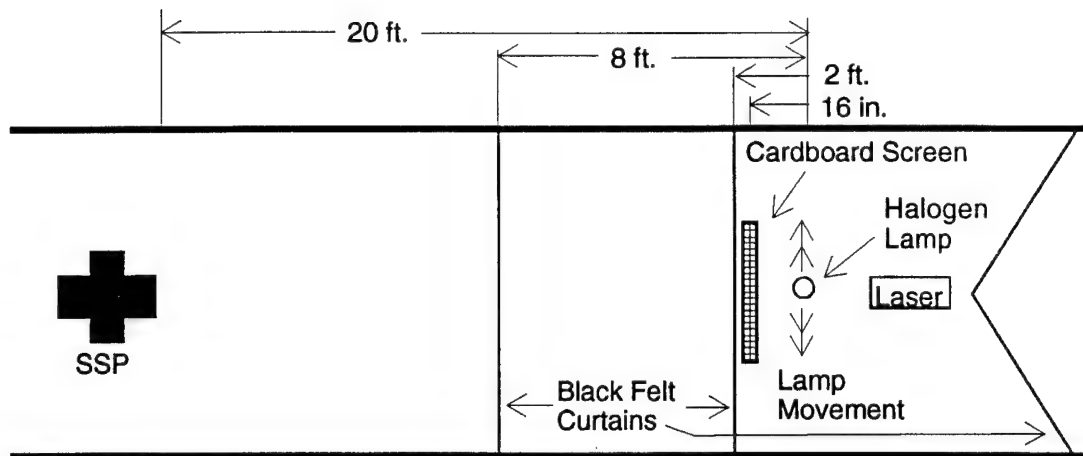
Figure 3.3: FOV measurement: Equipment layout.

3.3.1 Field of View

The equipment setup used to determine the field of view for channels 2 - 4 is illustrated in Figure 3.3. This experiment was conducted in a hallway where the distance between the SSP and the light source was 20 feet. The SSP was set on a leveling bench which consisted of a thick aluminum plate with a height adjusting screw in each corner. The light source is on scissors jack that allows the height of the bulb to be easily adjusted. The light source and jack are on a rolling bench with the wheels locked so the bench will only roll in a straight line. All equipment is leveled and aligned down the center of the hallway using the Helium-Neon laser. A cardboard screen with a 5 by 7 inch hole was attached to the rolling table. This screen moves with the light source and stops most of the reflection from the walls. To reduce reflections further, two black felt curtains were hung across the hallway with a hole cut into each curtain to allow the light from the source to reach the SSP. A black felt curtain is also hung behind the SSP to reduce the reflection from the back wall. The source light is moved perpendicular to the experiment centerline as shown in Figure 3.3. The distance from the center line and the signal intensity received at the SSP are recorded. The exact procedure used for this exercise is described further in Appendix B.

Results of measured intensity versus light source position for the radiance channel (3), are shown in Figures 3.4. This graph shows the relative power received (digital counts)
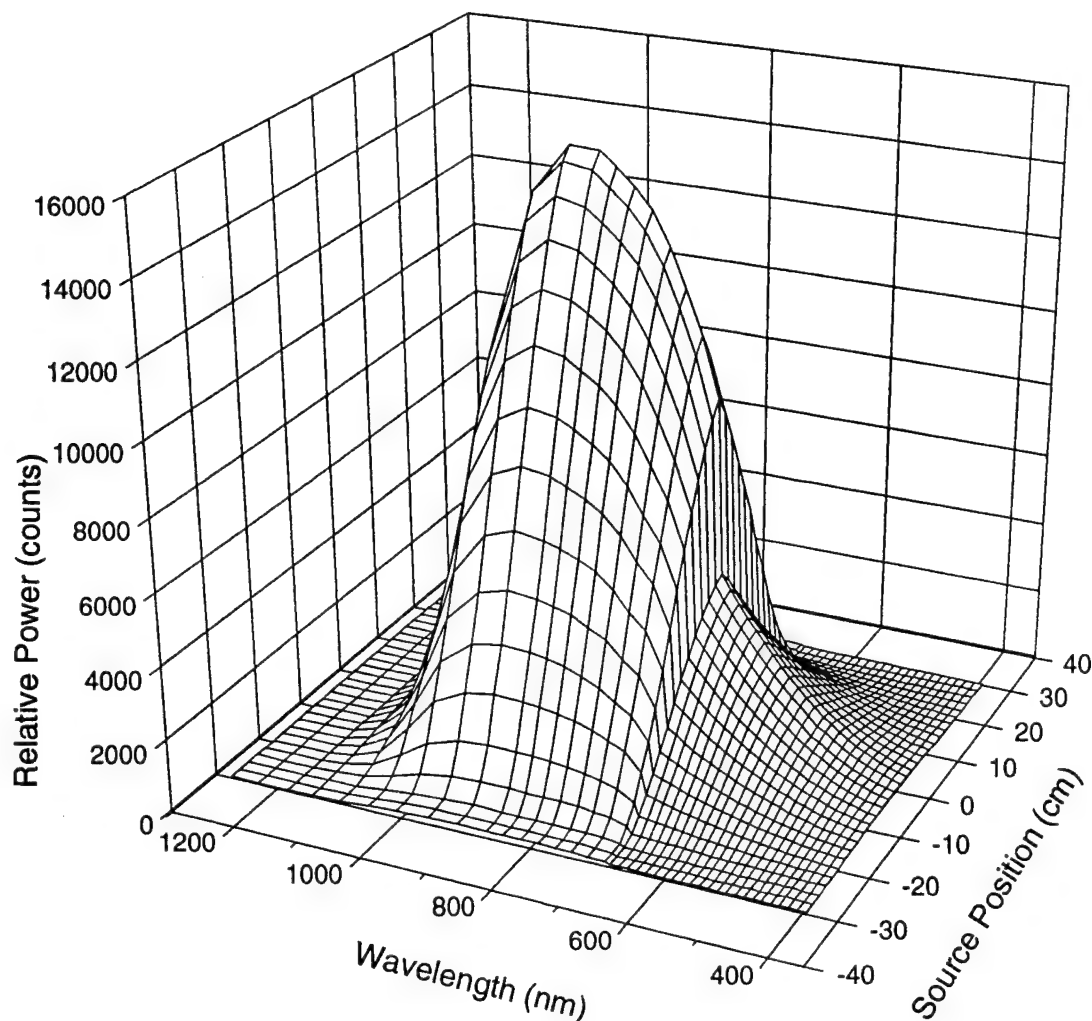
Figure 3.4: FOV measurement: Relative intensity versus position and wavelength for the radiance channel (3). Distance between the SSP and light source is 20 ft. Data shown is from the silicon detector. The jump in received intensity at 700 nm is due to CVF section 2 having a higher transmission than section 1.

versus the light source position and the measured wavelength. As the position of the source is changed we see a peak in the received power at the experiment centerline with the power falling off rapidly as the light source is moved off center. Looking at increasing wavelengths, we see an increase in the power received from 400 nm through 700 nm. At 700 nm there is a large jump in the power received, followed by a steady increase to the received power maximum at 900 nm. Beyond 1000 nm the power received falls off rapidly.

The jump in received power at 700 nm is a factor of two effects: the second CVF section is physically thinner and therefore has a higher transmission, it also has a steeper

wavelength gradient and each reading will have a wider bandwidth. The rapid decrease in received power beyond 1000 nm is a combined factor of the lamp emitting less in this spectral region and approaching the effective range of the silicon detector. Figure 3.5 shows the corresponding graph for the parallel polarization channel (2). Features of the parallel polarization are similar to the radiance channel, except the power received is approximately half that of the radiance channel.
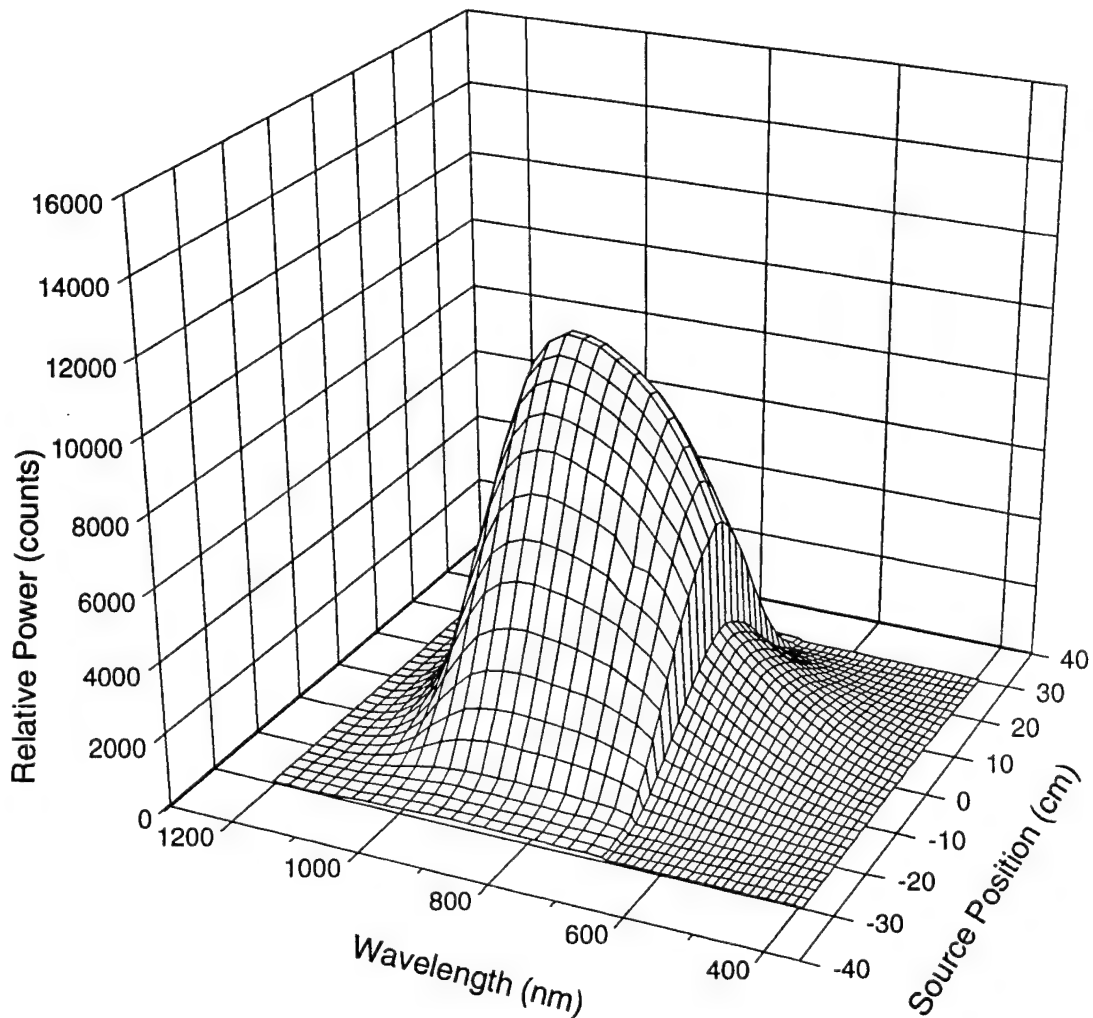
Figure 3.5: FOV measurement: Relative intensity versus position and wavelength for the parallel polarization channel (2). Distance between the SSP and light source is 20 ft. Data shown is from the silicon detector. The jump in received intensity at 700 nm is due to CVF section 2 having a higher transmission than section 1.
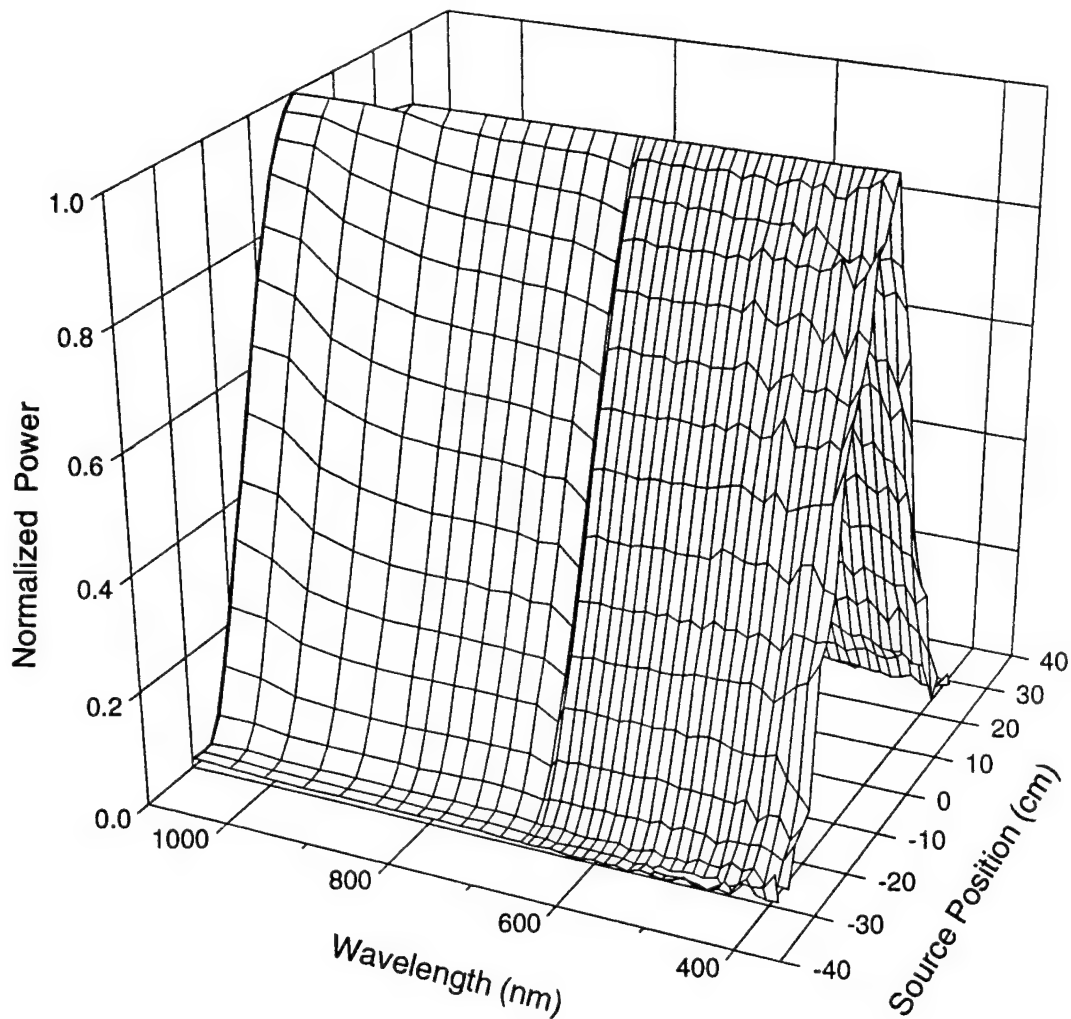
Figure 3.6: FOV measurement: Normalized intensity versus position and wavelength for the radiance channel. Distance between the SSP and light source is 20 ft. Data shown is from the silicon detector.

The field of view is determined by finding the two positions where the received power is $\frac{1}{2}$ the maximum. The width between these two positions and the distance between the light source and the SSP are then used to calculate the viewing angle. To automate the process, the data were first normalized as shown in Figure 3.6 for the radiance channel. Note how the constant distant lines roll over the top of the curve at the near infra red wavelengths. This is due to the longer wavelength light being 'bent' as is passes through the optics. In effect the SSP looks in a slightly different direction at the longer wavelengths.

The data for each wavelength are now fit to a gaussian curve of the form:
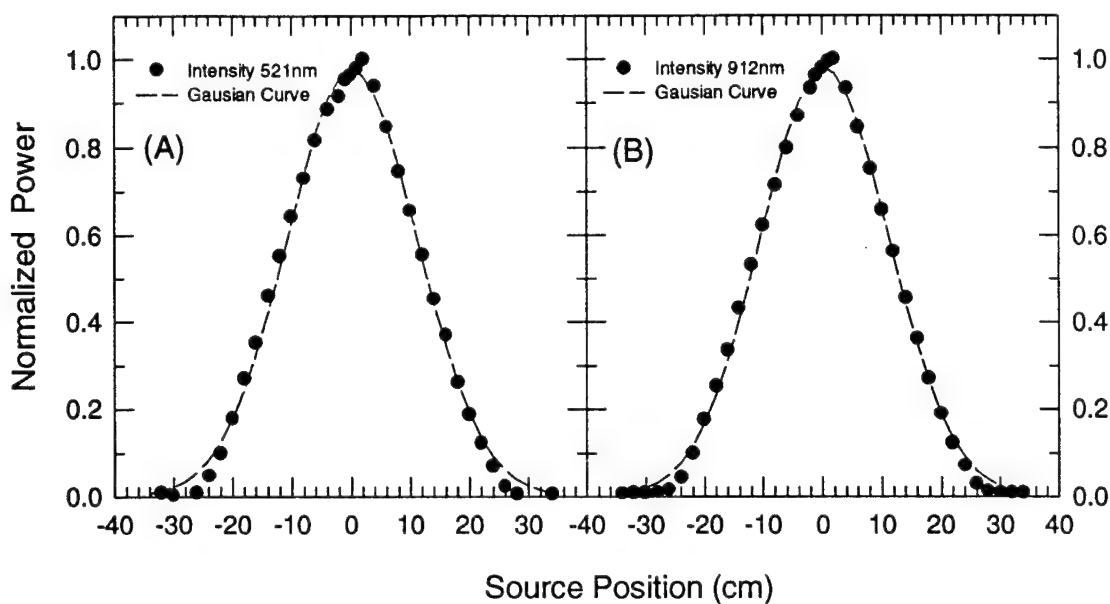
Figure 3.7: FOV measurement: Gaussian curve fit to the normalized data. Data for 521 nm is shown in (A) and 912 nm in (B). Distance between the SSP and light source is 20 ft.

$$ReceivedPower = \frac{k}{s}\exp[-.5\{(d-m)/s\}^2] \tag{3.1}$$

Where d = distance from the experiment centerline, m is the distribution mean, s is the standard deviation, and k is the amplitude factor. Figure 3.7 shows how the actual data fit the gaussian curve for 521 nm and 912 nm. Once the parameters k, s, and m are known the equation can be solved for the two locations where received power equals 50% of the maximum, or more appropriately, the width of the 50% viewing area

$$ViewWidth = \sqrt{(2m)^2 - 4(m^2 + s^2(2ln(\frac{sp}{k})))} \tag{3.2}$$

where p is 50%. Once the the viewing width is known, it is trivial to calculate the half angle of view. The resultant half angle fields of view are shown in Figure 3.8.

3.3.2 Cosine Response of Diffuser

The object of this exercise is to measure how the transmission of the flashed opal diffuser in channel 1 varies as a function of the incident angle of incoming radiation.
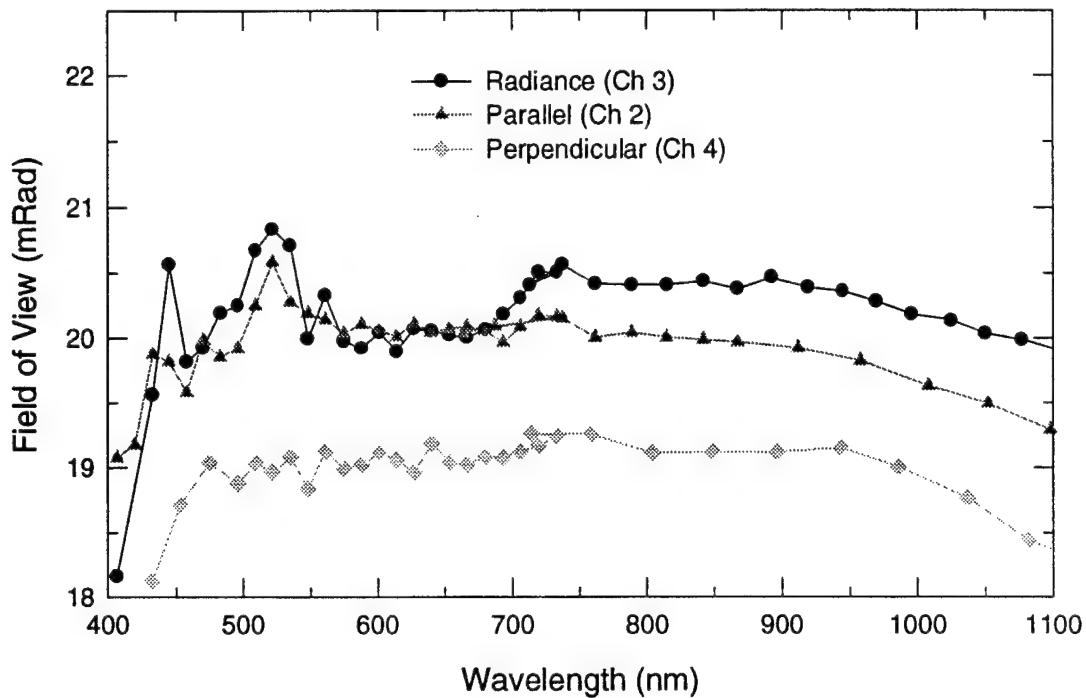
Figure 3.8: Field of view versus wavelength for the radiance, parallel polarization, and perpendicular polarization channels.

Flashed opal is the only commercially available material that allows the transmission of radiation from any angle. The diffuser is made by bonding a thin layer of diffusing glass to a supporting clear glass substrate. The diffusing glass causes multiple scattering of light. By nature, the shorter wavelengths scatter more, which also means transmission losses are greater. Flashed opal diffusers work well through visible wavelengths and the transmission curve is close to that shown in Figure 3.9, however, at longer wavelengths a directed component is superimposed at the forward direction. Part of this exercise is to define the extent of this forward transmission lobe.

A schematic of the diffuser response setup is shown in Figure 3.10. Setup is similar to that for the narrow field of view exercise, however, the distance between the SSP and the light source is only 53.3 cm. The lamp was calibrated by Eppley Labs at a distance of 50 cm, they recommend use of the lamp only for distances between the lamp and detector in excess of 45 cm. The SSP was set as close as it could be to the lamp and still have room for the screens to reduce reflections. Once the SSP and light source were aligned, the SSP
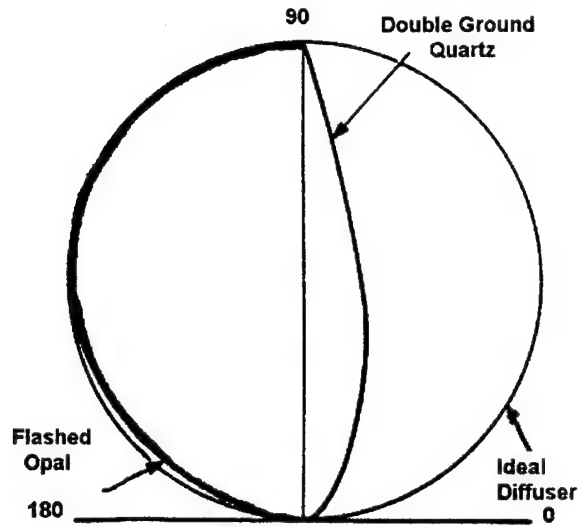
Figure 3.9: Transmission of an ideal diffuser, a flashed opal diffuser, and double ground quartz.

was rotated and the received intensity was measured as the angle between the SSP and light source was varied. The procedure used is described in detail in Appendix B.
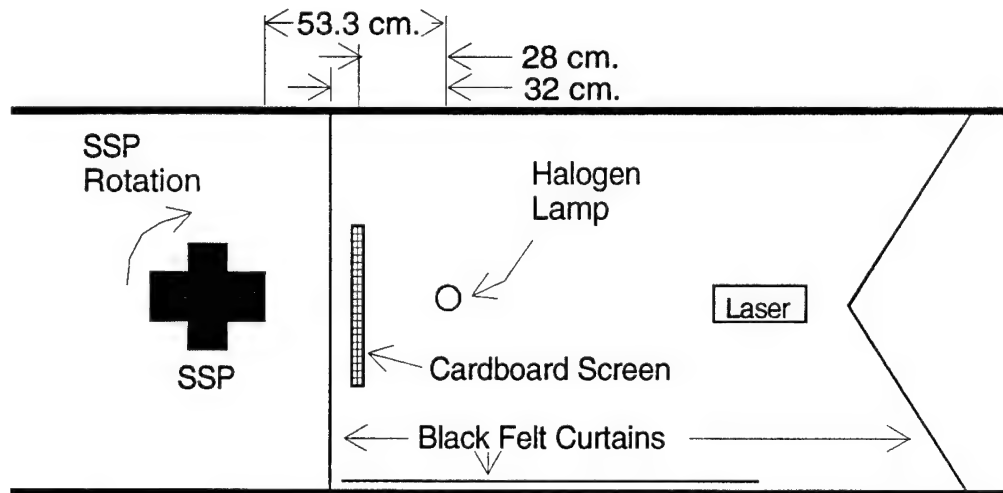
Figure 3.10: Diffuser transmission: Equipment setup for measuring the angle dependence of transmission for the flashed opal diffuser.

Results of the measured intensity versus the incident angle are shown in Figure 3.11. Data were not recorded when angles exceeded 80° because the front of the SSP vacuum chamber blocked all light from reaching the diffuser lens. In general, power increases as the
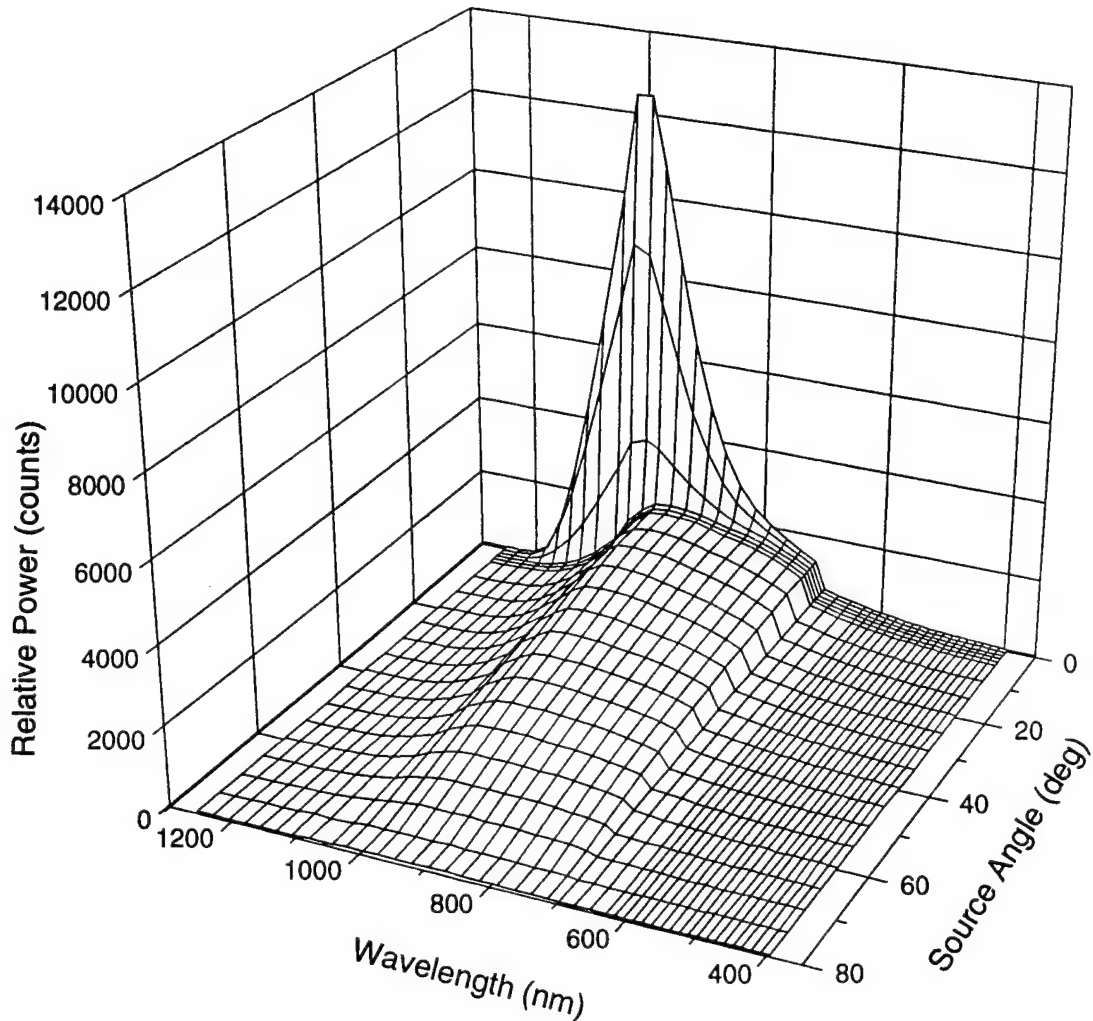
Figure 3.11: Diffuser Transmission: Relative power versus wavelength and angle between SSP and Source. Distance between the SSP and light source is 53.3 cm.

source angle is decreased to 0. From 400 nm through 800 nm there is a gradual increase, although the received power is so low it is difficult to see. From 800 nm through 1100 nm there is an extreme increase in power received at angles less than 3°, this is the strong forward transmission lobe mentioned previously. The maximum power received is shifted slightly to 1000 nm instead of 900 nm. Beyond 1100 nm the signal falls off sharply as this is beyond the range of the silicon detector.

To further explore how the flashed opal diffuser transmits radiation, the data were normalized so the maximum signal received is equal to unity as shown in Figure 3.12. Three distinct areas of diffuser transmission are evident. From 500 nm through 750 nm
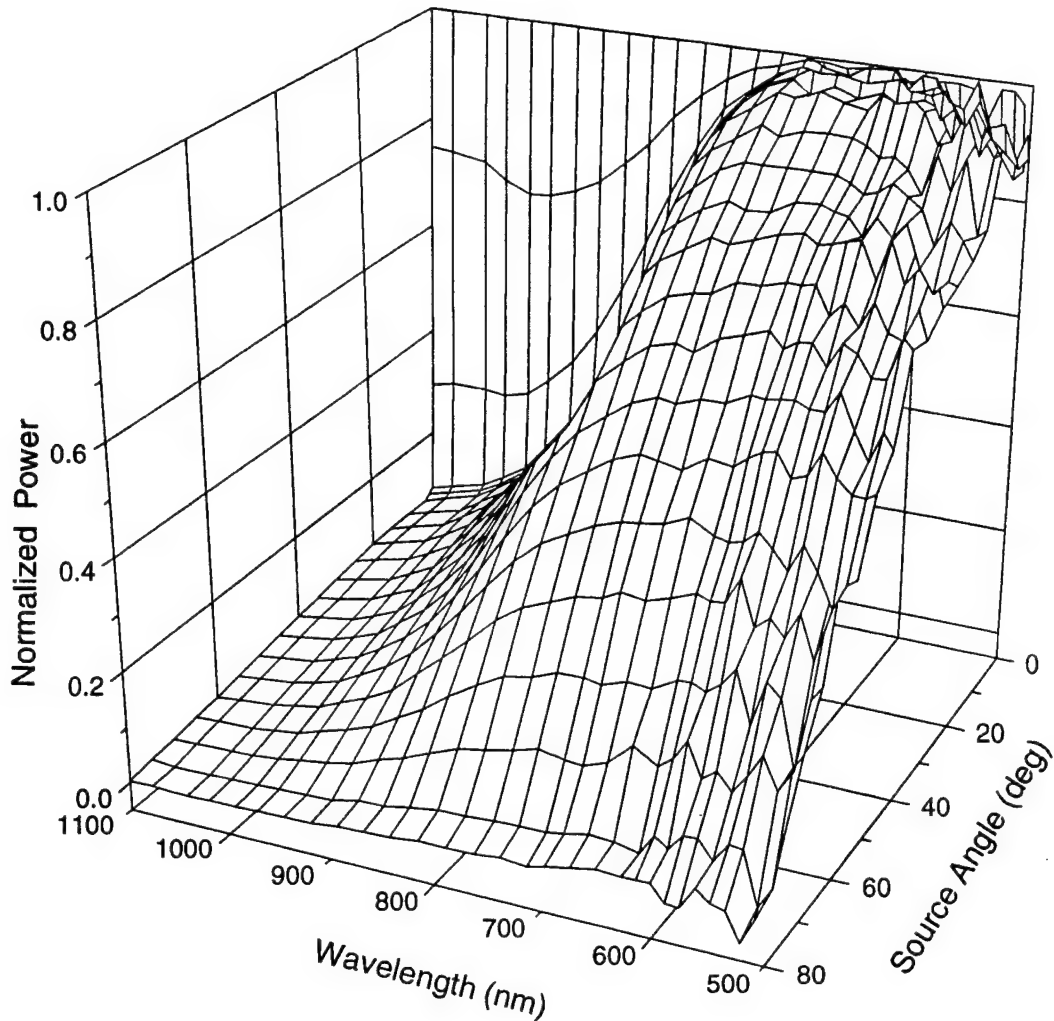
Figure 3.12: Diffuser transmission: Normalized power versus wavelength and angle between SSP and source. Distance between the SSP and light source is 53.3 cm.

the transmission curve is roughly a cosine curve. However, between 500 and 600 nm the received signal is weak enough that instrument noise distorts the curve. Below 500 nm, the data were to noisy too define a curve. From 850 nm through 1100 nm the transmission curve has a very strong peak between 0° and 2°. At 1000 nm the power received drops to less than 85% of the maximum by 3°. Between 750 nm and 850 nm there is a rapid transition from a cosine transmission curve to a curve with the strong forward transmission lobe.
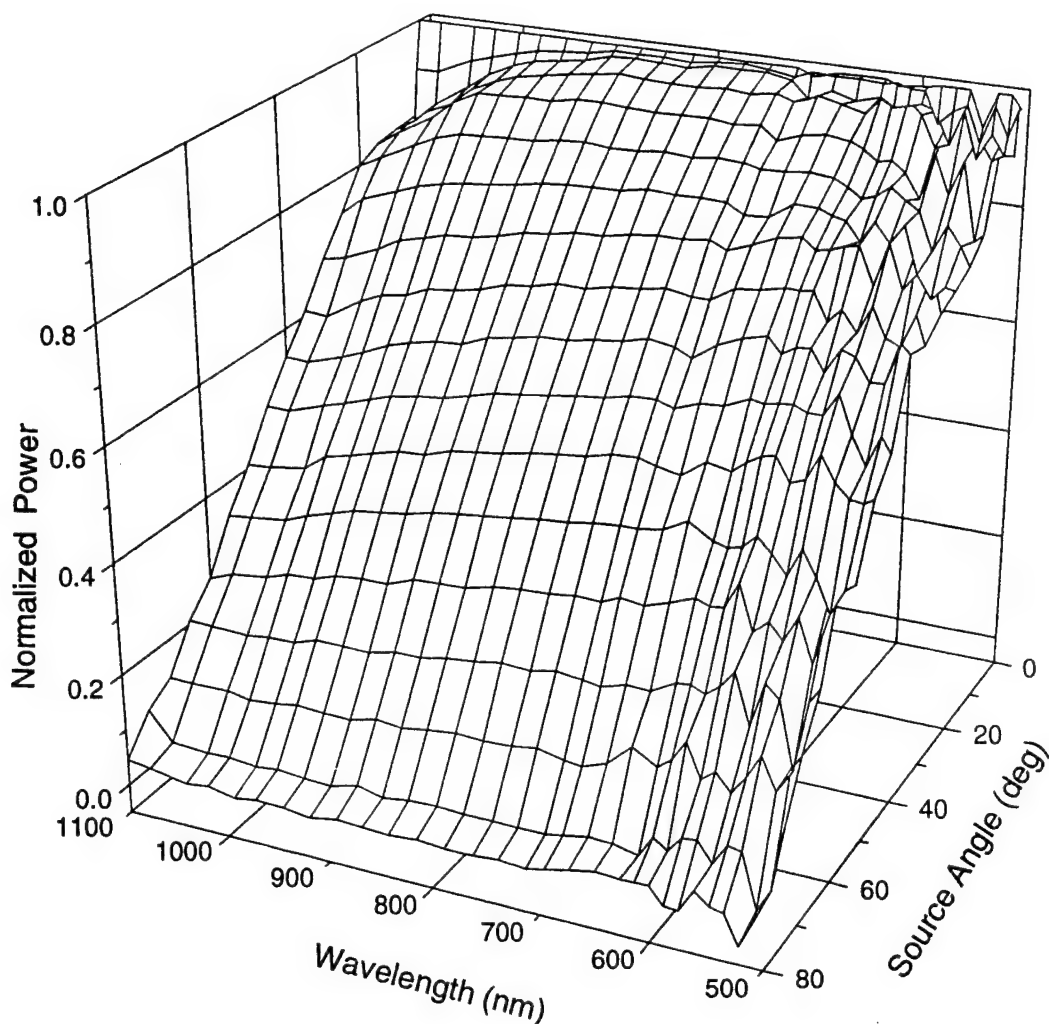
Figure 3.13: Diffuser transmission: Normalized power versus wavelength and angle between SSP and source, forward transmission lobe removed. Distance between the SSP and light source is 53.3 cm. Forward transmission lobe is removed by eliminating received power data for 2° to 0°.

The forward transmission lobe was removed by normalizing the data between 3° and 80° to unity as shown in Figure 3.13. Even at the longer wavelengths, the transmission curve approximates a cosine curve once the forward transmission lobe is removed.

To allow the calculation of diffuse light, a formula for the transmission curve is needed. For this purpose a curve of the form:

$$\frac{Received\,Power(\theta)}{Receiver\,Power(\theta=0)} = a\theta^2 + b\theta + c + d(exp[-e\theta]) \tag{3.3}$$
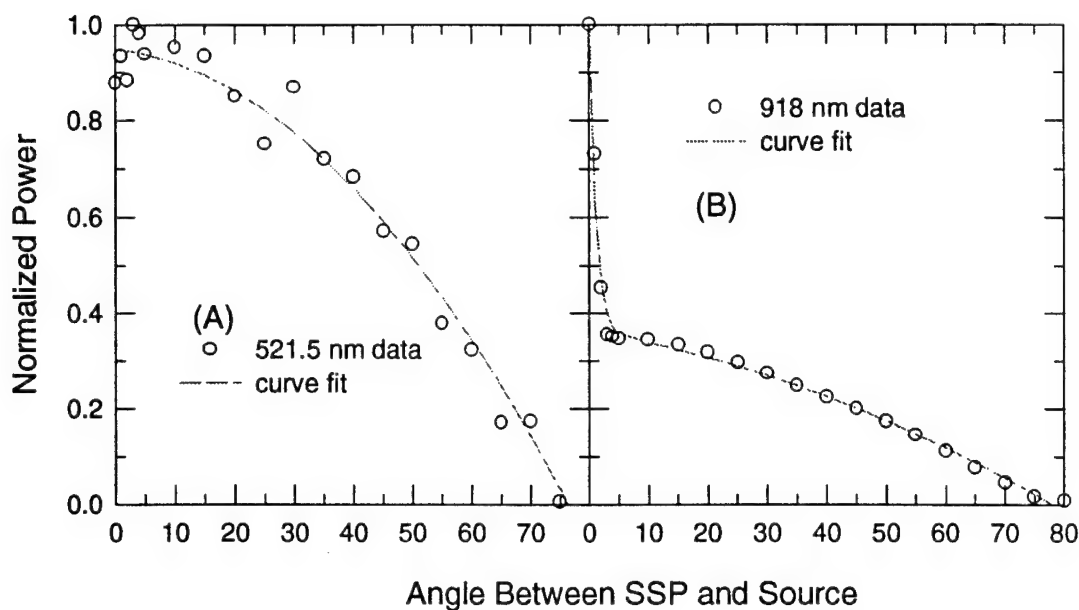
Figure 3.14: Diffuser transmission: Curve fit for the diffuse channel transmission function. Data for 521 nm is shown in (A) and 912 nm in (B). Distance between the SSP and light source is 53.3 cm.

where the parameters a, b, c, d, and e are all adjusted to fit the data. The first three terms of the right hand side will approximate the cosine transmission curve. The exponential term accounts for the forward transmission lobe. The parameter e is adjusted to cut off the effects of the forward transmission lobe at the proper angle. Figure 3.14 shows an example curve fit for both 521 nm and 918 nm. The parameters for all the diffuse wavelengths are tabulated in Appendix C.

3.3.3 Detector Response

The detector response was determined from two tests - the first applies to the diffuse channel (1) and the second to the three narrow field of view channels (2 - 4) channels. For the diffuse channel the SSP looks directly at the calibration light and measurements are taken to relate SSP measured voltage counts to the incident radiation flux. For the three narrow filed of view channels the light source is reflected from a lambertian reflectance plate, the SSP looks at the lambertian plate. Again, a relationship between voltage counts and incident radiation is determined.

Data processing and measurement errors have not yet been addressed. SSP raw data consist of a stream of 8 bit values, described in Table 2.4. One scan of data is normally 2594 bytes long, however, for this experiment the data stream were shortened. Since data from only 4 of the 12 detectors are used, the byte pattern was shortened to 864 bytes. This decreased the amount of data going to the data acquisition computer hard drive, and fewer data write errors are encountered. Under normal conditions, the CPU data write process lags the SSP data acquisition and approximately 1 scan of 20 will not be written to disk correctly. With the shortened byte pattern, the SSP normally drops one scan of the first 5 and then accurately records all data. The analog to digital converters also have a maximum value they will assign to the high byte. Zero signal from the detectors is a maximum digital count and detector saturation has a zero digital count. If the CPU data write process gets behind the SSP acquisition, the normal error is to shift the byte pattern one byte up or down. To find 'bad data' the length of each scan is checked as it is read from disk. Scans that are too short or too long are considered bad. All high bytes are also checked to verify they do not exceed the maximum high byte value due to a data shift. A scan with the data shifted is also considered bad. Since there are generally only 1-2 bad scans with each data file, recovery of data from the bad scans is not critical and the bad scans are just thrown out. Additionally, the first 5 scans of each data set are thrown out to allow the SSP electronics to settle into the normal operating mode after the start up power surge. After each scan has been verified as good, it is added into both

an averaging array and an error array. To calculate errors for the received power, the standard deviation is determined using the computational routine:

$$\sigma_{V_c} = \sqrt{\frac{\sum x_i^2 - n\bar{x}^2}{n-1}} \tag{3.4}$$

Background noise causes a DC voltage offset to be introduced into the data. This offset varies for each channel and each gain setting. Figure 3.15 shows one scan of raw data . To remove the voltage offset, data are normalized so readings from the two covered broadband holes are equal to zero. The data can then be parsed and the proper wavelength assigned to each reading.

Diffuse Channel

Setup for the detector response of the diffuse channel is illustrated in Figure 3.16. The diffuse channel looks directly at the calibration source. Alignment is achieved using the the laser. Once the SSP is aligned with the source lamp, received power is measured for every gain setting the SSP uses to record data. The distance between the SSP and light source was only 51.4 cm. Measurement of the received power is related to the light source spectral intensity by

$$k_\lambda = \frac{f_{source_\lambda} HBW_\lambda (d_{cal}/d)^2 T_\lambda}{V_c} \tag{3.5}$$

where k_λ is the calibration coefficient, f_{source_λ} is the spectral intensity emitted by the calibration lamp, HBW_λ is the half bandwidth, d_{cal} is the calibration distance for the source (50 cm), d is the distance between the SSP and source lamp, T_λ is the path transmission, and V_c is the measured voltage counts. Due to the short path length and low relative humidity during the calibration (less than 25%) the transmission is assumed to be 1.

NFOV Channels

Setup for determining the detector response of the narrow field of view channels is illustrated in Figure 3.17. The purpose of this exercise is to relate the voltage counts received from the SSP for different channels and gain settings to both each other and the incident radiance. The calibration lamp illuminates the lambertian reflectance plate and

Diffuse and Radiance Channels

Polarization Channels
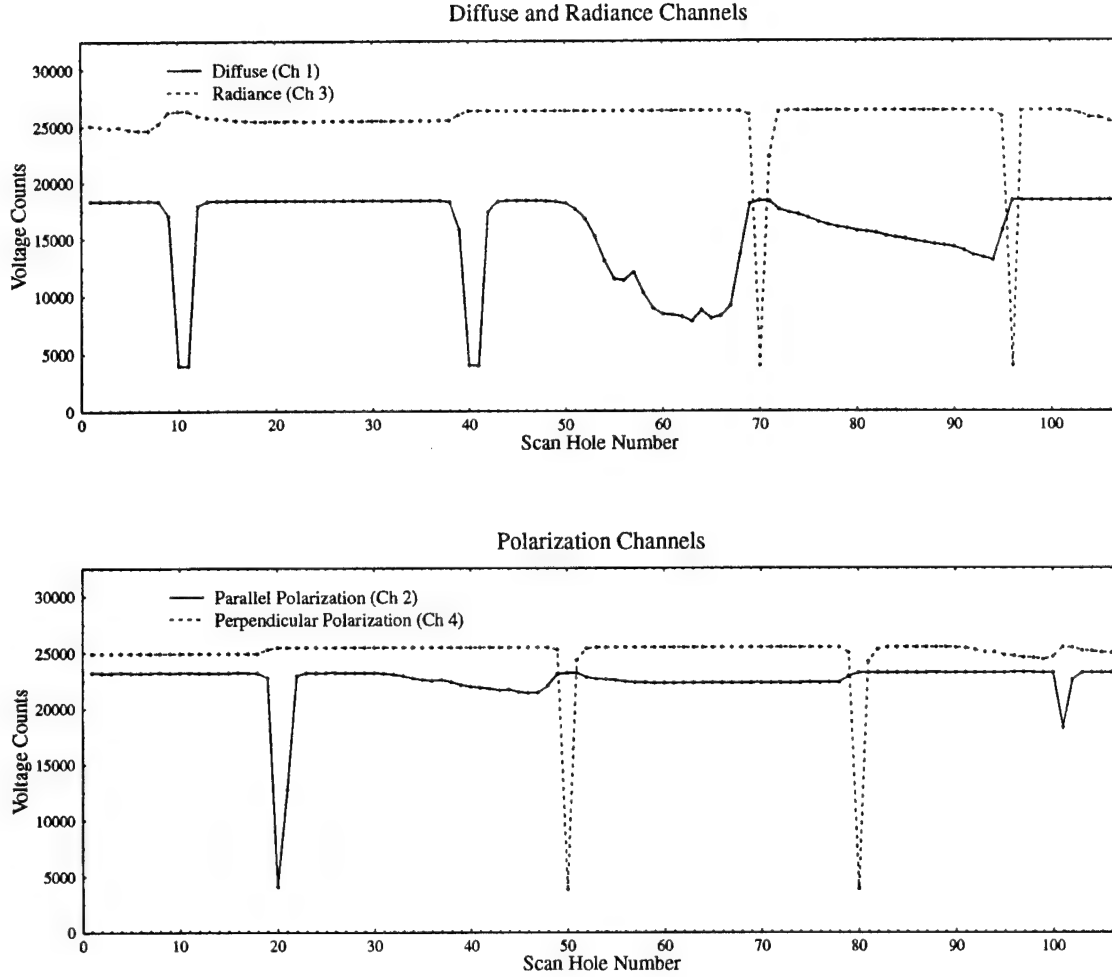
Figure 3.15: SSP raw data. Gain setting on channel 1 is 25.75. Gain setting for channels 2-4 is 13.38. The zero signal point is at the top of the graph and the curve drops as received power increases.

the SSP measures the reflected radiance. The laser is again user to align the equipment, then received power measurements are made for each gain setting the SSP records data. This is the most critical portion of the calibration. The setup procedure used is described in Appendix B.

Spectral intensity emitted by the source is related to received power by

$$k_\lambda = \frac{f_{source_\lambda} HBW_\lambda (d_{cal}/d)^2 R_\lambda T_{\lambda_{s-p}} T_{\lambda_{p-SSP}} \cos\theta \cos\phi}{P\pi V_c} \tag{3.6}$$

where k_λ is the calibration coefficient, f_{source_λ} is the spectral intensity emitted by the calibration lamp, HBW_λ is the half bandwidth, d_{cal} is the calibration distance for the
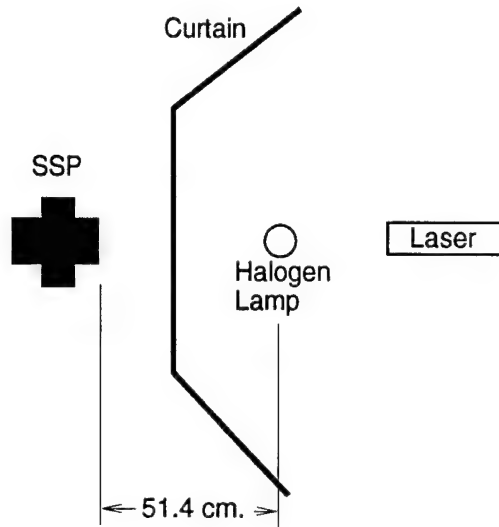
Figure 3.16: Equipment setup for determining the detector response for the diffuse channel(1).

source (50 cm), d is the distance between the reflectance plate and source lamp, R_λ is the spectral reflectance for the lambertian plate, $T_{\lambda_{s-p}}$ is the path transmission from the source lamp to the reflectance plate, $T_{\lambda_{p-SSP}}$ is the path transmission from the reflectance plate to the SSP, $\cos\theta$ is the angle the between the reflectance plate normal and the incident source radiation, $\cos\phi$ is the angle between the SSP and the reflectance plate normal, P accounts for the Glan-Taylors in the polarization channels and is equal to 1 for the radiance channel and 2 for the parallel and perpendicular polarization channels, and V_c is the measured voltage counts. As long as the lambertian plate fills the entire field of view, the NFOV angle and the distance between the SSP and lambertian plate cancel from the equation. Again, the path transmissions were assumed equal to 1. Resultant calibration coefficients enable measured voltage counts to be converted into atmospheric spectral intensity.

To calculate the error associated with the calibration coefficients, the calibration equations (3.5) and (3.6) must be considered. For an absolute calibration, every term could induce errors. The emission from the source changes with power fluctuations, the HBW's vary with each wavelength, measuring the distance between the SSP and source inaccurately induces an error, path transmission changes with room conditions, and instrument
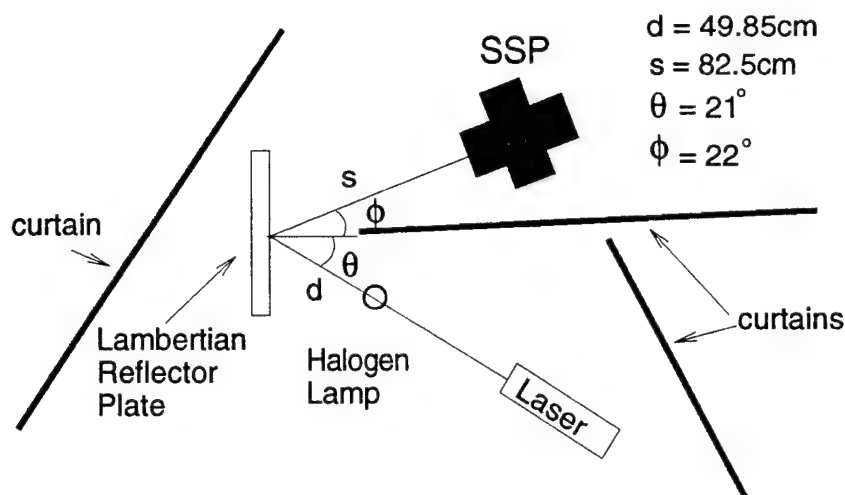
Figure 3.17: Equipment setup for determining the detector response for the narrow field of view channels (2 - 4).

electronic noise causes the received voltage counts to vary. The largest errors arise from the instrument placement (both alignment and distance between SSP and light source) and the instrument noise. Having the SSP out of alignment will induce a large error for the diffuse channel, especially at longer wavelengths. A 1 cm measurement error in the distance between the SSP and source causes a 4% error in the calibration equation. However, since we are only interested in a relative calibration between channels most of these errors cancel. The only error we need to consider is the instrument noise, or variation in received voltage counts and the error for the calibration coefficient is

$$\sigma_k = k(\frac{\sigma_V}{V}). \tag{3.7}$$

The calibration coefficients, k, for the diffuse and radiance channels are shown in Figure 3.18. The plot shows both the averaged k values and the associated error. Several interesting features emerge from Figure 3.18. First, the calibration coefficients for the diffuse channel are about 5 times that of the radiance channel. This is due to the low transmission of the flashed opal diffuser lens. Since less of the incident radiation is able to reach the detector, the calibration coefficient must be larger. Second, the error at the shorter wavelengths are much larger than the longer wavelengths. This is a side effect of the

calibration source. The emission from the calibration source, shown in Figure 3.2, is small below 500 nm. At the shorter wavelength there is less received power, and instrument noise is a larger portion of the measured signal. For the diffuse channel, additional radiation losses from the flashed opal lens extend this effect and the calibration coefficients have significant errors up to 700 nm. Third, the calibration coefficients increase rapidly at 1050 - 1100 nm. This is the effective range of the silicon detectors, and even though radiation energy is reaching the detector element, they do not measure it. Fourth, the calibration coefficients for the radiance channel jump at the end of CVF segment 1 ($\sim$ 740 nm) and at the beginning of CVF section 2 ($\sim$ 660 nm). This is caused by the cover put on the broadband channel partially covering the filter for these wavelengths. The same occurs for all channels, the data for these wavelengths was removed from the diffuse channel plot. Fifth, the calibration coefficients for CVF section 2 are smaller than section 1 since section 2 has a higher transmission.
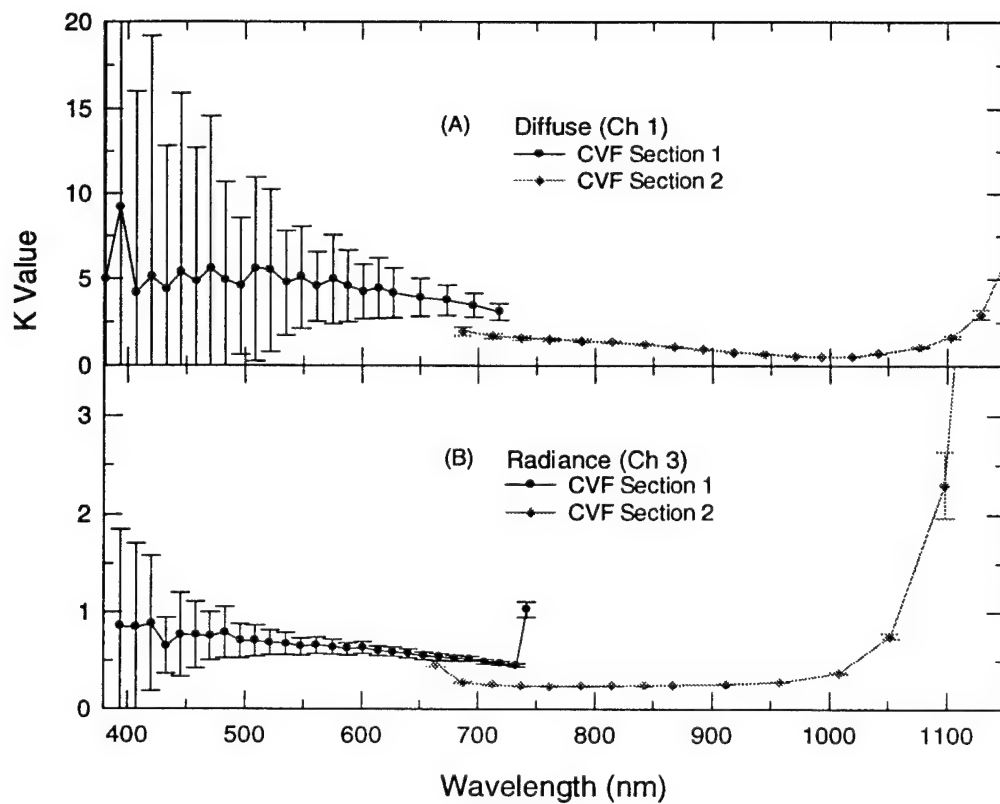
Figure 3.18: Calibration coefficients for the diffuse (Ch 1) and radiance (Ch 3) channels.

Chapter 4

MODEL

4.1 Introduction

A polarized, plane parallel, monochromatic radiative transfer model developed for a previous activity was adapted for this study (Evans and Stephens, 1991). It applies a rigorous solution of the radiative transfer equation for polarized light using the four Stokes parameters. For clear sky radiation, monochromatic works well since scattering and absorption properties are uniform over the bandwidths of the SSP channels. A 3D cartesian coordinate system is used, with the assumption of a plane parallel atmosphere. A point in the medium is defined by its z coordinate and the angular direction defined by the directional vector $\vec{\xi}$. This vector is represented by the angular pair (θ, ϕ) where θ is the zenith angle and ϕ the azimuth angle, see Figure 4.1.
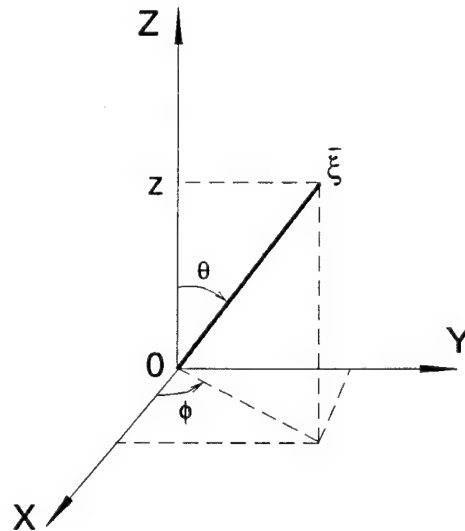
Figure 4.1: The general co-ordinate system and the specification of (θ, ϕ).

This model calculates the Stokes parameters (I, Q, U, V) for radiation diffusely scattered by the atmosphere. The complete polarized state of the radiation field is described by the intensity vector

$$\mathbf{I} = [I, Q, U, V] \tag{4.1}$$

Where I is the total intensity, Q characterizes the degree of polarization, U the plane of polarization, and V the ellipticity of the intensity. The Stokes parameters have units of intensity or power. This allows the Stokes parameters for multiple incoherent waves to be added together to obtain the total polarized state of a radiation field. Polarization may range anywhere from unpolarized ($Q = U = V = 0$) to totally polarized ($I^2 = Q^2 + U^2 + V^2$).

The Stokes parameters may be expressed in terms of the simple wave complex electric field vector (E_V, E_H) by:

$$I = |E_V|^2 + |E_H|^2$$

$$Q = |E_V|^2 - |E_H|^2$$

$$U = 2|E_V||E_H|cos\delta$$

$$V = 2|E_V||E_H|sin\delta \tag{4.2}$$

where δ is the phase difference between E_V and E_H.

An alternative set of Stokes parameters that separates the parallel (I_l) and perpendicular (I_r) components is defined by:

$$\mathbf{I} = [I_l, I_r, U, V] \tag{4.3}$$

where I_l and I_r are the intensity components perpendicular to each other and to the direction of propagation. The SSP measures I_l and I_r directly.

4.2   The polarized radiative transfer equation

The radiative transfer equation that describes the transfer of **I** through the plane parallel atmosphere can be written as

$$\mu \frac{d\mathbf{I}(\tau,\mu,\phi)}{d\tau} = -\mathbf{I}(\tau,\mu,\phi) + \frac{\tilde{\omega}}{4\pi} \int_0^{2\pi} \int_{-1}^1 \mathbf{M}(\mu,\phi;\mu',\phi')\mathbf{I}(\tau,\mu',\phi')d\mu'd\phi' + \sigma(\tau,\mu,\phi) \quad (4.4)$$

where, **I** is the four component Stokes vector, **M** is the four-by-four scattering matrix which depends on the Stokes representation (4.1), σ a vector for radiation sources, $\tilde{\omega}$ is the single scatter albedo, τ is the optical depth, μ is the cosine of the zenith angle, and ϕ is the azimuth angle. The detailed structure of **M** will be discussed latter. The coordinate system used is τ increases downward and μ is positive for downward directions.

The radiation field is separated into collimated and diffuse components. The above radiative transfer equation involves only the diffuse component. The collimated direct solar beam is attenuated according to Beer's Law $(e^{-\tau/\mu})$ and the radiation scattered from the collimated solar beam becomes a "pseudo-source".

The radiation sources can be separated into two terms,

$$\sigma(\tau,\mu,\phi) = \frac{\tilde{\omega}}{4\pi} e^{-\tau/\mu_o} \mathbf{M}(\mu,\phi;-\mu_o,\phi_o)\mathbf{F} + (1-\tilde{\omega})\mathbf{B}(T) \quad (4.5)$$

The first term on the right hand side of (4.4) describes the source of diffuse **I** due to single scatter from the direct solar beam. Solar radiation is unpolarized and of the form

$$\mathbf{F} = [F_o/\mu_o, 0, 0, 0] \quad (4.6)$$

where F_o is the direct solar flux at the top of the atmosphere and is taken to be incident along the direction (μ_o, ϕ_o).

The second term on the right hand side of (4.4) accounts for thermal emission of the medium. This emission function is also unpolarized and of the form

$$\mathbf{B} = [B(T), 0, 0, 0] \quad (4.7)$$

and $B(T)$ is the Planck black body function

$$B(T) = \frac{1.1911 \times 10^8}{\lambda^5[exp(\frac{1.4388 \times 10^4}{\lambda T}) - 1]} \quad (4.8)$$

where λ is the wavelength in microns, T is the temperature in Kelvins, and the units of B are Watts/(meter^2 ster micron).

4.3 The phase matrix

Single scattering calculations provide the scattering phase matrix $\mathbf{P}(\mu, \phi; \mu', \phi')$ which characterizes the single scatter of the Stokes parameters and is defined with respect to the scattering plane, or the plane defined by the directions of incident and scattered radiation. Multiple scattering calculations require that the scattering matrix be defined with respect to a fixed frame of reference rather than the relative frame of reference which defines $\mathbf{P}(\mu, \phi; \mu', \phi')$. Thus a transformation is required that accounts for this rotation and which refers the Stokes parameters of the incident radiation to the meridional plane containing the direction of incidence (μ', ϕ') and the Stokes parameters of the scattered radiation to the meridional plane containing the direction of scattering (μ, ϕ). Such a transformation has been discussed in detail by Chandrasekhar (1960) and is defined by the rotation matrix $\mathbf{L}(i)$

$$\mathbf{L}(i) = \begin{pmatrix} 1 & 0 & 0 & 0 \\ 0 & \cos 2i & -\sin 2i & 0 \\ 0 & \sin 2i & \cos 2i & 0 \\ 0 & 0 & 0 & 1 \end{pmatrix} \quad (4.9)$$

for the (I,Q,U,V) Stokes representation.

The polarization reference plane is rotated from the incident meridional plane to the scattering plane, the single scattering transformation represented by $\mathbf{P}$ is applied, and the polarization is rotated to the outgoing meridional plane (see Figure 4.2). The result of these transformations is a phase matrix $\mathbf{M}(\mu, \mu'; \phi - \phi')$ defined with respect to a fixed frame of reference where

$$\mathbf{M}(\mu, \mu'; \phi - \phi') = \mathbf{L}(\pi - i_2)\mathbf{P}(\mu, \phi; \mu', \phi')\mathbf{L}(i_1) \quad (4.10)$$
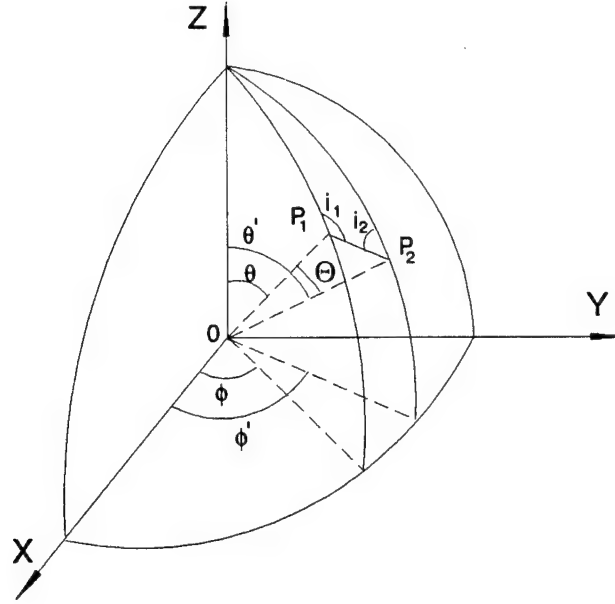
Figure 4.2: Illustration of scattering angle and the rotation of the polarization reference frame. The polarization of the incident ray (θ', ϕ'), in terms of the P_1OZ plane, is rotated into the scattering plane (P_1OP_2), the scattering matrix is applied, and then the polarization of the scattered ray (θ, ϕ) is rotated into the P_2OZ plane.

The scattering angle Θ in Figure 4.2 is formally defined as

$$\cos \Theta = \cos \theta \cos \theta' + \sin \theta + \sin \theta' \cos(\phi - \phi'). \tag{4.11}$$

The angles i_1 and i_2 are the angles that the plane of scattering makes with the meridian planes containing the directions of incidence and scattering respectively. These angles can be determined from spherical trigonometry by

$$\sin i_1 = \sin \theta \sin(\phi' - \phi)/\sin \Theta \tag{4.12}$$

$$\sin i_2 = \sin \theta' \sin(\phi' - \phi)/\sin \Theta \tag{4.13}$$

$$\cos i_1 = [\sin \theta' \cos \theta - \sin \theta \cos \theta' \cos(\phi' - \phi)]/\sin \Theta \tag{4.14}$$

$$\cos i_= [\sin \theta \cos \theta' - \sin \theta' \cos \theta \cos(\phi' - \phi)]/\sin \Theta \tag{4.15}$$

For randomly oriented particles with a plane of symmetry the four-by-four scattering phase matrix has only six unique values (Hovenier, 1969):

$$\mathbf{P}(\cos \Theta) = \begin{pmatrix} P_1 & P_2 & 0 & 0 \\ P_2 & P_5 & 0 & 0 \\ 0 & 0 & P_3 & P_4 \\ 0 & 0 & -P_4 & P_6 \end{pmatrix} \tag{4.16}$$

The phase matrix for spheres has $P_1 = P_5$ and $P_3 = P_6$.

After the polarization rotations have been applied, the scattering matrix has the form

$$\mathbf{M} = \left(\begin{array}{c|c|c|c} P_1 & P_2 \cos 2i_1 & -P_2 \sin 2i_1 & 0 \\ \hline P_2 \cos 2i_2 & \begin{array}{c} P_5 \cos 2i_1 \cos 2i_2 \\ -P_3 \sin 2i_1 \sin 2i_2 \end{array} & \begin{array}{c} -P_5 \sin 2i_1 \cos 2i_2 \\ -P_3 \cos 2i_1 \sin 2i_2 \end{array} & -P_4 \sin 2i_2 \\ \hline P_2 \sin 2i_2 & \begin{array}{c} P_5 \cos 2i_1 \sin 2i_2 \\ +P_3 \sin 2i_1 \cos 2i_2 \end{array} & \begin{array}{c} -P_5 \sin 2i_1 \sin 2i_2 \\ +P_3 \cos 2i_1 \cos 2i_2 \end{array} & P_4 \cos 2i_2 \\ \hline 0 & -P_4 \sin 2i_1 & -P_4 \cos 2i_1 & P_6 \end{array} \right) \tag{4.17}$$

4.4 Numerical Considerations

4.4.1 Fourier Expansion in Azimuth

The first step in formulating the solution to (4.4) is to represent the azimuthal dependence of all functions as a Fourier series. A real function $F(\phi)$ is expanded in the finite series

$$F(\phi) = \sum_{m-0}^{M} F_m^c \cos \phi = F_m^s \sin \phi \qquad F_0^s = 0 \tag{4.18}$$

with the sines and cosines forming and orthogonal set of functions

$$\int_0^{2\pi} \cos m\phi \cos m\phi' = c_m^c \delta_{mm'}$$
$$\int_0^{2\pi} \sin m\phi \sin m\phi' = c_m^s \delta/mm'$$
$$\int_0^{2\pi} \cos m\phi \sin m\phi' = 0 \tag{4.19}$$

$$\tag{4.20}$$

where

$$c_m^r = \begin{cases} 2\pi & r = c, \quad m = 0 \\ 0 & r = s, \quad m = 0 \\ \pi & m > 0 \end{cases} \tag{4.21}$$

The integral over azimuth of a product of functions transforms to a sum of the product of the Fourier coefficients

$$\int_o^{2\pi} A(\phi)B(\phi)d(\phi) = \sum_{m=0}^{M} \sum_{r=c,s} c_m^r A_m^r B_m^r \tag{4.22}$$

The radiative transfer equation is transformed to

$$\mu \frac{d\mathbf{I}_{mr}}{d\tau} = -\mathbf{I}_{mr} + \frac{\tilde{\omega}}{4\pi} \sum_{m'=0}^{M} \sum_{r'=c,s} c_{m'}^{r'} \int_{-1}^{1} \mathbf{M}_{mm'rr'}(\mu, \mu') \mathbf{I}_{m'r'}(\mu') d\mu' + \sigma_{mr}(\mu) \tag{4.23}$$

$$m = 0, 1, ..., M \qquad r = c, s$$

where the m subscript refers to the azimuthal Fourier mode, and the r subscript refers to the cosine and sine terms. The Fourier expansion is done separately for each element of the Stokes radiance vectors and the scattering matrix.

4.4.2 Numerical Quadrature in Zenith Angle

The integral in zenith is approximated with a numerical quadrature scheme, which uses polynomial interpolation to numerically perform the integration. A quadrature scheme provides a set of abscissae and weights for the integral approximation

$$\int_a^b f(x)dx \approx \sum_{i=1}^n w_i f(X_i) \qquad (4.24)$$

For our application, the integral is over the cosine of the zenith angle(μ), or $a = -1$ to $b = 1$. Abscissae (μ_j) and weights (w_j) are determined for

$$\int_{-1}^1 F(\mu)d(\mu) \approx \sum_{j=1}^N w_j F(+\mu) + \sum_{j=1}^N w_j F(-\mu) \qquad (4.25)$$

where the first and second terms of the right hand side represent the contribution to the diffuse radiation field from the scatter over the upper and lower hemispheres respectively. There are N angles in each hemisphere of solid angle. This approximation is sometimes referred to as the "2n stream" approximation.

The model provides a choice of four quadrature schemes: Gaussian, double Gaussian, Lobatto, and extra angles. In the Gaussian scheme, the angles are provided by the method and are chosen so the angle μ is not equal to -1, 0, or 1. The Gaussian scheme uses the same angles in each hemisphere. Gaussian quadrature can exactly integrate polynomials up to degree $2n - 1$. It is exact for integration over both hemispheres, but not for integrations over only one hemisphere.

The double-Gaussian is used if accurate hemispheric fluxes are desired. This method uses integration limits of 0 to 1 and creates a slight clustering of points near one side of the interval. It works well for low solar angles.

The Lobatto quadrature scheme is similar to the Gaussian method, only the limits of integration are included in the abscissae. This provides a quadrature angle in both the

zenith and nadir. This method is well suited for many remote sensing applications that use a zenith or nadir viewing direction.

The extra angle mode uses the Gaussian scheme, but allows the user to select angles to add to the abscissae the method generates. The extra angles are assigned a weighting factor of zero. This mode provides an easy method of comparing the model results to tabulated values.

Replacing the zenith angle integral with the quadrature sum gives

$$\pm\mu_j \frac{d\mathbf{I_{mr}}(\tau, \pm\mu)}{d\tau} = -\mathbf{I}(\tau, \pm\mu)$$

$$+\frac{\tilde{\omega}}{4\pi} \sum_{m'=0}^{M} \sum_{r'=c,s} \sum_{j'=1}^{N} c_{m'}^{r'} w_{j'} [\mathbf{M}_{mm'rr'}(\pm\mu_j, +\mu_{j'})\mathbf{I}_{m'r'}(\tau, +\mu_{j'})$$

$$+ \mathbf{M}_{mm'rr'}(\pm\mu_j, -\mu_{j'})\mathbf{I}_{m'r'}(\tau, -\mu_{j'})] + \sigma_{mr}(\tau, \pm\mu_j) \quad (4.26)$$

$$j = 1, ..., N \qquad m = 0, ..., M \qquad r = c, s$$

4.4.3 Radiative Transfer Scattering Matrix

It is convenient to express the single scattering phase matrix $\mathbf{P}$ as a Legendre series

$$\mathbf{P}(\cos\Theta) = \sum_{l=0}^{N_l} \chi_l \mathcal{P}_l(\cos\Theta) \quad (4.27)$$

where $\mathcal{P}_l$ is the l'th order Legendre polynomial and χ_l is the l'th Legendre coefficient matrix. For the scalar (unpolarized) case, the Fourier modes of the phase function are calculated from the coefficients of the Legendre series using the addition theorem of associated Legendre functions. The rotation of the frame of polarization precludes that method for finding the Fourier modes of the scattering matrix. The method used here is to perform the polarization rotation in azimuth space and then Fourier transform the results to get the scattering matrix for each Fourier azimuth mode. This method is similar to that of Ishimaru et al. (1984), except the rotation is performed on the Stokes parameters rather than the scattering amplitudes.

For each pair of quadrature angles μ_j and $\mu_{j'}$ (outgoing and incoming directions) and for a number of azimuth angles $\Delta\phi_k = \phi' - \phi$, the scattering angle Θ is found and the Legendre series is summed for the six unique elements of the phase matrix. Equation 4.17

is used to obtain the scattering matrix $\mathbf{M}$ with the desired polarization reference frame. The azimuth angle differences are at equally spaced angles

$$\Delta\phi_k = \frac{2\pi k}{N_\phi} \qquad k = 0, 1, ..., N_\phi - 1 \tag{4.28}$$

where N_ϕ is chosen so the highest frequency in $\Delta\phi$ is completely sampled, or so

$$N_\phi = 2^{[log_2(N_l+4)+1]+1}. \tag{4.29}$$

The scattering matrix $\mathbf{M}$ is then Fourier transformed to obtain the Fourier series representation

$$\mathbf{M}(\mu_j, \mu_{j'}, \phi' - \phi) = \sum_{m=0}^{M} [\mathbf{M}_m^c(\mu_j, \mu_{j'}) \cos m(\phi' - \phi) + \mathbf{M}_m^s(\mu_j, \mu_{j'}) \sin m(\phi' - \phi)] \tag{4.30}$$

This matrix is a Fourier series in $\phi' - \phi$, but it must be transformed into a Fourier series in ϕ' and ϕ, such as

$$\mathbf{M}(\mu_j, \mu_{j'}, \phi' - \phi) = \sum_{m=0}^{M} \sum_{m'=0}^{M} [\mathbf{M}_{mm'}^{cc} \cos m(\phi) \cos m'(\phi') + \mathbf{M}_{mm'}^{cs} \cos m(\phi) \sin m'(\phi')$$
$$+ \mathbf{M}_{mm'}^{sc} \sin m(\phi) \cos m'(\phi') + \mathbf{M}_{mm'}^{ss} \sin m(\phi) \sin m'(\phi')]. \tag{4.31}$$

From angle addition formulae for cosine and sine, the coefficients for the double Fourier series are related to the single Fourier series coefficients by

$$\mathbf{M}_{mm'}^{cc} = \mathbf{M}_{mm'}^{ss} = \mathbf{M}_m^c \delta_{mm'}$$

$$\mathbf{M}_{mm'}^{cs} = -\mathbf{M}_{mm'}^{sc} = \mathbf{M}_m^s \delta_{mm'}. \tag{4.32}$$

Since the scattering matrix only depends on the difference in the azimuth between the incoming and outgoing angles, the azimuth Fourier modes separate, ie. $\mathbf{M}$ depends only on m rather than both m and m'. This allows the azimuth modes to be solved separately, reducing the computational burden. In the scalar radiative transfer case the scattering function depends only on $\cos m(\phi' - \phi)$, therefore the $\mathbf{M}_{mm'}^{cs}$ and $\mathbf{M}_{mm'}^{sc}$ terms are zero and the cosine and sine terms do not mix.

Equation 4.17 has some special symmetries. The upper left and lower right two by two blocks are even functions in $\Delta\phi$, while the upper right and lower left blocks are

odd functions. Therefore the cosine matrices have off-diagonal blocks of zeros and the sine matrices have diagonal blocks of zeros. Another statement of this symmetry is that negating ϕ and ϕ' results in negating the off diagonal blocks. This allows the trivial calculation of the scattering matrix for $\pi < \Delta\phi \le 2\pi$ from the values for $0 < \Delta\phi \le \pi$. Another symmetry is negating μ and μ' results in negating the off diagonal blocks. This is due to the invariance of the scattering matrix with rotation of the coordinate system ($\mu \to -\mu$ and $\phi \to -\phi$): $\mathbf{M}(\mu, \mu', \phi' - \phi) = \mathbf{M}(-\mu, -\mu', \phi - \phi')$.

For a given azimuth mode m the cosine and sine scattering matrices can be combined into a single eight-by-eight scattering matrix

$$
\begin{pmatrix} I^c \\ Q^c \\ U^c \\ V^c \\ I^s \\ Q^s \\ U^s \\ V^s \end{pmatrix}_{out} = \left(\begin{array}{cc|cc|cc|cc} M_{11}^c & M_{12}^c & 0 & 0 & 0 & 0 & M_{13}^s & M_{14}^s \\ M_{21}^c & M_{22}^c & 0 & 0 & 0 & 0 & M_{23}^s & M_{24}^s \\ \hline 0 & 0 & M_{33}^c & M_{34}^c & M_{31}^s & M_{32}^s & 0 & 0 \\ 0 & 0 & M_{43}^c & M_{44}^c & M_{41}^s & M_{42}^s & 0 & 0 \\ \hline 0 & 0 & -M_{13}^s & -M_{14}^s & M_{11}^c & M_{12}^c & 0 & 0 \\ 0 & 0 & -M_{23}^s & -M_{24}^s & M_{21}^c & M_{22}^c & 0 & 0 \\ \hline -M_{31}^s & -M_{32}^s & 0 & 0 & 0 & 0 & M_{33}^c & M_{34}^c \\ -M_{41}^s & -M_{42}^s & 0 & 0 & 0 & 0 & M_{43}^c & M_{44}^c \end{array} \right) \begin{pmatrix} I^c \\ Q^c \\ U^c \\ V^c \\ I^s \\ Q^s \\ U^s \\ V^s \end{pmatrix}_{in}
$$

$$(4.33)$$

The blocks of zeros in this scattering matrix allows a computationally efficient rearrangement of the cosine and sine modes of Stokes parameters. Writing the Stokes radiance vectors as

$$
\hat{\mathbf{I}}^c = \begin{pmatrix} I^c \\ Q^c \\ U^c \\ V^c \end{pmatrix} \qquad \hat{\mathbf{I}}^s = \begin{pmatrix} I^s \\ Q^s \\ U^s \\ V^s \end{pmatrix} \tag{4.34}
$$

then the $\hat{\mathbf{I}}^c$ and $\hat{\mathbf{I}}^s$ radiance vectors decouple. The rows and columns of the scattering matrix rearrange to give two separate four-by-four matrices

$$
\hat{\mathbf{I}}^c_{out} = \begin{pmatrix} M_{11}^c & M_{12}^c & M_{13}^s & M_{14}^s \\ M_{21}^c & M_{22}^c & M_{23}^s & M_{24}^s \\ -M_{31}^s & -M_{32}^s & M_{33}^c & M_{34}^c \\ -M_{41}^s & -M_{42}^s & M_{43}^c & M_{44}^c \end{pmatrix} \hat{\mathbf{I}}^c_{in} \tag{4.35}
$$

$$
\hat{\mathbf{I}}^s_{out} = \begin{pmatrix} M_{11}^c & M_{12}^c & -M_{13}^s & -M_{14}^s \\ M_{21}^c & M_{22}^c & -M_{23}^s & -M_{24}^s \\ M_{31}^s & M_{32}^s & M_{33}^c & M_{34}^c \\ M_{41}^s & M_{42}^s & M_{43}^c & M_{44}^c \end{pmatrix} \hat{\mathbf{I}}^s_{in} \tag{4.36}
$$

Conventionally the solar azimuth is set to zero, so both the solar and thermal sources of radiation are even functions and unpolarized, or I^c is the only non-zero element. Since the $\hat{\mathbf{I}}^c$ and $\hat{\mathbf{I}}^s$ radiance vectors are decoupled, further scattering leaves the sine mode radiance vector zero. Therefore, only the first four-by-four Fourier scattering matrix need be considered. For the azimuthally symmetric case ($m = 0$) the sine terms in the scattering matrix are zero and the U and V Stokes parameters are zero, in this case, the two-by-two scattering matrix may be used.

If the solar azimuth is zero the direction of the incident solar radiation is $\mu_o = \cos\theta_o, \phi_o = \pi$. The rearranged Stokes vector for the solar "pseudo source" is then

$$\hat{\sigma}(\mu_j) = \frac{F_o}{\mu_o} \frac{\tilde{\omega}}{4\pi} exp(\frac{-\tau}{\mu_o}) \begin{pmatrix} M_{11}^c \\ M_{21}^c \\ M_{31}^s \\ M_{41}^s \end{pmatrix} \qquad (4.37)$$

where the scattering matrix elements are evaluated as described above for the quadrature angles μ_j and the solar angle μ_o.

The Matrix Formation of the Equation of Transfer

Using the notation $\hat{\mathbf{I}}_{mj}^{\pm} = \hat{\mathbf{I}}_m^c(\tau, \pm\mu_j)$ the discretized radiative transfer equation becomes.

$$\pm \mu_j \frac{d\hat{\mathbf{I}}_{mj}^{\pm}}{d\tau} = -\hat{\mathbf{I}}_{mj}^{\pm} + \hat{\sigma}_{mj}^{\pm} + \frac{\tilde{\omega}}{4\pi} \sum_{j=1}^{N} c_m w_{j'} [\mathbf{M}_{mjj'}^{\pm+} \hat{\mathbf{I}}_{mj'}^{+} + \mathbf{M}_{mjj'}^{\pm-} \hat{\mathbf{I}}_{mj'}^{-}]. \qquad (4.38)$$

where the plus and minus superscripts refer to the quadrature angles in the downward (+) and upward (−) directions respectively.

The notation can be simplified by removing the subscripts and writing the equation using matrices and vectors. The dependencies on both τ and m is taken to be understood. The radiative transfer equation will be numerically solved for each azimuth mode m. The Stokes radiance vectors for each quadrature angle in a hemisphere are combined into one long radiance vector

$$\bar{I} = \begin{pmatrix} \hat{\mathbf{I}}_{j=1} \\ \hat{\mathbf{I}}_{j=2} \\ \vdots \\ \hat{\mathbf{I}}_{j=N} \end{pmatrix}, \qquad \hat{\mathbf{I}}_j = \begin{pmatrix} \hat{I}_j^c \\ \hat{Q}_j^c \\ \hat{U}_j^c \\ \hat{V}_j^c \end{pmatrix} \qquad (4.39)$$

The length of this vector is $4 \times N$. The individual scattering matrices for each pair of angles $\mu_j, \mu_{j'}$ are combined to form a scattering matrix that operates on a radiance vector to produce another vector, which is the the discrete equivalent of integration over all angles. In matrix notation the radiative transfer equation becomes

$$\pm \mathbf{D} \frac{d\bar{I}^\pm}{d\tau} = -\bar{I}^\pm + \mathbf{C}^{\pm+} \bar{I}^+ + \mathbf{C}^{\pm-} \bar{I}^- + \bar{\sigma}^\pm. \tag{4.40}$$

The elements of the matrices $\mathbf{D}$ and $\mathbf{C}^{\pm\pm}$ are

$$|\mathbf{D}|_{jj'ii'} = \mu_j$$

$$|\mathbf{C}^{\pm\pm}|_{jj'ii'} = \frac{\tilde{\omega}}{4\pi} c_m w_{j'} |\mathbf{M}^{\pm\pm}_{mrjj'}|_{ii'} \tag{4.41}$$

where the i and i' indices refer to the Stokes parameters.

4.5   Integrating the Radiative Transfer Equation

4.5.1   Finite Difference

The radiative transfer equation (4.40) is a matrix first order ordinary differential equation. One method of numerically integrating the differential equations to approximate the derivative $(\frac{dI}{d\tau})$ with a finite difference scheme. The simplest difference scheme is

$$\frac{dI}{d\tau} = \frac{I(\tau) - I(\tau + \Delta\tau)}{\Delta\tau}. \tag{4.42}$$

Although simple, this method is very accurate if $\Delta\tau$ is chosen small enough. Defining $I_o = \bar{I}(\tau)$ and $I_1 = \bar{I}(\tau + \Delta\tau)$ equation (4.40) becomes

$$I_1^+ - I_o^+ = \Delta\tau \mathbf{D}^{-1}[-I_o^+ + \mathbf{C}^{++} I_o^+ + \mathbf{C}^{+-} I_1^- + \sigma^+]$$

$$I_1^- - I_o^- = \Delta\tau \mathbf{D}^{-1}[-I_1^- + \mathbf{C}^{-+} I_0^+ + \mathbf{C}^{--} I_1^- + \sigma^-] \tag{4.43}$$

The finite difference scheme requires the right hand side of the equation be defined in terms of the discretized values I_o and I_1. This is nearly the same since $\Delta\tau$ is chosen very small. The last equation can be arranged to express the radiation emerging from a this layer in term of the incident radiation.

$$I_1^+ = [\bar{\bar{1}} - \Delta\tau \mathbf{D}^{-1}(\bar{\bar{1}} - \mathbf{C}^{++})] I_o^+ + \Delta\tau \mathbf{D}^{-1} \mathbf{C}^{+-} I_1^- + \Delta\tau \mathbf{D}^{-1} \sigma^+ \tag{4.44}$$

$$I_0^- = [\bar{\bar{1}} - \Delta\tau \mathbf{D}^{-1}(\bar{\bar{1}} - \mathbf{C}^{--})] I_1^- + \Delta\tau \mathbf{D}^{-1} \mathbf{C}^{-+} I_0^+ + \Delta\tau \mathbf{D}^{-1} \sigma^- \tag{4.45}$$

$$\downarrow I_o^+ \qquad\qquad\qquad \uparrow I_0^-$$

$$R^\pm \quad T^\pm \quad S^\pm$$

$$\uparrow I_1^- \qquad\qquad\qquad \downarrow I_1^+$$

Figure 4.3: Illustration of the interaction principle. The I_o^+ and I_1^- on the left represent incident radiation. The I_0^- and I_1^+ on the right represent the radiation leaving the medium. R, T, and S are the reflection, transmission, and source terms respectively.

4.5.2 The Interaction Principle

The interaction principle is a simple method of expressing the linear interaction of radiation with a medium. Radiation emerging from any medium can be expressed in term of the incident radiation plus the radiation generated within the medium. The matrix formulation for the interaction principle is

$$I_1^+ = T^+ I_o^+ + R^+ I_1^- + S^+$$

$$I_0^- = T^- I_1^- + R^- I_0^+ + S^- \tag{4.46}$$

where T is the transmission matrix, R is the reflection matrix, and S is the source vector. The finite difference form of the radiative transfer equation (4.40) is the same form as the interaction principle. The reflection and transmission matrices and the source vectors for the infinitesimal layer can be related to the local properties of the medium by

$$T^\pm = [\bar{\bar{1}} - \Delta\tau \mathbf{D}^{-1}(\bar{\bar{1}} - \mathbf{C}^{\pm\pm})]$$

$$R^\pm = \Delta\tau \mathbf{D}^{-1} \mathbf{C}^{\pm\mp}$$

$$S^\pm = \Delta\tau \mathbf{D}^{-1} \sigma^\pm. \tag{4.47}$$

Relating the radiative transfer equation to the interaction principle is normally termed initialization. There are several initialization methods, the one used here is sometimes called the infinitesimal generator initialization.

The Adding Algorithm

The previous section have shown how the coefficients of the radiative transfer equation relate to the reflection matrices, transmission matrices, and source vectors for infinitesimal layers. Now an integration procedure is needed to relate the properties of the infinitesimal layers to the properties of an atmosphere composed of many infinitesimal layers. With the reflection and transmission matrices and the source vectors for the entire medium, the interaction principle can be applied to the incident radiation at the boundaries to calculate the outgoing radiation. Radiation fields inside the medium may also be calculated from the incident radiation and the matrices and source vectors for the medium above and below the level of interest.
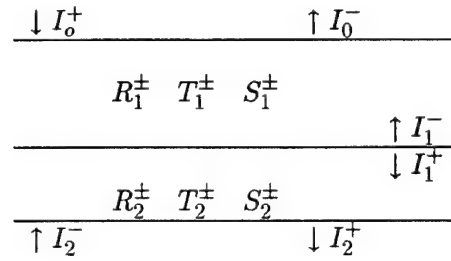
Figure 4.4: Illustration of adding principle. The properties of layers 1 and 2 are combined to make the reflection, transmission, and source term for the new layer.

The interaction principle is now used to combine (add) two layers. The reflection and transmission matrices and the source vector for this new double thick layer can be expressed in terms of the matrices and vectors of the individual layers. Starting with the interaction principle for the two layers, Figure 4.4, the radiances at the interface are eliminated and the equations rearranged to form the interaction principle for the new layer, resulting in

$$R_T^+ = R_2^+ + T_2^+\Gamma^+ R_1^+ T_2^-, \qquad R_T^- = R_1^- + T_1^-\Gamma^- R_2^- T_1^+$$

$$T_T^+ = T_2^+\Gamma^+ T_1^+, \qquad T_T^- = T_1^-\Gamma^- T_2^-$$

$$S_T^+ = S_2^+ + T_2^+\Gamma^+(S_1^+ + R_1^+ S_2^-), \qquad S_T^- = S_1^- + T_1^-\Gamma^-(S_2^- + R_2^- S_1^+)$$

$$\Gamma^+ = [1 - R_1^+ R_2^-]^{-1}, \qquad \Gamma^- = [1 - R_2^- R_1^+]^{-1}. \tag{4.48}$$

By similar manipulation, the internal radiances (I_1^+, I_1^-) may be expressed in term of the radiance incident upon the two layers as

$$I_1^+ = \Gamma^+[R_1^+ T_2^- I_2^- + T_1^+ I_0^+ + R_1^+ S_2^- + S_1^+]$$

$$I_1^- = \Gamma^-[R_2^- T_1^+ I_0^+ + T_2^- I_2^- + R_2^- S_1^+ + S_2^-]. \tag{4.49}$$

Doubling Algorithm

The radiative properties for a finite layer could be calculated by building on one layer at a time using the adding algorithm, however, the doubling algorithm provides a much faster method of building up a thick layer from many identical thin layers. If all the thin layers have an optical depth of $\Delta\tau$, then combining the first two layers yields a layer with optical depth $2\Delta\tau$. Since all the thin layers are identical, all the $2\Delta\tau$ layers will be the same. Two $2\Delta\tau$ layers are now added together to form a $4\Delta\tau$ thick layer. After N of these doubling steps the layer is built up to an optical depth of $2^N \Delta\tau$. Using this method more than one million thin layers can be combined in 20 steps. The doubling formulae for the reflection and transmission matrices are

$$R_{2N}^+ = R_N^+ + T_N^+ \Gamma^+ R_N^+ T_N^-, \qquad R_{2N}^- = R_N^- + T_N^- \Gamma^- R_N^- T_N^+$$

$$T_{2N}^+ = T_N^+ \Gamma^+ T + N^+, \qquad T_{2N}^- = T_N^- \Gamma^- T_N^-$$

$$\Gamma^+ = [1 - R_N^+ R_N^-]^{-1}, \qquad \Gamma^- = [1 - R_N^- R_N^+]^{-1}. \tag{4.50}$$

The doubling, adding, and finite generator initialization algorithms used here were developed by Grant and Hunt (1969). The doubling method so far requires all the layers be uniform.

The solar pseudo-source has an exponential dependence with optical depth. Wiscombe (1976) extended the doubling method to incorporate these sources. With exponential sources the source at a deeper optical depth is the same as the source at a shallower optical depth except for a multiplicative factor. This introduces a factor into the formula for adding the sources of two layers

$$S_{2N}^+ = \gamma^N S_N^+ + T_N^+ \Gamma^+ (S_N^+ + R_N^+ S_N^- \gamma^N)$$

$$S_{2N}^- = S_N^- + T_N^- \Gamma^- (S_N^- \gamma^N + R_N^- S_N^+)$$

$$\gamma = exp(-\Delta\tau/\mu_o). \tag{4.51}$$

4.5.3   The Boundaries

The effect of the surface may also be calculated using the interaction principle. The ground is treated as a layer with transmission of unity, no source, and a reflection. The ground is assumed to be a Lambertian surface, and therefore emits and reflects equally in all directions. The reflected radiance is the incident flux times the ground albedo divided by π. Reflected radiance is assumed to be unpolarized. Radiation emitted from the ground is the incident radiance on the lower boundary. The internal radiance algorithm is used to calculate the downwelling radiance below the atmosphere, but above the ground

$$I_a^- = \Gamma^+ I_a^{+'}$$

$$I_a^{+'} = T_a^+ I_o^+ = R_a^+ I_g^- + S_a^+$$

$$\Gamma^+ = [1 - R_a^+ R_g]^{-1} \tag{4.52}$$

where a refers to the total atmosphere layer and g refers to the ground. The downwelling radiation from the atmosphere is what the radiation would be with no ground $I_a^{+'}$ multiplied by the multiple reflection factor Γ^+.

The radiance upwelling from the top of the atmosphere is found by adding the atmosphere layer to the ground layer

$$I_o^- = R_T^- I_o^+ + T_T^- I_g^- = S_T^-$$

$$R_T^- = R_a^- + T_a^- \Gamma^- R_g T_a^+$$

$$T_T^- = T_a^- \Gamma^-$$

$$S_T^- = S_a^- + T_a^- \Gamma^- R_g S_a^+$$

$$\Gamma^- = [1 - R_g R_a^+]^{-1}. \tag{4.53}$$

4.6   Testing the Polarized Radiative Transfer Model

A convenient test of the model is to compare the results to the tables by Coulson et al. (1960). The Coulson tables list the outgoing radiation for a conservative sunlit Rayleigh atmosphere. Both the upwelling and downwelling Stokes radiance vectors (I, Q, U) are provided in terms of different optical depths, solar angles, and surface albedos. Comparisons were made with two cases of varying optical depth and solar angles. The radiative

Table 4.1: Comparison of model results with Coulson tables for a homogeneous Rayleigh atmosphere. The upwelling radiance at azimuth angle of 90° for optical depth of 1, solar zenith angle of 0.8, and surface albedo of 0.25. Coulson defines Q with a sign opposite of that used in this model.

	Coulson			Model		
μ	I	Q	U	I	Q	U
0.06	0.39887	0.05099	0.24758	0.395222	-0.05162	0.246095
0.16	0.40894	0.03988	0.23375	0.406471	-0.04037	0.232832
0.28	0.40482	0.02766	0.20918	0.403094	-0.02801	0.208589
0.4	0.3938	0.0157	0.17114	0.392471	-0.01596	0.180708
0.64	0.37248	-0.00774	0.12476	0.371605	0.007621	0.124514
0.84	0.36147	-0.02681	0.0759	0.360826	0.026772	0.075762
0.96	0.35776	-0.03808	0.03609	0.357222	0.038087	0.036026
1	0.35694	-0.04181	0	0.356435	0.041833	0

transfer model was run with 16 angles using the extra angle quadrature mode (8 angles machine generated and 8 user supplied) and azimuth modes up to $m = 2$. The upwelling and downwelling radiances were compared at azimuth angles of 0, 90, and 180° (U is zero at 0 and 180°). Table 4.1 compares the upwelling radiance at azimuth angle of 90° for a homogeneous Rayleigh atmosphere with optical depth of 1, solar zenith angle of 0.8, and surface albedo of 0.25. Note: Coulson define Q with a sign opposite of that used in this model. Table 4.2 compares the downwelling radiance at azimuth angle of 180° for optical depth of 1, solar zenith angle of 0.6, and surface albedo of 0. Table 4.3 summarizes the two cases, the average and maximum differences between the model and Coulson tables are shown.

Table 4.2: Comparison of model results with Coulson tables for a homogeneous Rayleigh atmosphere. The upwelling radiance at azimuth angle of 180° for optical depth of .15, solar zenith angle of 0.6, and surface albedo of 0. U is zero at 0 and 180°.

	Coulson		Model	
μ	I	Q	I	Q
0.06	0.29264	0.05675	0.288185	-0.05806
0.16	0.18709	0.05065	0.184099	-0.05142
0.28	0.11837	0.04489	0.116442	-0.04528
0.4	0.08206	0.0414	0.080709	-0.04158
0.64	0.04656	0.03616	0.04583	-0.03608
0.84	0.03438	0.03041	0.033906	-0.03027
0.96	0.03347	0.02387	0.033064	-0.02373
1	0.03859	0.01662	0.038152	-0.01654

Table 4.3: Summary of differences between the model and Coulson tables. The average and maximum absolute differences of the radiances over the eight zenith angles at azimuths of 0, 90, 180° and both upwelling and downwelling directions.

Optical Depth	Solar μ	Surface Albedo	Average Error			Maximum Error		
			I	Q	U	I	Q	U
1	0.8	0.25	0.00108	0.00014	0.00024	0.00399	0.00063	0.00149
0.15	0.6	0	0.00174	0.00057	0.00021	0.00519	0.00211	0.00193

4.7 Model Results
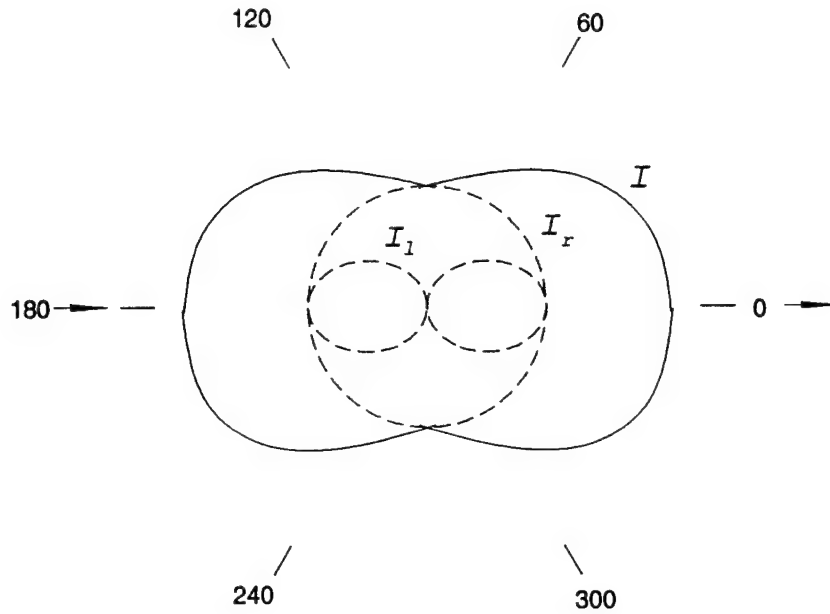
Figure 4.5: Scattering pattern for a Rayleigh particle. Incident radiation is unpolarized. I_l is the component parallel to the scattering plane and I_l is the component perpendicular to the scattering plane. The pattern is rotationally symmetric about the direction of the incident radiation.

For unpolarized incident radiation, the angular distribution of Rayleigh scattering is shown in Figure 4.5. The distribution has rotational symmetry around both $\Theta = 0 - 180°$ and $\Theta = 90°$. Radiation scattered directly forward or backward remains totally unpolarized. Radiation scattered at $\Theta = 90°$ has half the intensity of forward and back scattered radiation, but is totally polarized. The definition of the Rubenson degree of polarization (Coulson, 1988) comes from this relationship

$$P = \frac{I_r - I_l}{I_r + I_l}. \tag{4.54}$$

This definition of linear polarization ($V = 0$) is convenient when in the plane of the sun's vertical, since it is easy to calculate and allows for both positive and negative polarization. However, at directions that are not in the plane of the sun's vertical the Rubenson definition gives erroneous results because I_r and I_l with respect to the viewing direction

are not the same as I_r and I_l with respect to the scattering plane. At directions not in the sun's vertical the state of linear polarization in given by

$$P = \frac{[(I_r - I_l)^2 + U^2]^{.5}}{I_r + I_l}.$$ (4.55)

with

$$U = (I_r - I_l)\tan 2\chi$$ (4.56)

where χ is the angle the plane of polarization taken with respect to the vertical direction. The degree of polarization is normally positive due to the square root relation. Only with $U = 0$ does a negative sign of P have meaning. Since $U = 0$ in the suns vertical, P can become negative the Rubenson definition applies. In the most general sense polarization is not linear ($V \neq 0$), using the (I, Q, U, V) representation the degree of polarization becomes

$$P = \frac{(Q^2 + U^2 + V^2)^{\frac{1}{2}}}{I}.$$ (4.57)

This representation of polarization does not allow negative polarization, but allows calculation of the degree of polarization at all angles. It is the relationship used to calculate polarization for the sky hemisphere.

Figure 4.6 shows the radiation intensity for a pure Rayleigh atmosphere. The solar zenith angle is 78.5°, optical depth is .05 and surface albedo is zero. This is the familiar Rayleigh pattern for atmospheric radiation intensity with it's nearly concentric contours and the brightening near the horizon. Figure 4.7 shows the sky polarization for the same solar angle, optical depth, and surface albedo. Due to the low sun angle and relatively small optical depth there is little multiple scatter and a 95% polarization band occurs close to the 90° azimuth.

Figures 4.8 and 4.9 show the sky polarizations for solar zenith angles of 66.4° and 23.1° respectively. For these two cases, the optical depth was increased to .15, but surface albedo is held at zero. In both cases we see the effect of scattering angle as the maximum polarization band remains close to 90° from the sun. The maximum polarization band shifts across the sky and the contours become more concentric with decreasing solar zenith angle. If the sun were at the zenith, the maximum polarization would be at the horizon and the polarization contours would be symmetric about the solar zenith.

Figure 4.6: Distribution of the transmitted intensity over the hemisphere of the sky. The solar position is azimuth = 0 and zenith angle = 78.5°, optical depth is .05 and surface albedo is zero. Only half the hemisphere is shown, the other half being the mirror image of this one. The plane of the sun's vertical is represented by the straight bottom line, with 0 being the zenith. The outside semicircle represents the horizon.

Figure 4.10 shows the hemispheric radiation intensity with the introduction of haze into the atmosphere. Here the solar zenith angle is again 23.1° and the surface albedo is zero. The optical depth is also .15, however .10 is due to Rayleigh scattering and .05 is due to the haze. The intensity close to the sun sharply increases due to the strong forward scatter for the haze. Intensity at all other angles also increases due to increased multiple scattering. Figure 4.11 shows the corresponding graph for the sky polarization. The band of maximum polarization does not change location much, although there is a decrease in the maximum intensity. There is also a larger area of low polarization near the solar position.

To closely examine the effects of the parameters that affect the sky radiation intensity and polarization, the directions $\phi - \phi_o = 0$ and $\phi - \phi_o = 180$ were used. Figure 4.12 shows the effect of increasing Rayleigh optical depth on the sky light intensity and polarization. For this exercise, the solar zenith angle was held constant at 50° (solar elevation = 40°) and the surface albedo was zero. The sky intensity overall shows a minimum at high

Figure 4.7: Distribution of the degree of polarization over the hemisphere of the sky. The solar position is azimuth = 0 and zenith angle = 78.5°, optical depth is .05 and surface albedo is zero.

elevation angles and a maximum at low elevation angles ($\theta < 40°$ and $\theta > 140°$). This is a result of a plane parallel atmosphere. At high elevation angles, the path length through the atmosphere is short and not much radiation is scattered from the direct solar beam into the viewing direction. At low elevation angles, the path length through the atmosphere increases and more radiation is scattered from the direct solar beam into the viewing direction. As optical depth increases, sky radiation intensity increases at all elevations, since more radiation is scattered out of the direct solar beam with increased optical depth. The increase is the most significant in the sun's hemisphere and close to the horizon since Rayleigh scattering is stronger in the forward and backward directions. The effects on polarization are more complicated. For a purely single scattering Rayleigh case, there would be totally unpolarized radiation (zero polarization) at the solar elevation and totally polarized radiation (polarization = 1) at 90° above the solar angle. However, the atmosphere is not single scattering. Multiple scattering has the effect of converting perpendicular polarized radiation into parallel polarized radiation. Therefore at elevations close to the solar position, multiple scattering will cause the observed polarization to
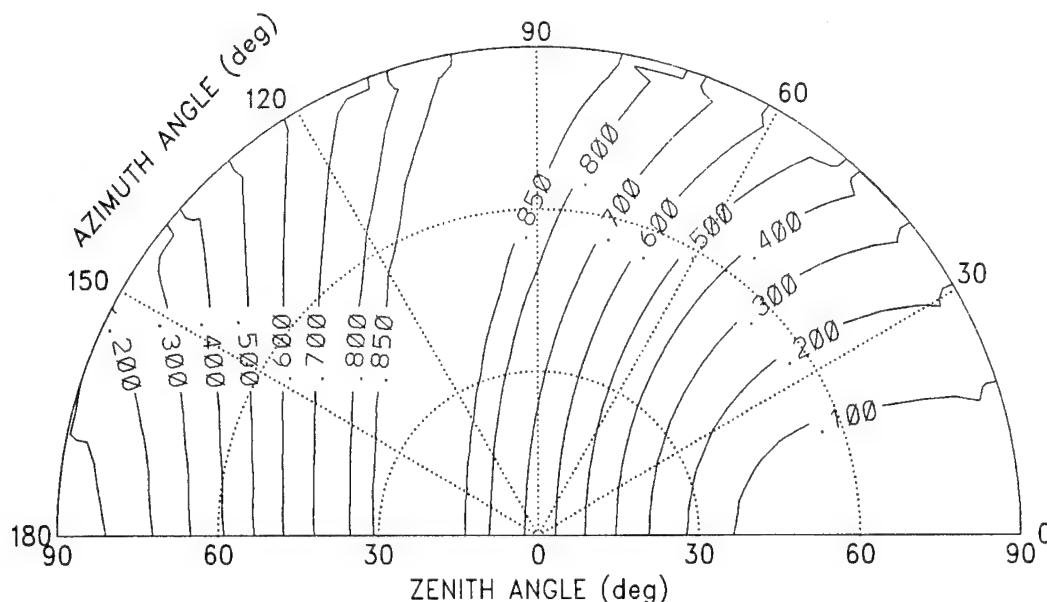
Figure 4.8: Distribution of the degree of polarization over the hemisphere of the sky. The solar position is azimuth = 0 and zenith angle = 66.4°, optical depth is .15 and surface albedo is zero.

become negative. At elevations close to 90° from the solar position, multiple scattering will reduce the observed polarization below the maximum of 1 for single scatter. Figure 4.12 shows that as the optical depth increases, and therefore multiple scatter increases, the polarization near the sun becomes more negative, and the polarization decreases at 90° from the sun.

Figure 4.13 shows the effects of surface reflection. As the surface albedo increases, there is an almost uniform increase in intensity for all elevation angles, this increase is of less magnitude than that for increasing the optical depth. The intensity increase is a result of radiation being reflected from the ground and then being scattered into the viewing direction. The polarization is effected the most at angles 90° from the solar position. Increasing surface reflection decreases the polarization maximum significantly. At elevations close to the solar position there is very little change in polarization. This is due to the surface acting as a lambertian reflector. Radiation reflected from the surface back into the atmosphere will be unpolarized, and induce a depolarization effect at all angles. There will be a large effect 90° from the sun at the polarization max, but since the polarization near the sun is already close to zero the effect here will be less noticeable.
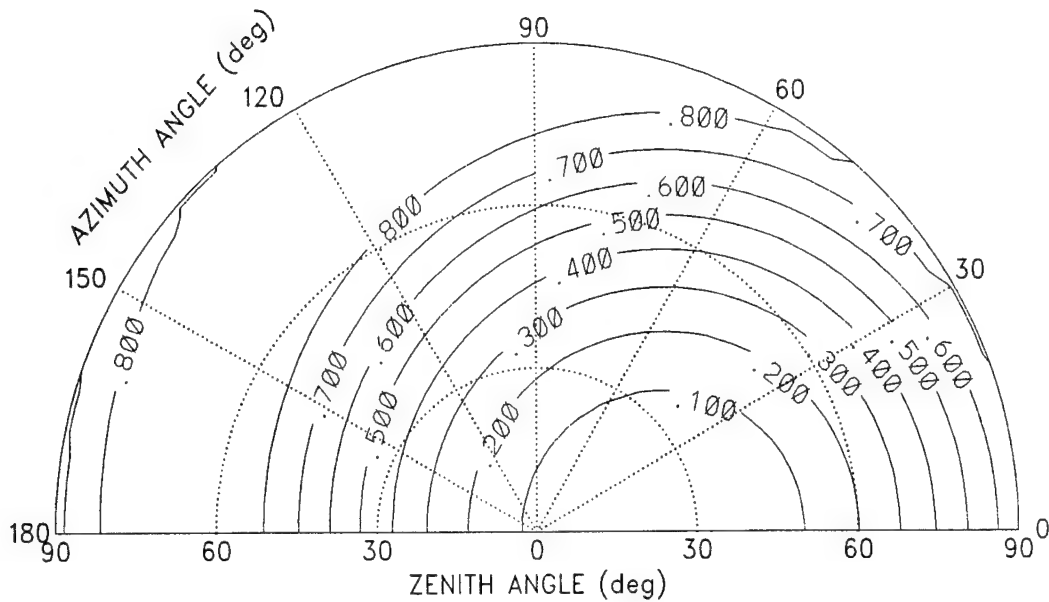
Figure 4.9: Distribution of the degree of polarization over the hemisphere of the sky. The solar position is azimuth = 0 and zenith angle = 23.1°, optical depth is .15 and surface albedo is zero.

Figure 4.14 shows the effect solar zenith angle has on the sky light intensity and polarization. As the solar zenith angle decreases (solar position closer to 90°) the intensity pattern becomes more symmetric. As the sun changes position, the areas of maximum and minimum polarization track the solar position. As the solar position moves higher into the sky the area of negative polarization near the solar position becomes less negative, due to optical path decreasing, and therefore less multiple scattering. The opposite happens at 90° from the solar position. As the solar position rises into the sky the area of maximum polarization now has an increasing optical path and the resulting increase in multiple scattering causes the observed maximum polarization to decrease in magnitude.

Figure 4.15 shows the effect of adding haze to the bottom kilometer in the atmosphere. For this test the Rayleigh scatter was held at .10 and the optical depth due to the haze was increased from .01 up to .10. The solar zenith angle was 50° and the surface albedo was zero. A Deirmendjian Haze-L distribution (Deirmendjian, 1969) was used with a complex index of refraction $m = 1.50 - .000i$ at $\lambda = 520nm$. The scattering phase function was determined by mie calculations, particles are assumed to be randomly oriented. The
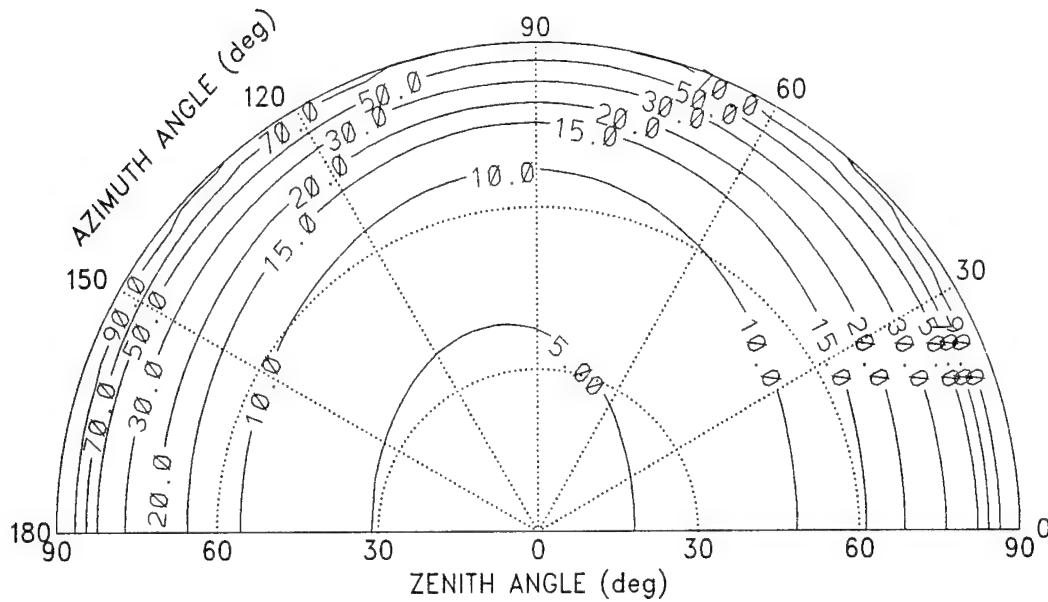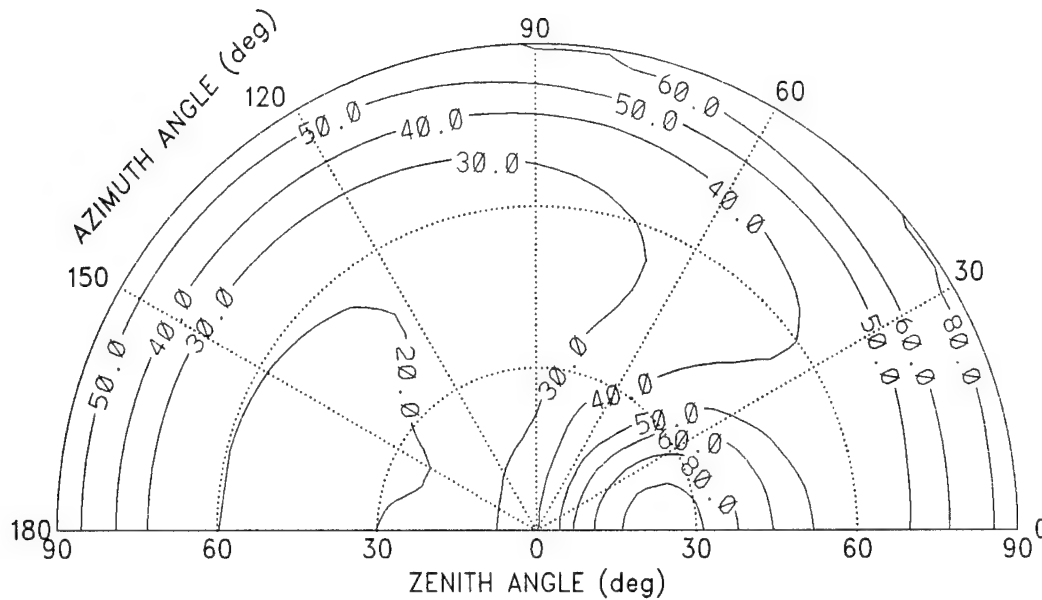
Figure 4.10: Distribution of radiation intensity over the hemisphere of the sky. The solar position is azimuth = 0 and zenith angle = 23.1°, Rayleigh optical depth is .10, the haze optical depth is .05, and surface albedo is zero.

intensity phase function is shown in Figure 4.16 with the phase function for Rayleigh scattering. We see the haze has very strong forward scattering peak from 0° through 40° and the backscatter is less than that for Rayleigh scattering. The strong forward scattering of the haze shows up readily in Figure 4.15 as the narrow peak in intensity near the sun. Away from the solar position, the increase in intensity falls off rapidly. Haze de-polarizes the the Rayleigh atmosphere at all angles. In the vicinity of the solar position, multiple Rayleigh scattering normally introduces a negative polarization, but haze over shadows this effect and the resultant polarization is close to zero. At 90° from the solar position there is a larger de-polarization as the optical depth of the haze increases. The point of maximum polarization also moves further from the solar position as the haze optical depth increases. This is a result of the haze forward scattering depolarizing the area closer to the sun to a greater degree than those area farther away from the sun.
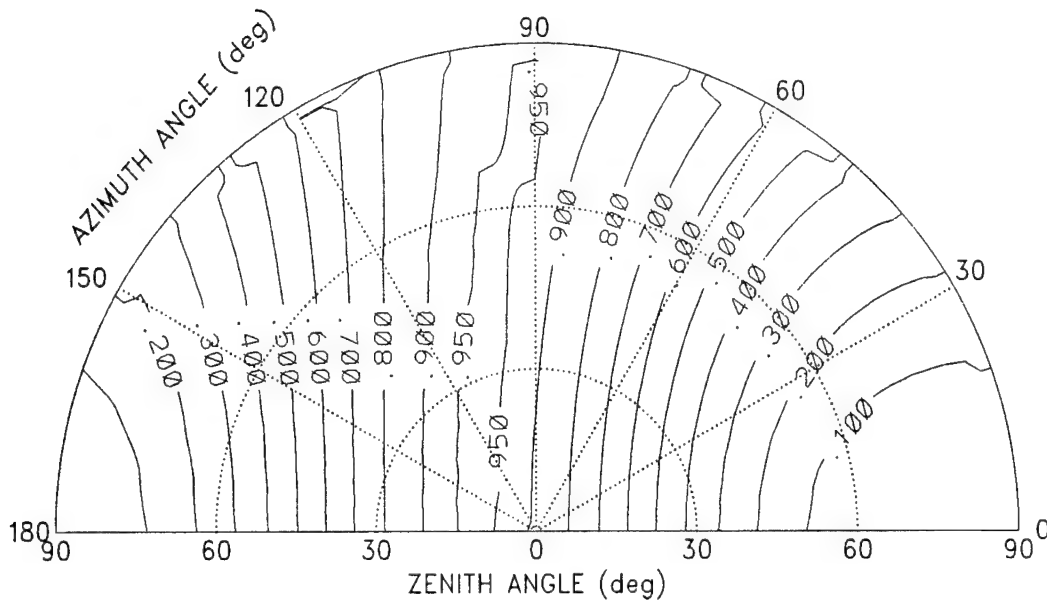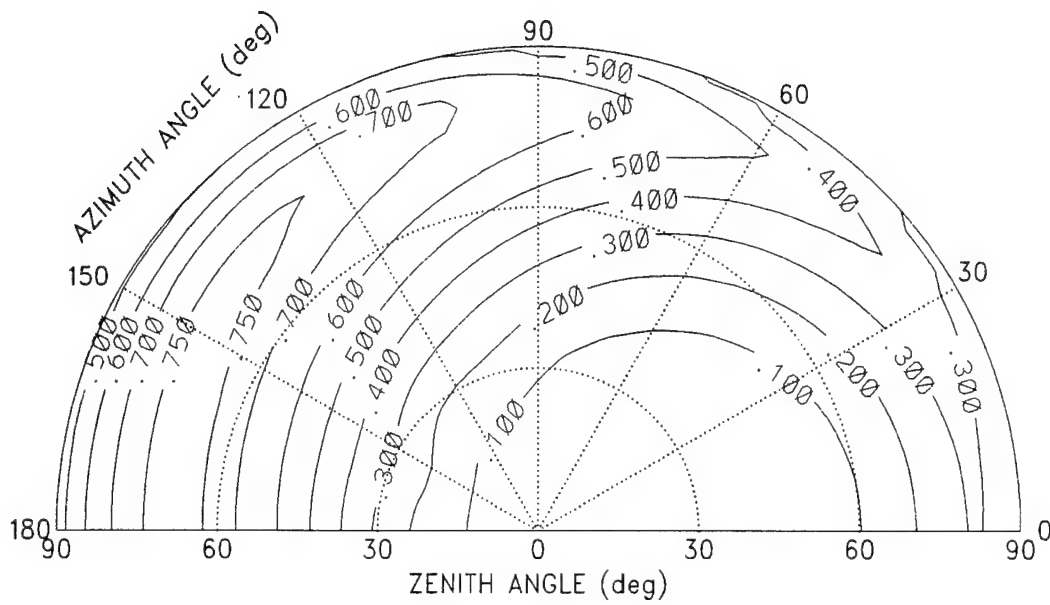
Figure 4.11: Distribution of the degree of polarization over the hemisphere of the sky. The solar position is azimuth = 0 and zenith angle = 23.1°, Rayleigh optical depth is .10, the haze optical depth is .05, and surface albedo is zero.
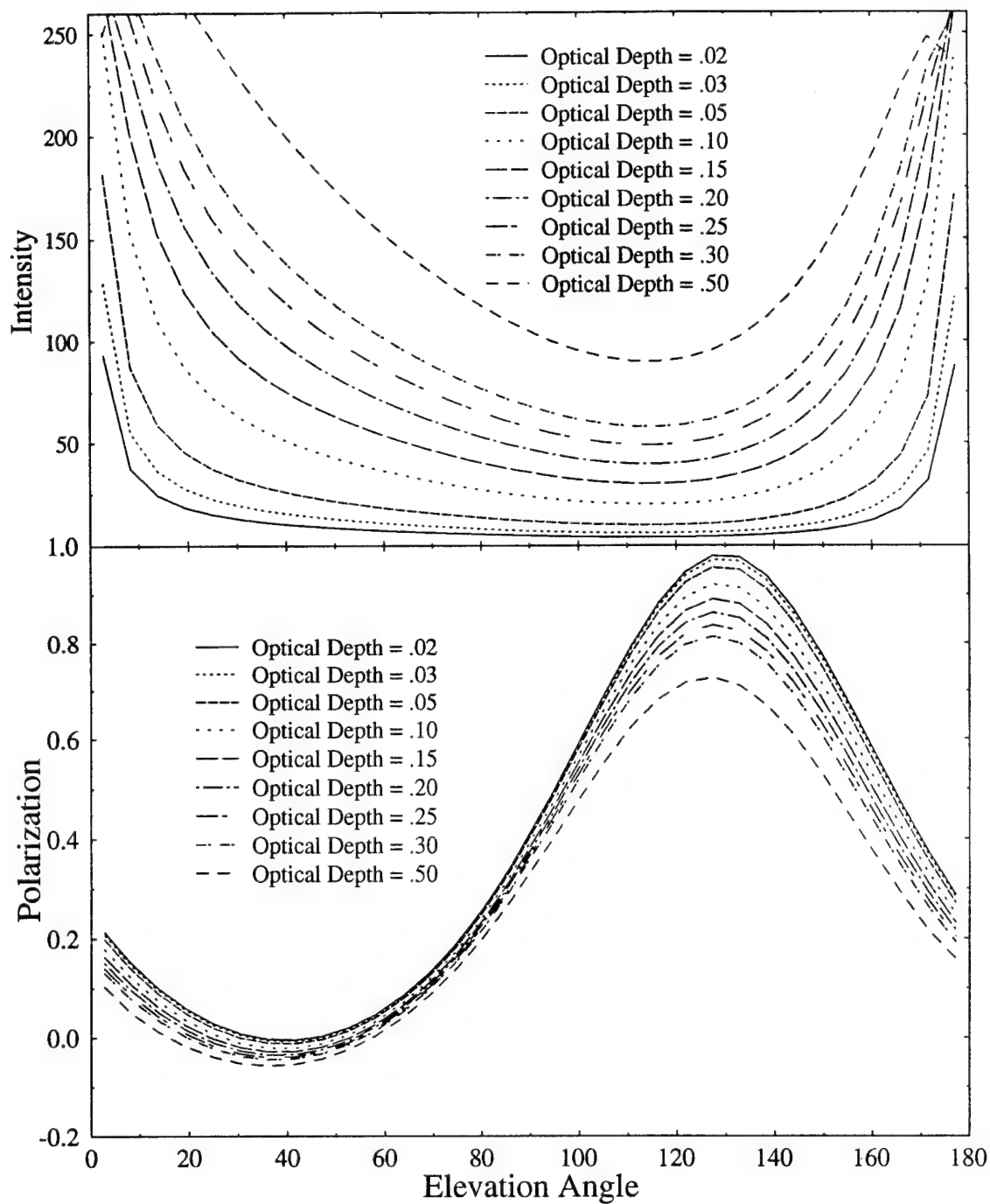
Figure 4.12: Effects of changing Rayleigh optical depth on sky radiation intensity and polarization. The solar position is held at 40°, and surface albedo is zero.
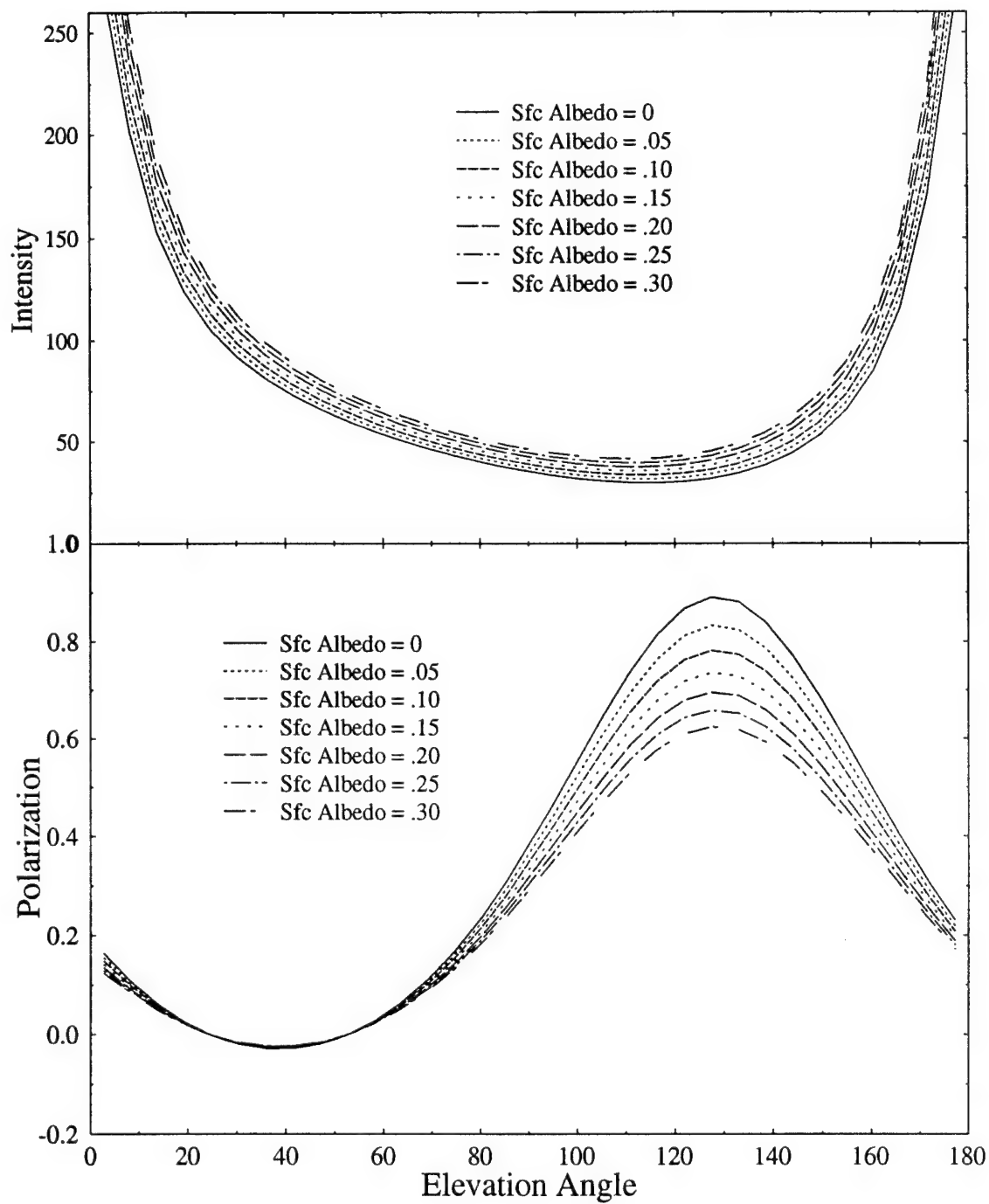
Figure 4.13: Effect of changing surface albedo on sky radiation intensity and polarization. Solar position is held at 40° and the optical depth is .15.
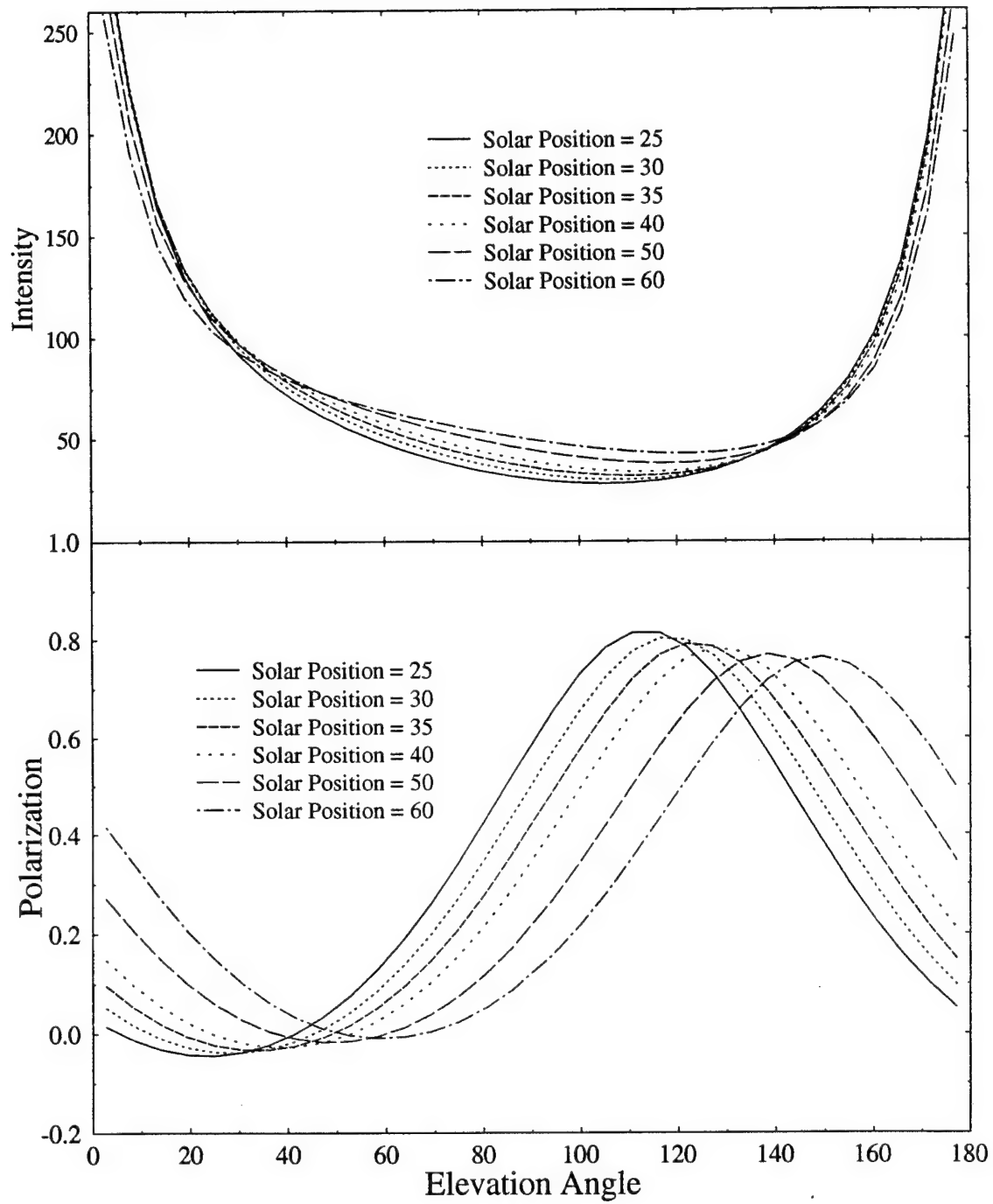
Figure 4.14: Effects of changing the solar zenith angle.
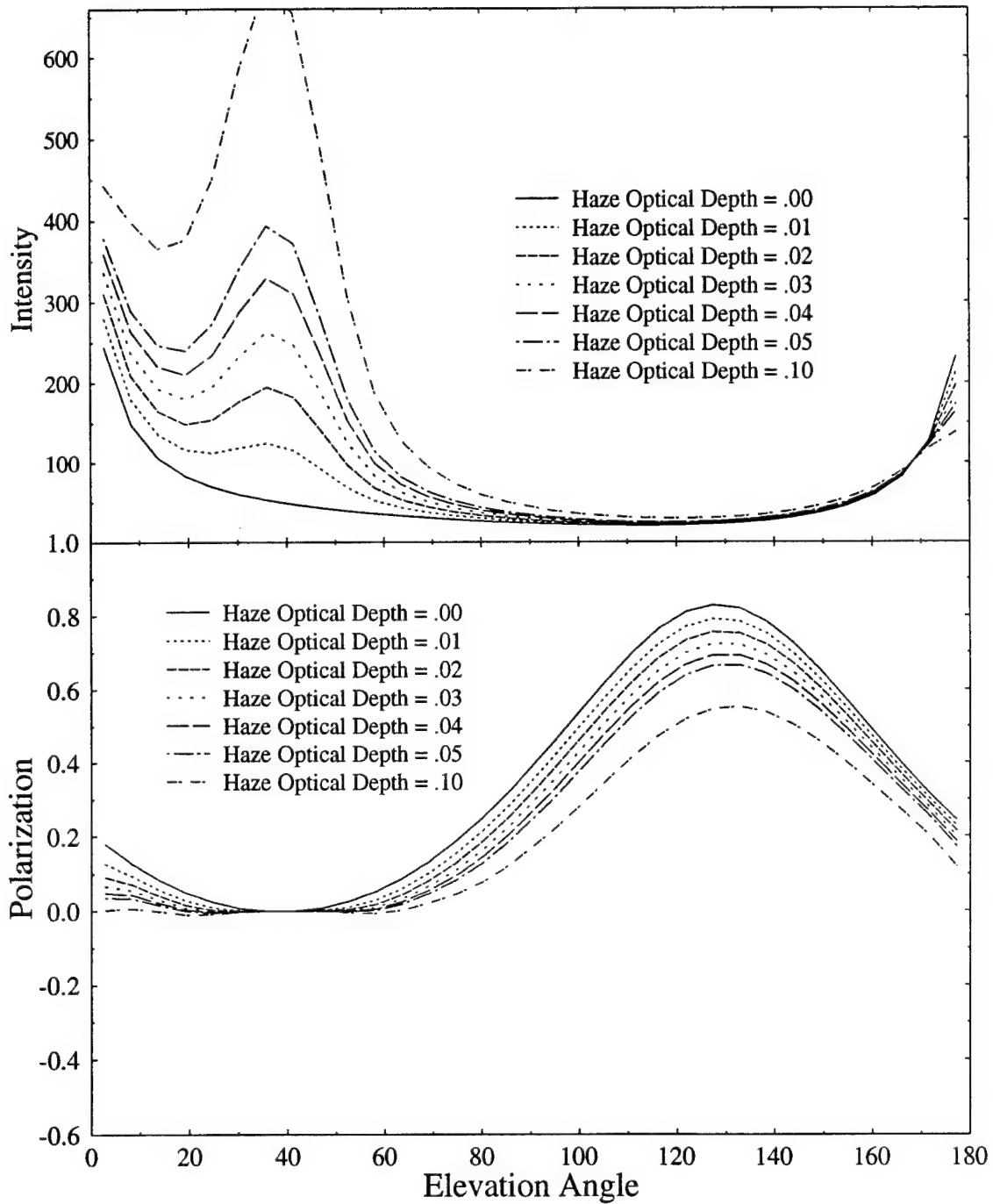
Figure 4.15: Effects of introducing haze into the atmosphere. The Rayleigh portion of optical depth is held constant at .10 while the optical depth of haze increased from .01 to .10. Solar zenith angle is 50° and surface albedo is zero.
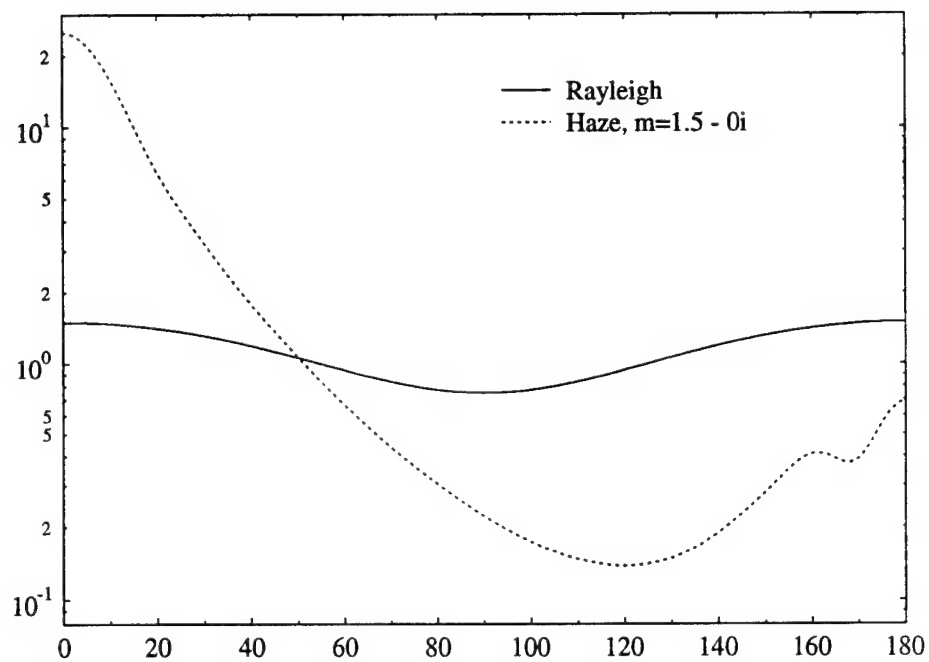
Figure 4.16: Scattering phase function for Rayleigh scattering and haze particles.

Chapter 5

SKY POLARIZATION EXPERIMENT

In this experiment, the sky radiation intensity is measured with the SSP. Using the calibration coefficients described earlier, the intensity values are used to calculate sky polarization. The resultant polarization patterns are compared to the modeled values.

5.1 Measuring the Solar Radiation

The SSP was mounted in the CSU Smart Solar Tracker as shown in Figure 5.1. The
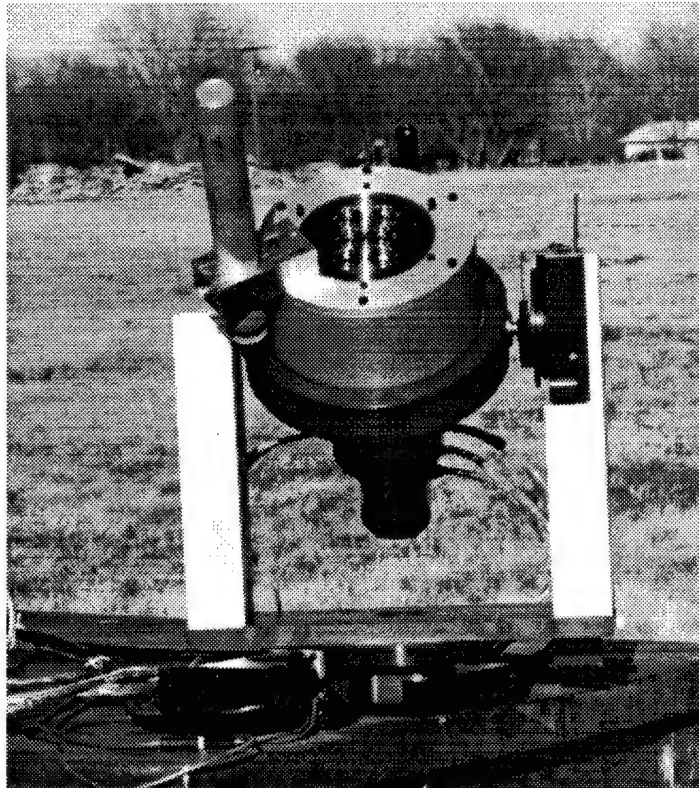
Figure 5.1: CSU Smart Solar Tracker.

solar tracker is a servo-driven two-axis mount that is controlled by a PC based motor controller card. The position of the servo motors is determined using optical encoders, which have a resolution of 600 steps/degree of rotation. Solar position is calculated using the positioning algorithm from "Astronomical Algorithms" (Meeus, 1991). Two modes of the tracking software were used. In the first mode the tracker centers itself on the sun and continually adjusts its position to follow the sun's movement. The second mode allows the user to stop the tracking routine and have the tracker move a given number of degrees from the solar position.

The procedure for this exercise included:

1. Set the SSP in the solar tracker. Align the SSP center line in the vertical. Cover the SSP lenses and center the solar tracker on the sun.

2. Once the solar tracker has located the sun, stop the tracking software. Use the controller to manually move the solar tracker a given number of degrees from the solar position. These moves are always made in the elevation of the tracker. Uncover the SSP lenses and record the sky radiation intensity.

3. Cover the lenses and have the tracking software re-acquire the sun.

4. Repeat Steps 2 and 3.

Intensity measurements were always made in the vertical plane of the sun. This simplifies several tasks: the solar tracker only has to be adjusted in elevation, calculation of the scattering angle is trivial (it is simply the difference between the solar elevation and the elevation the solar tracker is pointed), polarization can be determined using the Rubenson formula, and both the maximum and minimum sky polarizations will be sampled during each scan.

Measurements were made at 5° intervals in elevation both above and below the solar position. At each position data were recorded for approximately 60 seconds. This provided more than 100 scans of data to be averaged together. Additional time was required to re-acquire the solar position before each reading. To scan the entire hemisphere required about 2 hours. Three scans were performed on 24 February, the first and third scans centered around $2\frac{1}{2}$ hours before and after solar noon with an average solar elevation of

30° and the second scan was centered around solar noon with the solar elevation of 40°. Data from the second scan will be used for illustration purposes.

During the same time the sky radiation was being measured, measurements of optical thickness were made with the University of Arizona, Custom Filter-Wheel Solar Radiometer. The radiometer uses ten narrow band filters from 370 nm through 1030 nm. Data from the radiometer are plotted on a langley diagram to determine the optical thickness. Table 5.1 lists the measured optical thickness for each of the radiometer channels.

Table 5.1: The University of Arizona, Custom Filter-Wheel Solar Radiometer central wavelengths and the measured optical depths.

Channel	Wavelength Center (nm)	Optical Thickness
1	370	.431
2	400	.317
3	441	.221
4	520	.133
5	610	.097
6	670	.057
7	779	.027
8	870	.018
9	939	.193
10	1029	.012

5.2 Solar Data

Figure 5.2 illustrates an interesting point about the calibration lamp. The plot shows the raw data signal received from the calibration source at a gain setting of 25.75. and the raw power received from the sky when the SSP is 10° from the solar position at the same gain setting. Note how the received power from the calibration lamp is much lower than the received power from the sky light at wavelengths shorter than 700 nm. Thus for the shorter wavelengths, error may be introduced into the calibration coefficients due to instrument noise, which is the spectral region where the atmospheric signal is the strongest. The only way to overcome this is to find a different type of calibration source that emits stronger at the shorter wavelengths.
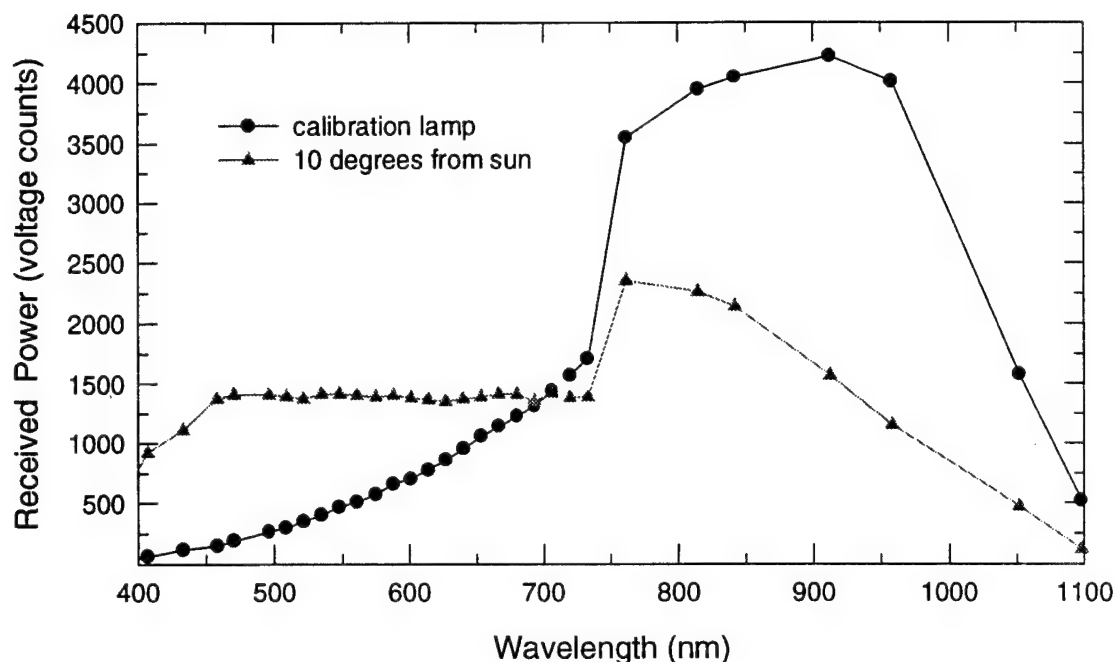
Figure 5.2: Raw data signals received by the SSP for the calibration lamp and from the the sky with the SSP 10° from the solar position. The gain setting for both measurements was 25.75. Note the low signal intensity from the calibration lamp at the shorter wavelengths.

Before we examine the data results from the solar scan, it is interesting to once again look at the raw data. Figure 3.15, shown earlier, was for a solar elevation only 10° from the solar position. Figure 5.3 illustrates the same data for the solar elevation 90° from the solar position. For this scan, the gain setting on channels 1 and 2 is 25.75 and the gain setting for channels 3 and 4 is 34.00. The higher gain setting for channels 2-4 introduces a significant amplification of the DC voltage offset, moving the data points down the graph. More importantly, the signal from the sky is so weak the spectral signal is difficult to see visually. Also, the broadband signal no longer saturates the detectors. This weak signal is the main reason 60 seconds (more than 100 scans) of data were gathered for each measurement.

Figure 5.4 shows the measured spectral radiance for an entire scan through the sun's vertical plane. This graph is plotted backward from the previous graphs, with longer wavelengths at the front. For this scan, the solar elevation was 40° (solar zenith angle of 50°). There is a increase in radiance at the shorter wavelengths, as is expected when

Diffuse and Radiance Channels

Polarization Channels
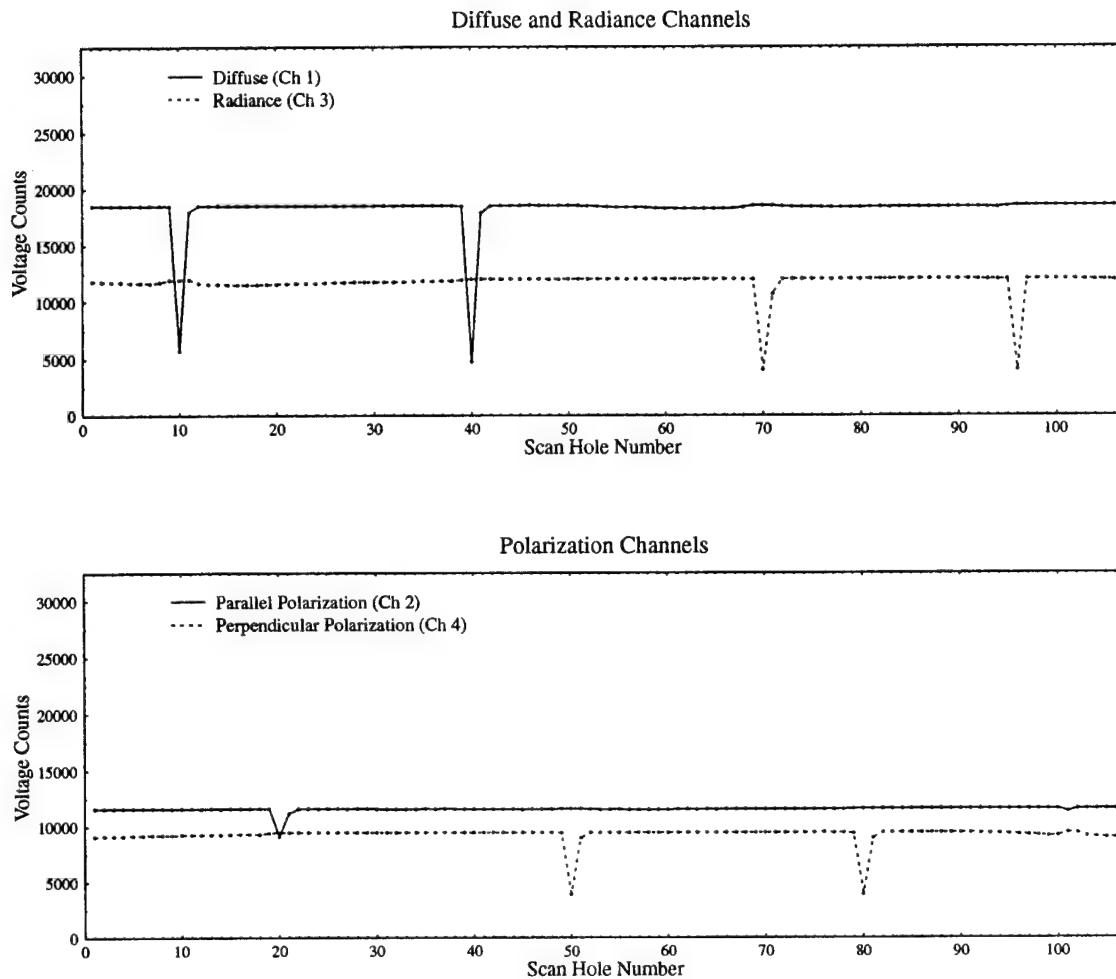
Figure 5.3: SSP raw data at 90° from solar position. Gain setting on channels 1 and 2 is 25.75. Gain setting for channels 3 and 4 is 34.00. The zero signal point is at the top of the graph.

measuring the solar spectrum. The SSP also detects the increase in radiance as it views closer to the horizon, especially near 165° elevation. Also note that at 5° elevation, the radiance falls off sharply, since the SSP was viewing a building. The elevations near the solar position are also interesting. Radiance increases at angles close to the sun. This is due to the forward scattering of haze. The haze contribution is in a very narrow band band around the solar position. There is even a trough of low radiance values at 15 - 20° elevation where the forward scattering of the haze has not overshadowed the normal Rayleigh radiation decrease for this area.
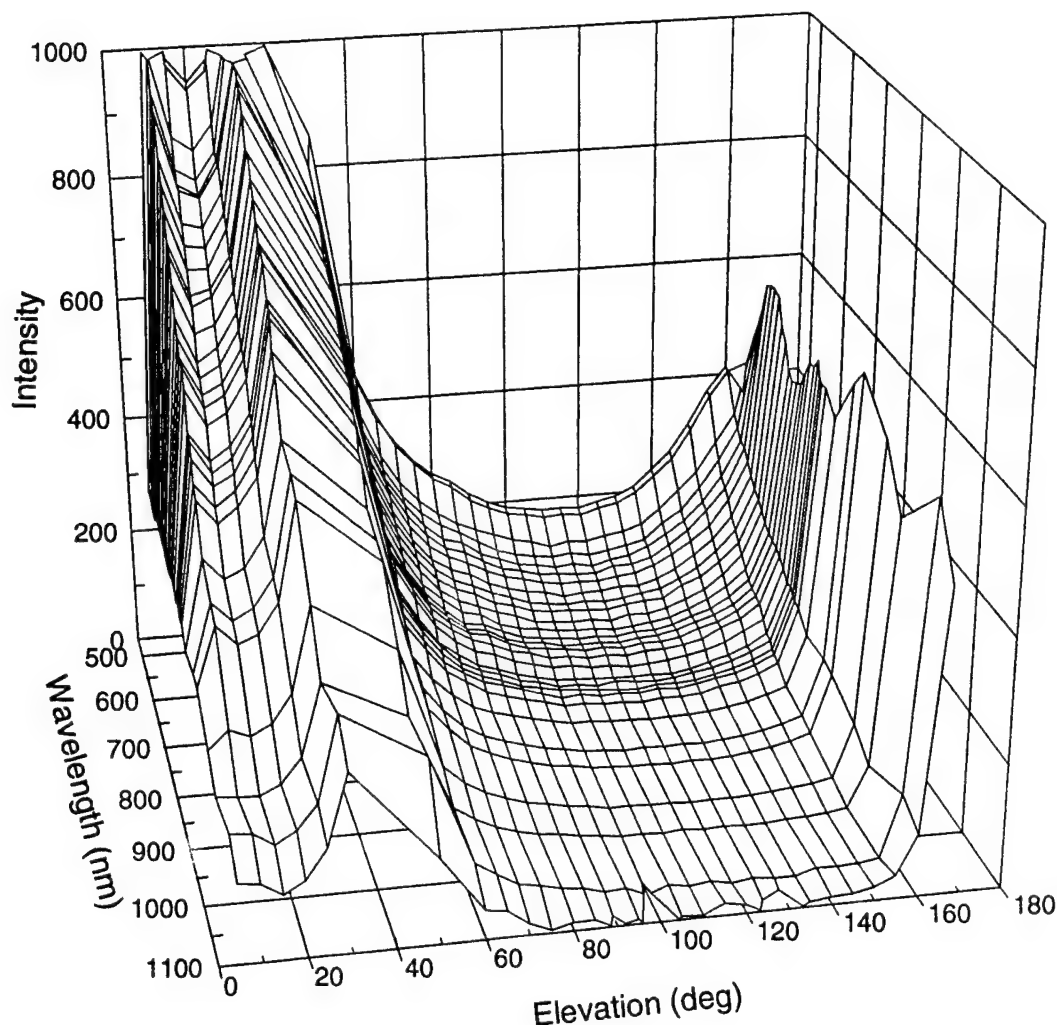
Figure 5.4: Spectral intensity versus wavelength and elevation angle for 24 February. The solar elevation was 40°.

Figure 5.5 shows the spectral intensity with its associated error at 60° and 130° elevation. Several interesting items are evident. The spectral intensity is much weaker at 130°. This effect is stronger as wavelength increases, since Rayleigh optical depth decreases with increasing wavelength. There is very little radiance in the NIR wavelengths at 130°. The radiance values calculated for CVF sections 1 and 2 in the region of overlap, between 660 nm and 740 nm, give almost identical results. This is an indication of the accuracy of the relative calibration. The oxygen absorption band at 760 nm is detected. The water vapor absorption band at 940 nm is detected by the 958 nm reading. This data shown here is from channel 3 for which 958 nm is the closest central wavelength, however, the
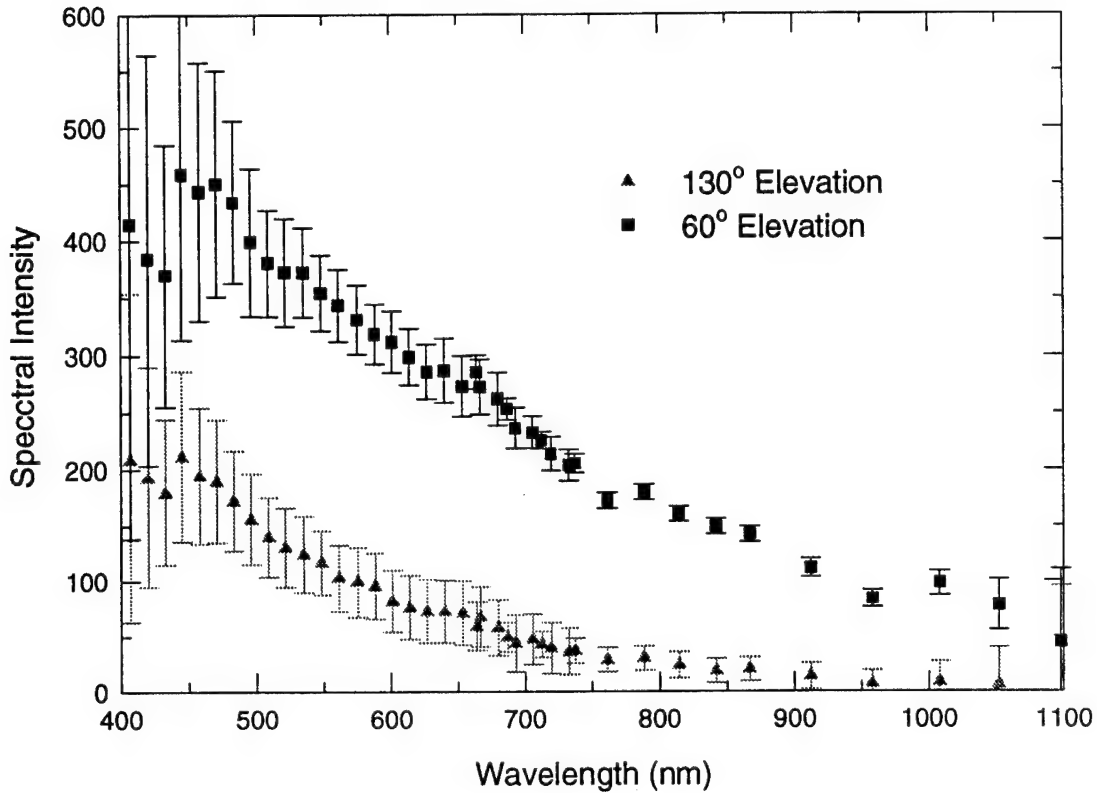
Figure 5.5: Spectral intensity at 60° and 130° elevation. The solar elevation was 40°. Note the radiance values calculated from the different filter wheels between 660 nm and 740 nm give almost identical results. Also, the oxygen absorption band at 760 nm and the water vapor absorption band at 940 nm are detected.

HBW is wide enough that information from the water vapor absorption band is measured. As discussed earlier, radiance errors are largest for the shorter wavelength due to the low emittance of the calibration lamp in this spectral region. In general, CVF section 2 has smaller errors since its transmission is higher. The errors for the NIR wavelengths of the 130° elevation scan are significantly larger than for the same wavelengths in the 60° elevation scan due to the low signal strength at 130°, thus allowing instrument noise to be a larger fraction of the measurement.

Figure 5.6 shows the spectral polarization for 24 February versus the elevation angle and wavelength. The polarization data are noisy, but the maximum polarization for all wavelengths stands out at approximately 130° elevation, which is 90° from the solar position. There is also a band of minimum, even slightly negative, polarization near
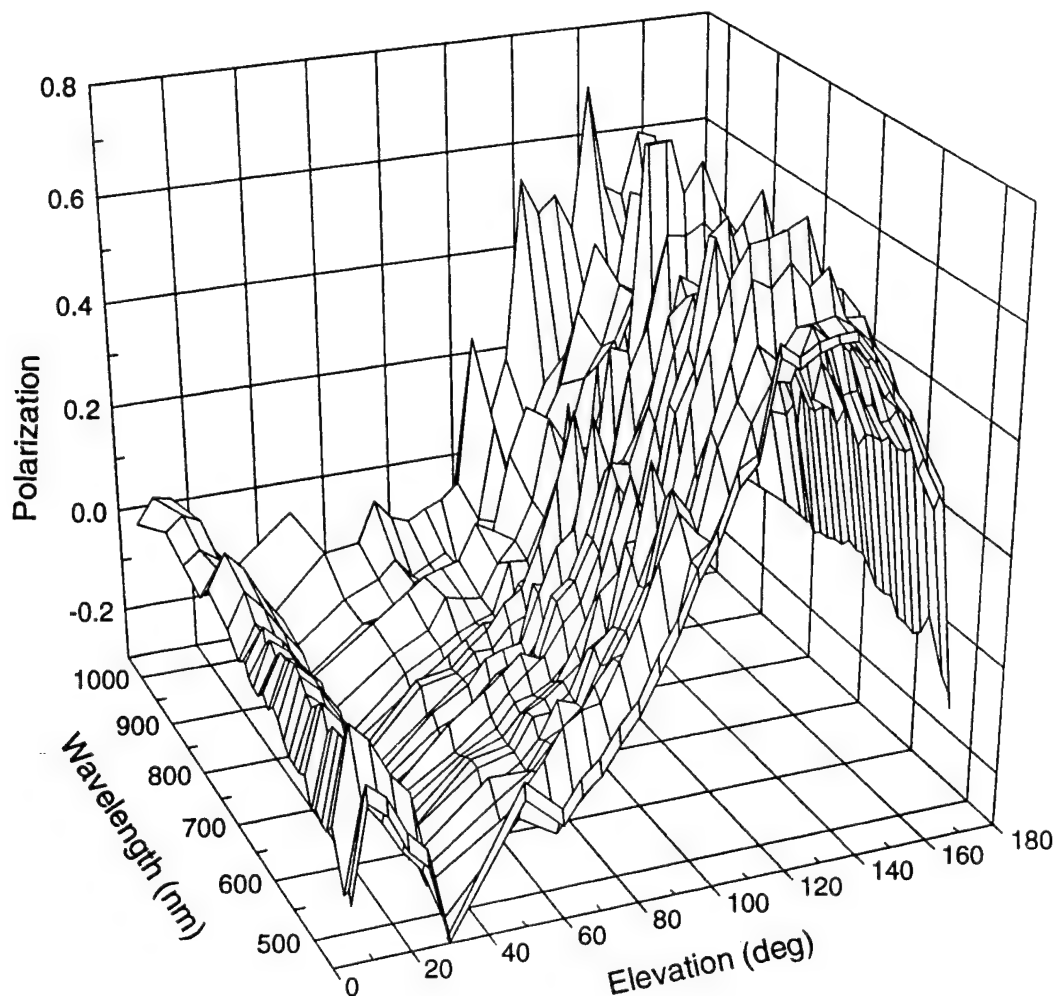
Figure 5.6: Spectral polarization versus wavelength and elevation angle. The solar elevation was 40°.

the solar position. The polarization at all angles shows very little dependance on the wavelength and therefore the optical depth.

Since all measurements are made in the plane of the sun's vertical, the polarization can be calculated with Rubenson's formula, or

$$P = \frac{I_r - I_l}{I_r + I_l}.$$

The error in calculating the polarization depends on two quantities, both I_r and I_l. Assuming the errors are independent of each other the final error is calculated by

$$\sigma_P = \sqrt{(\frac{\partial P}{\partial I_l})^2 \sigma_{I_l}^2 + (\frac{\partial P}{\partial I_r})^2 \sigma_{I_r}^2} \qquad (5.1)$$

which reduces to

$$\sigma_P = \frac{2}{(I_l + I_r)^2} \sqrt{I_l^2 \sigma_{I_r}^2 + I_r^2 \sigma_{I_l}^2} \tag{5.2}$$

Figure 5.7 shows the spectral polarization and its associated error at 60° and 130° elevation. The errors are substantial at all wavelengths. At the shorter wavelength instrument noise introduces errors into the calibration coefficients. At the longer wavelengths, the low sky light intensity due to less scattering allows instrument noise to again introduce error. The net result is the error for the polarization measurements is large for all wavelengths. This again is justification for the long dwell time for the sky intensity measurements. Also, since intensity measurements from both channels 2 and 4 are required to determine the polarization, only data points where the central wavelengths of these two channels are within 1% of each other is the polarization calculated. This eliminates some of the NIR data points shown in previous plots.

To evaluate the error, the distribution of individual radiance values at 130° elevation is shown in Figure 5.8 for all three NFOV channels. The range between the maximum and minimum radiance value for each channel was divided into 20 equal bins and the number of readings within each bin is plotted. The radiance distribution for each channel is close to a gaussian distribution. Skewness for a gaussian curve is zero. The skewness for channels 2 - 4 was .19, .14, and .1 respectively. This indicates the majority of the error is associated with instrument noise and the distribution average is a representative value. The data at 130° elevation has a signal to noise ration of 4:1 for the radiance and perpendicular polarization channels and as low as 1:1 for the parallel polarization channel.

5.3 Model Comparisons

To run the model, several parameters must be determined. These include the solar zenith angle, Rayleigh and haze optical depths, surface albedo, and solar spectral flux at the top of the atmosphere.

The solar zenith angle for the second scan was 50°. During the entire scan this only changed by less than $\frac{1}{2}°$. For scans one and three, the solar zenith angle varied from

56° through 68°. For these scans, an average solar zenith angle of 62 was used and each measurement elevation was corrected.

Paltridge and Platt (1976) developed the Rayleigh optical depth calculation

$$\tau_R(\lambda, h) = 0.0088\lambda^{(-4.15+0.2\lambda)}[exp(-0.1188h - 0.00116h^2)] \tag{5.3}$$

where h is in kilometers and λ is in microns. Once the Rayleigh optical depth is known, it is assumed that haze makes up the difference between the calculated and measured optical depths.

A representative surface albedo was determined from Rowe (1993) and the solar spectral flux was obtained from Iqbal (1983).

Figure 5.9 and Figure 5.10 compare the measured values of sky light radiance and polarization to the modeled values for 520 nm and 670 nm. The radiance values from the SSP measurements were scaled to the modeled values at 130° elevation. The plots illustrate the model in three stages of complexity: first with only Rayleigh scattering and no surface reflection, the second step adds in surface albedo, and the third stage has both Rayleigh and haze scattering with surface reflection. The intensity profile requires the addition of haze into the model before a realistic prediction is achieved. The polarization is reasonably predicted by the Rayleigh scattering case with surface albedo. The addition of haze improves the model prediction at all angles. Agreement between the model and measurements is generally good, except in the vicinity of the sun where values of negative polarization were observed. Only for optically thick Rayleigh atmospheres did the model produce negative polarization in this location. Since forward scattering of the modeled haze is unpolarized, adding haze to the atmosphere depolarized the negative polarization induced by Rayleigh scattering near the sun. Of note is the smaller error bar for 130° (90° above the solar position) when compared to the measurements for 125 and 135°. This was a direct result of the number of scans taken for the readings. The measurments at 125 and 135° had just over 100 scans of data and the 130° measurement had over 200 scans, thus reducing the uncertainty. Also, the maximum errors in the polarization occur close to the sun and the horizon. At both locations, sky light intensity changes rapidly with

viewing angle. The most probable cause for this error is SSP channels 2 and 4 looking in slighty different directions, i.e. the parallel channel (2) looking above the perpendicular channel (4).
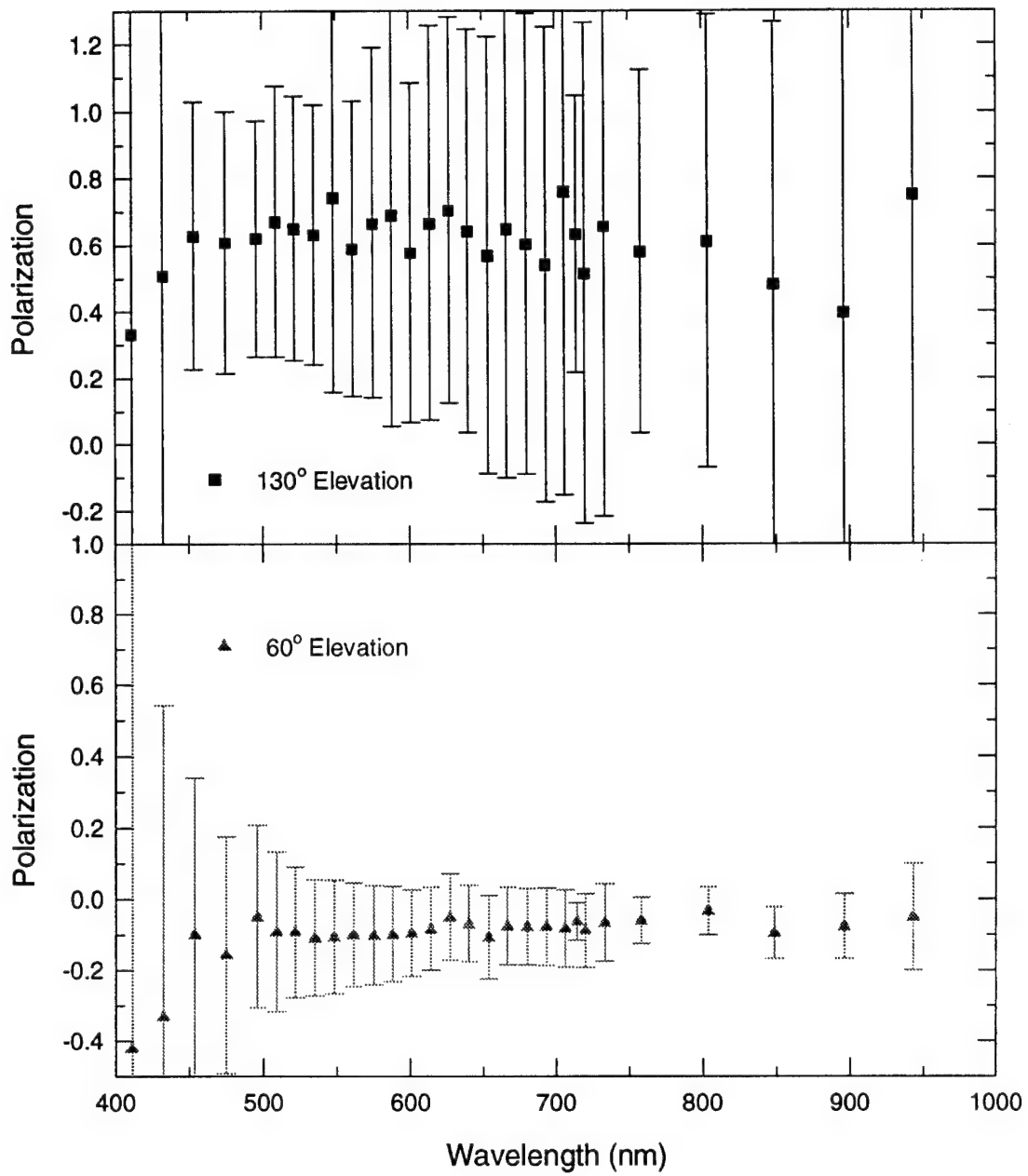
Figure 5.7: Spectral polarization at 60° and 130° elevation. The solar elevation is 40°.
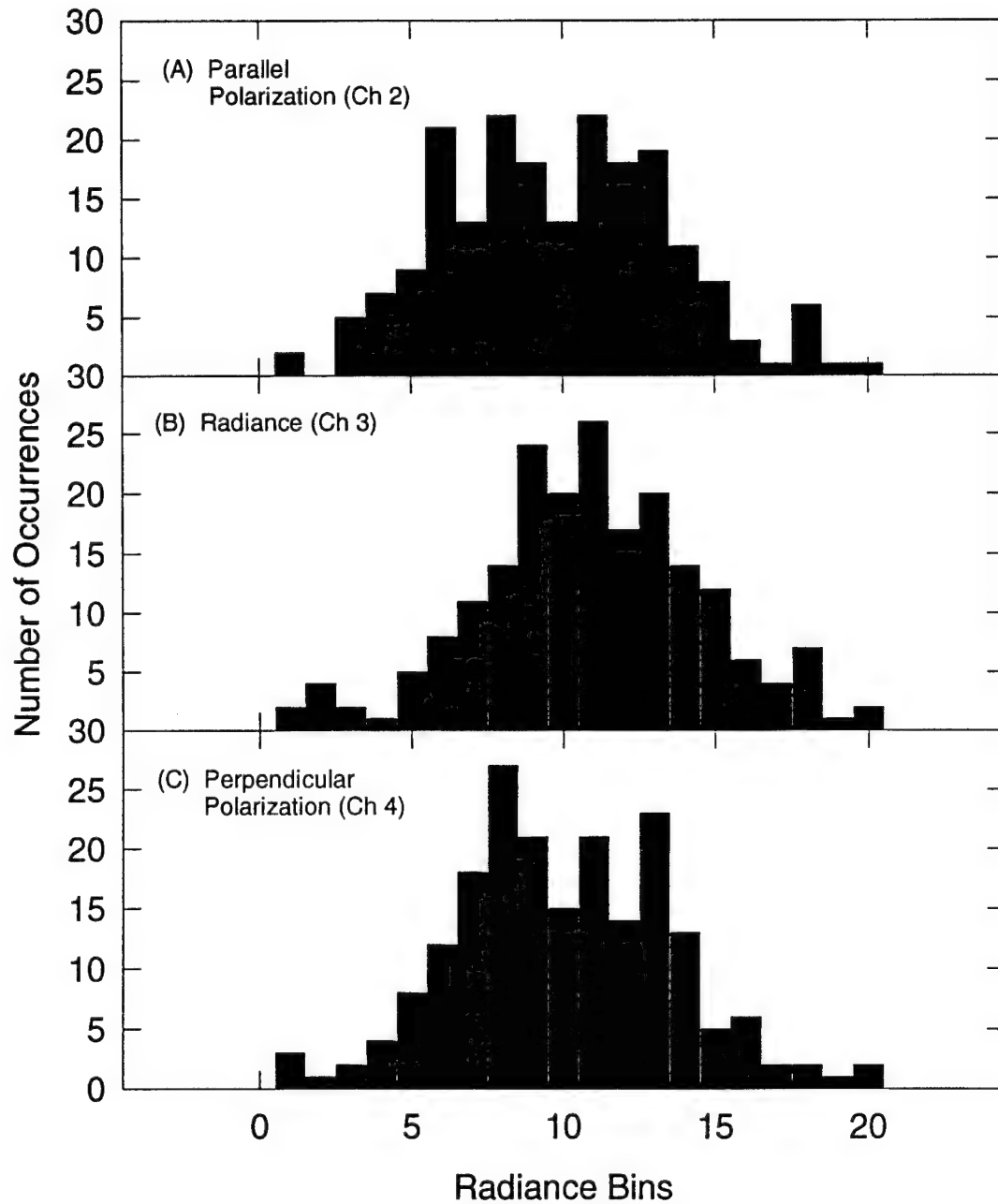
Figure 5.8: Radiance values error distribution for 130° elevation. Radiance values are grouped into 20 equal bins between the maximum and minimum readings for each channel.
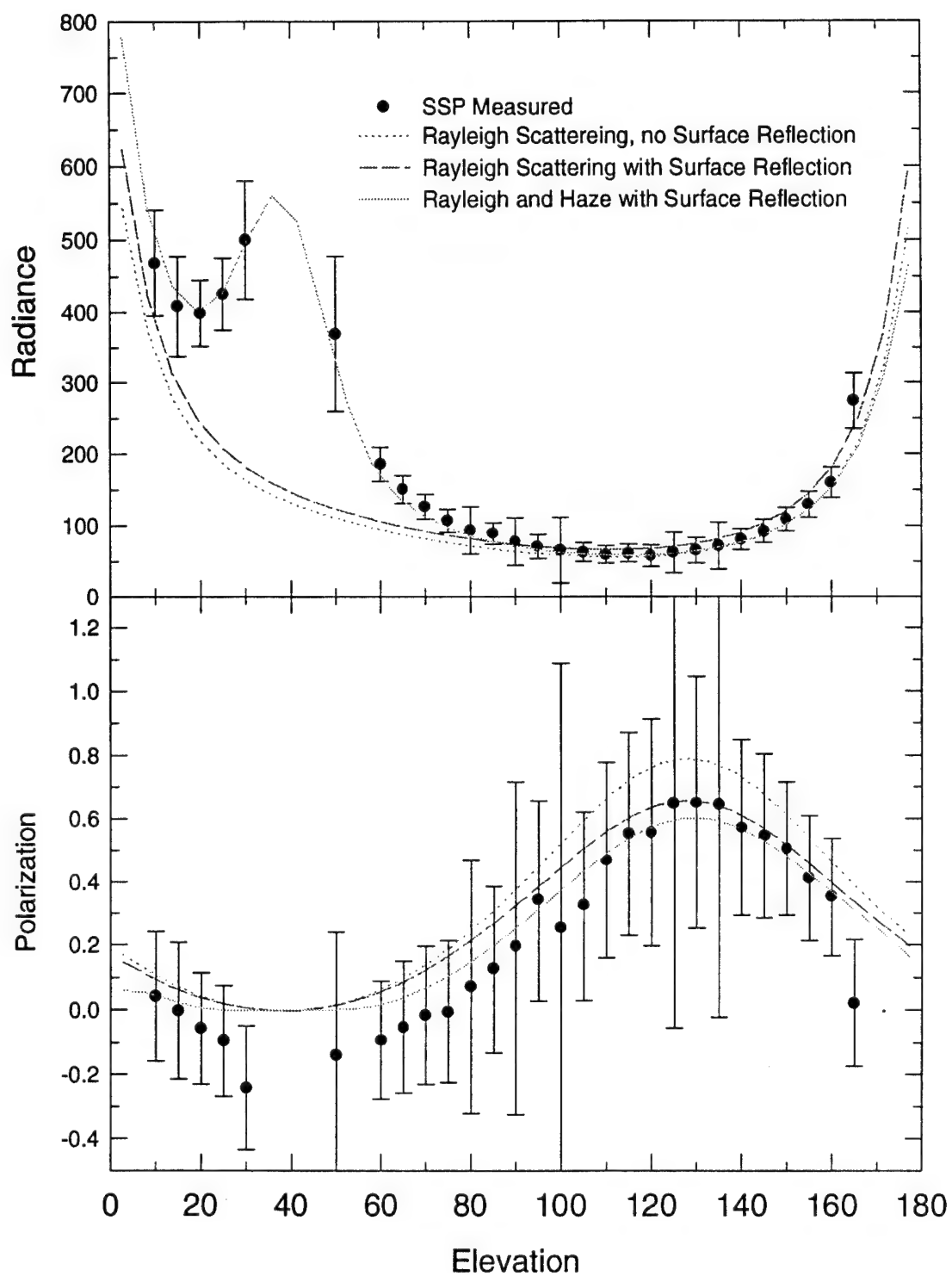
Figure 5.9: SSP measured intensity and polarization compared to the model predicted values for 521 nm.
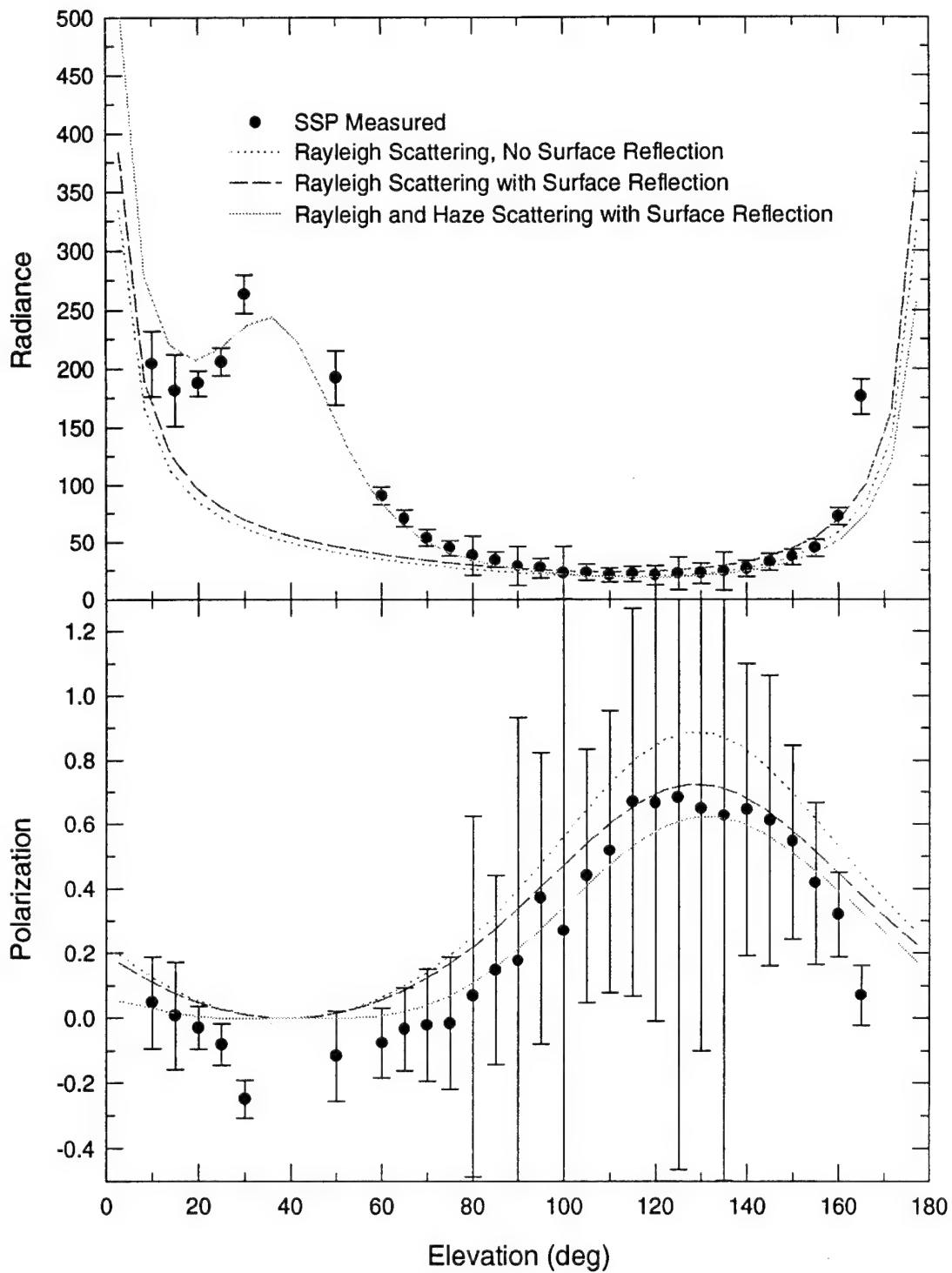
Figure 5.10: SSP measured intensity and polarization compared to the model predicted values for 670 nm.

Chapter 6

SUMMARY AND CONCLUSIONS

The SSP is in its third iteration, the current instrument description, optics characteristics, and data acquisition systems were presented. The new version has several improvements over the previous instruments:

1. Compact, small enough to fly in a unmanned aerospace vehicle (UAV).

2. Adds polarization capability. This version has the capability of 4 polarization channels; parallel, perpendicular, and right and left hand circular. Only the parallel and perpendicular optics were installed for this thesis work. Previous versions only had diffuse and radiance channels.

3. Increased spectral range. In the current configuration the SSP spectral range is only 400 - 1100 nm. When the new detectors are installed the range will be increased to 400 - 4000nm. The spectral range of version 1 was 400 - 1200nm and version 2 was 400 - 2500 nm

The SSP is ready to collect atmospheric data from airborne platforms at this time. The instrument has flown test missions in manned aircraft and in the General Atomics (GNAT) UAV. It is currently in compatibility testing for the Perseus-B UAV payload. The SSP will provide spectral measurements that are unique to the remote sensing of clouds, aerosols, and land surfaces.

Initial calibration was conducted here at Colorado State University. The calibration procedures, to include the optics installation and alignment, measuring the instruments field of view, and determining the angular response for the diffuse channel were outlined. To both confirm the accuracy of the calibration and as a study of the sky light radiance, the sky light intensity and polarization were measured with the SSP in an experiment for

this thesis. A polarized radiative transfer model was utilized to examine the effects local conditions can have on the sky light intensity and polarization and to evaluate the SSP data.

6.1 Summary of Results

6.1.1 Instrument

The optics of the Scanning Spectral Polarimeter were characterized in this paper.

1. Perpendicular and parallel polarization channels are aligned $90° \pm .183°$.

2. The viewing angle for the three narrow field of view channels was ~20 mRad for channels 2 and 3 and ~19 mRad for channel 4. These values are slightly lower than those predicted by ray tracing.

3. The angular response of the flashed opal diffuser was measured as a function of wavelength. A very strong forward transmission lobe was quantified in the NIR wavelengths. This lobe is not well documented by the manufacturer.

4. Calibration coefficients were determined and allow accurate relationships between spectral radiances measured with the different channels.

6.1.2 Model

The polarized radiative transfer model was used to isolate effects of changing Rayleigh optical depth, solar position, surface reflection, and haze loading. Single scatter Rayleigh conditions will produce an atmosphere with 0% polarization in the vicinity of the sun and 100% polarization 90° from the sun.

1. As Rayleigh optical depth increases, the polarization is decreased at all angles, and can even become negative. Optically thick Rayleigh atmospheres have a significant area of negative polarization near the sun.

2. Increasing surface albedo by 5% causes approximately a 5% decrease in the maximum polarization 90° from the sun. The effect near the sun is much smaller.

3. Increasing the solar elevation angle causes the maximum and minimum polarizations to shift across the sky and also a slight depolarization at all angles.

4. The addition of haze to the atmosphere induces strong depolarization at all levels. Haze layers of relatively small optical depth ($\tau_h < .1$) also causes the intensity of diffuse radiation to increase dramatically, especially near the sun.

6.1.3 Experiment

Polarization measurements made with the SSP were in generally good agreement with values predicted by the model. Rayleigh scattering alone captures the major elements of the sky polarization pattern. Adding surface reflection and haze layers to the model brings the results closer to that measured with the SSP. The average polarization error in the SSP data is less than 10% with respect to the model. Two areas of maximum disagreement were close to the sun, where the model predicted 0% polarization but the SSP measured negative polarization, and at the horizon. The maximum error for both cases is ∼20%.

6.2 Conclusions

1. The SSP provides detailed spectral polarization characteristics suitable for research in remote sensing of the earth's surface and the atmosphere, to include clouds and aerosols.

2. The SSP is capable of measuring the spectral sky polarization to within 10% accuracy, with respect to model predictions.

3. The instrument is capable of resolving the effects that aerosol scattering and surface reflection have on sky polarization. The non-spherical properties of atmospheric aerosols limit the degree of accuracy to which the model can predict sky polarization patterns.

4. Characterization of the flashed opal diffuser spectral transmission function will allow the SSP to determine spectral hemispheric flux within 5% accuracy.

6.3 Instrument Improvements

Several instrument improvements are currently being undertaken, including:

1. The NIR detectors are being replaced. This will allow measurements from 1100 nm through 4000 nm.

2. The optical encoder is being changed so measurements are recorded at even intervals around the CVF. This will allow all detectors to make measurement at identical wavelengths and simplify polarization calculations.

3. The detector electronics are being upgraded to remove the DC voltage offset prior to signal amplification. This will enable the data part of the signal to be amplified more, thus reducing the significance of instrument noise on errors.

Bibliography

Beiying, W. and D. Lu, 1988: Retrieval of stratospheric background aerosol scattering coefficient from twilight polarization measurements. *Appl. Optics*, **27**, 4899–4906.

Bellver, C., 1988: Luminance and polarization of the sky light at Seville (Spain) measured in the white light. *Atmos. Environ.*, **22**, 595–599.

Chandrasekhar, S., 1960: *Radiative Transfer*. Dover, 393 pp.

Chandrasekhar, S. and D. D. Ebert, 1954: The illumination and polarization of the sunlit sky on Rayleigh scattering. *Trans. Am. Philos. Soc.*, **44**, 643–728.

Coulson, K. L., 1977: Atmospheric turbidity determinations by skylight measurements at the Mauna Loa Observatory. *Contrib. Atmos. Sci.*, **13**.

Coulson, K. L., 1980: Characteristics of skylight at the zenith during twilight as indicators of atmospheric turbidity. 1: Degree of polarization. *Appl. Optics*, **19**, 3469–3480.

Coulson, K. L., 1981: Characteristics of skylight at the zenith during twilight as indicators of atmospheric turbidity. 2: Intensity and color ratio. *Appl. Optics*, **20**, 1516–1524.

Coulson, K. L., 1983: Effects of the El Chichon volcanic cloud in the stratosphere on the polarization on light from the sky. *Appl. Optics*, **22**, 1036–1050.

Coulson, K. L., 1988: *Polarization and Intensity of Light in the Atmosphere*. A. DEEPAK Publishing, 596 pp.

Coulson, K. L., J. V. Dave, and Z. Sekera, 1960: *Tables Related to Radiation Emerging from a Planetary Atmosphere with Rayleigh Scattering*. Univ. of California Press, 548 pp.

Dave, J. V., 1970: Intensity and polarization of the radiation emerging from a plane-parallel atmosphere containing monodispersed aerosols. *Appl. Optics*, **9**, 2673–2684.

Dave, J. V., 1978: Review paper: Extensive datasets of the diffuse radiation in realistic atmospheric models with aerosols and common absorbing gases. *Sol. Energy*, **21**, 361–369.

Deirmendjian, D., 1969: *Electromagnetic Scattering on Spherical Polydispersions*. American Elsevier Publishing Co., 290 pp.

Deschamps, P., F. Breon, M. Leroy, and A. Podaire, 1994: The POLDER mission: Instrument characteristics and scientific objectives. *IEEE Trans. Geosci. Remote Sens.*, **32**, 598–615.

Deuze, J. L., F. M. Breon, P. Y. Deschamps, and c. Devaux, 1993: Analysis of the POLDER (POLarization and Directionality of Earth's Reflectances) airborne instrument observations over land surfaces. *Remote Sens. Environ.*, **45**, 137–154.

Evans, K. F. and G. L. Stephens, 1991: A new polarized atmospheric radiative transfer model. *J. Quant. Spectosc. Radiat. Transfer*, **46**, 413–423.

Fitch, B. W. and K. L. Coulson, 1983: Effects of skylight at south pole station, Antarctica, by ice crystal precipitation in the atmosphere. *Appl. Optics*, **22**, 71–74.

Goloub, P., J. L. Dueze, M. Herman, and Y. Fouquart, 1994: Analysis of the POLDER polarization measurements performed over cloud covers. *IEEE Trans. Geosci. Remote Sens.*, **32**, 78–88.

Grant, I. P. and G. E. Hunt, 1969: Discrete space theory of radiative transfer. *Proc. Roy. Soc. London*, **A313**, 183–197.

Hitzfelder, S. J., G. N. Plass, and G. W. Kattawar, 1976: Radiation in the earth's atmosphere: Its radiance, polarization and ellipticity. *Appl. Optics*, **15**, 2489–2500.

Hovenier, J. W., 1969: Symmetry relationships for scattering of polarized light in a slab of randomly oriented particles. *J. Atmos. Sci.*, **26**, 488–499.

Iqbal, M., 1983: *An Introduction to Solar Radiation.* Academic Press.

Ishimaru, A., D. Lesselier, and C. Yeh, 1984: Multiple scattering calculations for non-spherical particles based on the vector radiative transfer theory. *Radio Sci.*, **19**, 1356–1366.

Kattawar, G. W., G. N. Pllas, and S. J. Hitzfelder, 1976: Multiple scattered radiation emerging from Rayleigh and continental haze layers. 1: Radiance, polarization, and neutral points. *Appl. Optics*, **15**, 633–647.

Meeus, J., 1991: *Astronomical Algorithms.* Willmann-Bell Inc, 429 pp.

Nakajima, T. and M. D. King, 1990: Determination of the optical thickness and effective particle radius of clouds from reflected solar radiation measurements. Part I: Theory. *J. Atmos. Sci.*, **47**, 1878–1893.

Paltridge, G. W. and C. M. R. Platt, 1976: *Radiative Processes in Meteorology and Climatology.* Elsevier Sci. Pub. Co., 318 pp.

Rowe, C. M., 1993: Global land-surface albedo modeling. *Int. J. Climat.*, **13**, 473–495.

Scott, J. C. and G. L. Stephens, 1985: A visible-infrared spectroradiometer for cloud reflectance measurements. *J. Phys. E: Sci. Instrum.*, **18**, 697–701.

Stackhouse, P. W. and G. L. Stephens, 1991: A theoretical and observational study of the radiative properties of cirrus: Results from FIRE 1986. *J. Atmos. Sci.*, **48**, 2044–2059.

Stackhouse, P. W., G. L. Stephens, A. J. Heymsfield, and T. Uttal, 1994: Investigation of the effects of the macrophysical and microphysical properties of cirrus clouds on the retrieval of optical properties. *J. Atmos. Sci.* Submitted.

Stephens, G. L. and J. C. Scott, 1985: A high speed spectrally scanning radiometer (SPERAD) for airborne measurements of cloud optical properties. *J. Atmos. Ocean. Tech.*, **2**, 148–156.

Takano, Y. and K. Liou, 1989: Solar radiative transfer in cirrus clouds. Part I: Single-scattering and optical properties of hexagonal ice crystals. *J. Atmos. Sci.*, **46**, 3–22.

Tsay, S., P. M. Gabriel, M. D. King, and G. L. Stephens, 1994: A fourier-riccati approach to radiative transfer. Part II: applications to spectral reflectance and heating/cooling rates in the 5 December 1991 FIRE IFO cirrus case study. *J. Atmos. Sci.* Submitted.

Wiscombe, W. J., 1976: On initialization, error and flux conservation in doubling method. *J. Quant. Spectosc. Radiat. Transfer*, **16**, 477–489.

Appendix A

CVF CENTRAL WAVELENGTHS

Table A.1: Listing of the central wavelength for each reading made by the SSP as a function of both index hole number and degrees of rotation of the CVF wheel.

Detector Angle		300	240	120	60	180	0
Hole	Angle	Det 1	Det 2	Det 3	Det 4	Det 5	Det 6
1	3	2727.4	1831.67	842	509	1355	4026.07
2	6	2662.47	1795	814.5	521.5	1330	3961.13
3	9	2597.53	1758.33	788.5	535	1305	3896.2
4	12	2532.6	1721.67	761.5	548	1280	3831.27
5	15	2467.67	1685	737.5	561	1255	3766.33
6	18	2402.73	1648.33	712.5	575	1230	3701.4
7	21	2337.8	1611.67	687	588	1204	3636.47
8	24	2272.87	1575	664	601	1179	3571.53
9	27	2207.93	1538.33	639	614	1154	3506.6
10	30	clear	1501.67	clear	627	1129	3441.67
11	33	2198.33	1465	381	640	1104	3376.73
12	36	2161.67	1428.33	394	653.5	1077	3311.8
13	39	2125	1391.67	407	666.5	1050	3246.87
14	42	2088.33	1355	420	680	1025	3181.93
15	45	2051.67	1318.33	433	693	996	3117
16	48	2015	1281.67	445	706	970	3052.07
17	51	1978.33	1245	458	719.5	945	2987.13
18	54	1941.67	1208.33	470.5	733	919	2922.2
19	57	1905	1171.67	483	742	892	2857.27
20	60	1868.33	clear	496	clear	867	2792.33
21	63	1831.67	1355	509	4026.07	842	2727.4
22	66	1795	1330	521.5	3961.13	814.5	2662.47
23	69	1758.33	1305	535	3896.2	788.5	2597.53
24	72	1721.67	1280	548	3831.27	761.5	2532.6
25	75	1685	1255	561	3766.33	737.5	2467.67
26	78	1648.33	1230	575	3701.4	712.5	2402.73
27	81	1611.67	1204	588	3636.47	687	2337.8
28	84	1575	1179	601	3571.53	664	2272.87

Table A.1 (cont)

Detector Angle		300	240	120	60	180	0
Hole	Angle	Det 1	Det 2	Det 3	Det 4	Det 5	Det 6
29	87	1538.33	1154	614	3506.6	639	2207.93
30	90	1501.67	1129	627	3441.67	clear	clear
31	93	1465	1104	640	3376.73	381	2201.67
32	96	1428.33	1077	653.5	3311.8	394	2168.33
33	99	1391.67	1050	666.5	3246.87	407	2135
34	102	1355	1025	680	3181.93	420	2101.67
35	105	1318.33	996	693	3117	433	2068.33
36	108	1281.67	970	706	3052.07	445	2035
37	111	1245	945	719.5	2987.13	458	2001.67
38	114	1208.33	919	733	2922.2	470.5	1968.33
39	117	1171.67	892	742	2857.27	483	1935
40	120	clear	867	clear	2792.33	496	1901.67
41	123	1355	842	4026.07	2727.4	509	1868.33
42	126	1330	814.5	3961.13	2662.47	521.5	1835
43	129	1305	788.5	3896.2	2597.53	535	1801.67
44	132	1280	761.5	3831.27	2532.6	548	1768.33
45	135	1255	737.5	3766.33	2467.67	561	1735
46	138	1230	712.5	3701.4	2402.73	575	1701.67
47	141	1204	687	3636.47	2337.8	588	1668.33
48	144	1179	664	3571.53	2272.87	601	1635
49	147	1154	639	3506.6	2207.93	614	1601.67
50	150	1129	clear	3441.67	clear	627	1568.33
51	153	1104	381	3376.73	2198.33	640	1535
52	156	1077	394	3311.8	2161.67	653.5	1501.67
53	159	1041	407	3246.87	2125	666.5	1468.33
54	162	1019	420	3181.93	2088.33	680	1435
55	165	993	433	3117	2051.67	693	1401.67
56	168	971	445	3052.07	2015	706	1368.33
57	171	944	458	2987.13	1978.33	719.5	1335
58	174	918	470.5	2922.2	1941.67	733	1301.67
59	177	892	483	2857.27	1905	742	1268.33
60	180	867	496	2792.33	1868.33	clear	clear
61	183	842	509	2727.4	1831.67	4026.07	1355
62	186	814.5	521.5	2662.47	1795	3961.13	1330
63	189	788.5	535	2597.53	1758.33	3896.2	1305
64	192	761.5	548	2532.6	1721.67	3831.27	1280
65	195	737.5	561	2467.67	1685	3766.33	1255
66	198	712.5	575	2402.73	1648.33	3701.4	1230
67	201	687	588	2337.8	1611.67	3636.47	1204
68	204	664	601	2272.87	1575	3571.53	1179

Table A.1 (cont)

Detector Angle		300	240	120	60	180	0
Hole	Angle	Det 1	Det 2	Det 3	Det 4	Det 5	Det 6
69	207	639	614	2207.93	1538.33	3506.6	1154
70	210	clear	627	clear	1501.67	3441.67	1129
71	213	381	640	2198.33	1465	3376.73	1104
72	216	394	653.5	2161.67	1428.33	3311.8	1077
73	219	407	666.5	2125	1391.67	3246.87	1050
74	222	420	680	2088.33	1355	3181.93	1025
75	225	433	693	2051.67	1318.33	3117	996
76	228	445	706	2015	1281.67	3052.07	970
77	231	458	719.5	1978.33	1245	2987.13	945
78	234	470.5	733	1941.67	1208.33	2922.2	919
79	237	483	742	1905	1171.67	2857.27	892
80	240	496	clear	1868.33	clear	2792.33	867
81	243	509	4026.07	1831.67	1355	2727.4	842
82	246	521.5	3961.13	1795	1330	2662.47	814.5
83	249	535	3896.2	1758.33	1305	2597.53	788.5
84	252	548	3831.27	1721.67	1280	2532.6	761.5
85	255	561	3766.33	1685	1255	2467.67	737.5
86	258	575	3701.4	1648.33	1230	2402.73	712.5
87	261	588	3636.47	1611.67	1205	2337.8	687
88	264	601	3571.53	1575	1180	2272.87	664
89	267	614	3506.6	1538.33	1154	2207.93	639
90	270	627	3441.67	1501.67	1128	clear	clear
91	275.3	650	3326.95	1436.89	1082	2170.22	395.38
92	280.6	673	3212.24	1372.11	1037	2105.44	417.76
93	285.9	696	3097.52	1307.33	986	2040.67	440.13
94	291.2	718	2982.8	1242.56	943	1975.89	462.51
95	296.5	740	2868.09	1177.78	896	1911.11	484.89
96	301.8	clear	2753.37	clear	848.5	1846.33	507.27
97	307.1	3937.32	2638.66	1320	803.5	1781.56	529.64
98	312.4	3822.61	2523.94	1275	758	1716.78	552.02
99	317.7	3707.89	2409.23	1230	714	1652	574.40
100	323	3593.18	2294.51	1182	670	1587.22	596.78
101	328.3	3478.46	clear	1143	clear	1522.44	619.16
102	333.6	3363.75	2191	1098	390	1457.67	641.53
103	338.9	3249.03	2126.22	1052	411	1392.89	663.91
104	344.2	3134.32	2061.44	1008	432.5	1328.11	686.29
105	349.5	3019.6	1996.67	958	453.5	1263.33	708.67
106	354.8	2904.88	1931.89	912	475	1198.56	731.04
107	360	2792.33	1868.33	867	496	clear	clear

Appendix B

PROCEDURES FOR CALIBRATION EXERCISES

B.1 Optics Alignment

The Glan-Taylor polarization cube in the perpendicular channel must be aligned 90°
from the Glan-Taylor in the parallel channel. Equipment layout for aligning the optics is
illustrated in Figure 3.1. Optical channels 2 and 4 are used for the polarization channels
since they are physically 180° apart from each other in the optics tower.

B.1.1 Alignment Procedure

1. Remove the optical tower from the SSP vacuum chamber and mount on the jig
with channel 2 located in the top right position.

2. Remove both the focusing lens (from optics layer 3) and Glan-Taylor polarizing
cubes (from optics layer 1) if they are installed for optical channels 2 and 4.

3. Put a centering guide in the back (layer 3) of the optics tower. Align the laser
beam on the center of the guide.

4. Put a centering guide in the front (layer 1) of the optics tower. The laser beam
should hit this new guide in its center. If the laser beam does not hit the second guide
in its center, the optics tower/laser beam are not aligned with each other. Adjust the
position of the optics tower for large corrections. Make small corrections with the two
mirrors. Use mirror 1 to adjust the originating position of the laser beam on mirror 2
and mirror 2 to adjust the beam direction. Repeat steps 3 and 4 until the laser beam is
centered on both the back and front guides.

5. After the beam is aligned on both centering guides, install the iris. Close the
aperture on the iris so the opening is slightly larger than the laser beam. Verify alignment
of the optical tower by installing the Glan-Taylor polarizing cube. The Glan-Taylor will

reflect some of the incident light. Look on the back of the iris to see the direction of the reflected beam. The reflected beam should be aligned with the incident beam. Small imperfections in the optics tower or lens construction will cause this alignment to be slightly off. This error was measured to be 0.28° between the incident and reflected beam for channel 2, and approximately half this value for channel 4. Once the laser beam is aligned with the optical tower, do not adjust the laser beam or the optical tower jig. The following adjustments will be accomplished by moving the detector or lens holders.

6. Remove the Glan-Taylor and the centering guides from the optics tower. Set up the detector, centering it on the laser beam. Also ensure the light reflected by the detector is aligned with the incident beam. Maximum signal from the detector well be obtained when the detector is properly centered and aligned.

7. Put a lens centering guide in lens holder 2. Center the guide in the laser beam. Once the lens is centered it can be aligned by putting a piece of paper behind the guide. If aligned properly, a circle of light will be transmitted. If the guide is out of alignment it will create an interference pattern. To align the guide, remove the interference. This will yield only a crude alignment. Remove the centering guide and install the Glan-Taylor. Fine tune the alignment, by adjusting the reflected beam so it is coincident with the incident beam. Remove the Glan-Taylor and install the centering guide to verify the lens holder is still centered on the laser beam. Repeat the process until the lens holder is both centered and aligned.

8. Repeat step 7 for lens holder 1.

Once all the equipment is aligned with the laser beam, Glan-Taylor polarization cubes are ready for installation into the SSP optical tower. There are several methods to align the Glan-Taylors. These methods normally include setting a Glan-Taylor at a reference angle, shooting the laser beam through this reference cube and then through the Glan-Taylor being aligned. Either the maximum signal (the two cubes at the same angle) or the minimum signal (the two cubes 90° apart) are sought. For the equipment setup used it was very difficult to determine the maximum signal since the detector became saturated and readings near the maximum were very unstable. In an attempt to overcome this

problem, a filter was used to attenuate the signal, but readings from the detector were not reliable. To get a discernible change in the signal, the polarization cube had to be rotated 3-5°. On the other hand, detecting the minimum signal was very accurate. The base-line signal from the detector with no light hitting the detector was 0.48mV. The detector was sensitive to any incoming light. During this phase of the calibration all external light was eliminated. The lights were off, windows were covered, and the doors were shut with the hole at the bottom covered. The sensitivity at this range was measured at more than 100mV per degree of rotation. The following alignment procedure utilizes this extreme sensitivity at determining the minimum signal when the two Glan-Taylors are at 90° to each other.

9. Insert a Glan-Taylor into lens holder 1. This is the reference cube. This cube must be set square with the light table. It was aligned to allow radiation perpendicular to the light table to pass.

10. Insert a Glan-Taylor into channel 2 of the optics tower. Rotate the Glan-Taylor until the minimum signal is obtained. Lock the Glan-Taylor into position. This is difficult, as even a slight rotation of the Glan-Taylor caused by any vibration or uneven tightening of the lens clamp will change the lens orientation and thus cause the transmitted signal to vary. Once the minimum signal is obtained, the Glan-Taylor in the optics tower will be aligned 90° from the reference cube. Channel 2 will now eliminate all perpendicular radiation and therefore detect parallel polarization. The minimum reading achieved was 3.16mV.

11. Rotate the optics tower 180°. This will move channel 4 into the laser beam path. Verify alignment of the optics tower and laser beam by placing the centering guides and Glan-Taylors into optical channel 4. No adjustments should be required. If the optics tower/laser beam are not aligned after the rotation, the optics jig has most likely moved and the entire process must be repeated.

12. Remove the centering guides and Glan-Taylor from optical channel 4. Insert a Glan-Taylor into lens holder 2. Rotate this Glan-Taylor until the minimum transmitted signal is obtained. It is easier to adjust this lens since the lens holder makes it simpler

to lock the lens into position. Once the minimum signal is obtained, the Glan-Taylor in lens holder 2 will be aligned 90° from the reference Glan-Taylor in lens holder 1 and thus will allow radiation parallel to the light table to pass. The minimum signal obtained was 0.70mV. The Glan-Taylor in lens holder 2 now becomes the reference polarization cube.

13. Remove the Glan-Taylor from lens holder 1 and install it in the optics tower, layer 1 of channel 4. Repeat the alignment procedure of step 10. The Glan-Taylor in channel 4 will now be aligned 90° from the one in channel 2. Channel 4 will detect perpendicular polarization. The minimum signal obtained was 2.07mV.

B.1.2 Errors in alignment

To calculate the error in aligning the two Glan-Taylors, the voltages from the three settings were added together and three times the base-line voltage was then subtracted. This represents the maximum error since it assumes all errors in setting the lenses were in the same direction. This error is 4.49mV. Using the sensitivity of 100mV per degree, measured earlier, the error is .045°. Also, while re-positioning the optical tower, it was noted the jig allowed the optical tower to rotate slightly. This movement was measured to be 0.138°. This error is then added to the error calculated above providing the final positioning of the two Glan-Taylors as 90° ± .183°. This is a conservative estimate, since all errors are assumed to be in the same direction and as the optics tower is tightened to the jig, movement of the optics tower is reduced.

B.2 Field of View

The purpose of this exercise is to determine the field of view (FOV) for the three narrow field of view (NFOV) channels (channels 2 - 4). A plan view of the equipment setup used for this exercise is shown in Figure 3.3 and the side view is shown in Figure B.1. The SSP is set on a leveling bench and the light source and laser sit on scissors jacks. The light source is on a rolling bench. This exercise is conducted in a long hallway.

B.2.1 FOV Measurement Procedure

1. Center the table in the hallway. Level the table and then the leveling bench.
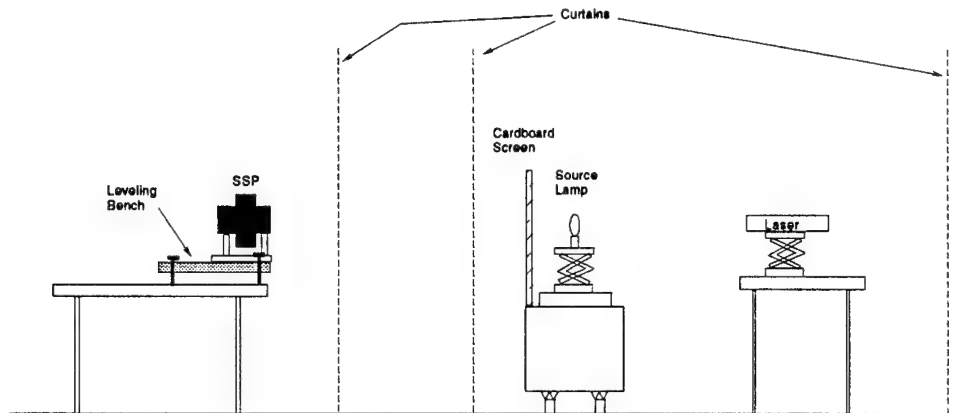
Figure B.1: FOV measurement layout.

2. Set laser and SSP on the leveling bench, SSP in the back and laser in the front. Align the SSP center line in the vertical. Adjust the height of the laser to the height of the entrance window for channel 2.

3. Shoot the laser down the center of the hallway towards the light source. Position the light source in the center of the hallway and adjust the height of the light source so the laser beam hits it in the center of the element.

4. Move the SSP into position on the leveling bench. Move the laser to the light source end of the hallway, behind the light source.

5. Position the laser in its new position so it is in on the experiment center line, shooting down the center of the hallway towards the SSP. Adjust the height of the laser to the height of the center of the light source element. Temporarily lower the light source.

6. Align the laser so the laser beam hits the SSP channel 2 entrance window.

7. Align the SSP on the leveling table so the laser beam is reflected back along its incident path. Lock the SSP into position on the leveling bench.

8. Adjust the light source, height and position, so the laser hits the center of the element. The line from the SSP to the light source now defines the experiment center line.

9. Mark the position of the light source bench. Tape a yard stick or tape measure to the floor perpendicular to the experiment centerline. This will be used to determine the distance the light source is from the centerline.

10. Measure the distance between the SSP and light source, this distance was 20 feet for our setup. At 20 feet we received ample signal to conduct the experiment, yet not saturate the detector and there was enough room in the hallway to move the light source out of the field of view of the SSP.

11. Attach a cardboard screen to the front of the light source bench. This screen moves with the light source and will stop most the reflections from the walls. Cut a small hole for the light to pass through and reach the SSP. Use the laser to find the center of the hole. The hole must be large enough for light from the source to illuminate the SSP when the source is moved to the side of the hallway.

12. To reduce reflections further, hang black felt curtains across the hallway. Cut a hole in the curtains to allow light from the source to reach the SSP.

13. Hang a black felt curtain behind the laser to reduce the reflections from the back wall.

14. Turn off the laser.

15. The light source is now moved along the perpendicular to the experiment center line. Light intensity received at the SSP is measured as the distance from the center line in varied.

16. Repeat for each narrow field of view channel.

B.3 Cosine Response of Diffuser

The object of this exercise is to measure how the transmission of the diffuser lens on channel 1 varies as the angle of incident light changes. Setup is similar to that for the narrow field of view measurement, however, the distance between the SSP and the light source is only 53.3 cm. A plan view of the experiment setup is shown in Figure 3.10. The side view is very similar to that shown for the FOV exercise in Figure B.1, except the distances are shorter and the curtains are positioned differently to reduce reflections.

B.3.1 Diffuser Transmission Function Measurement Procedure

1. Level table and leveling bench. Align the SSP centerline in the vertical.

2. Set the laser on the leveling bench at the height of the diffuser (channel 1) entrance lens. Shoot the laser towards the source light. Adjust the height of the light so the laser beam hits the center of the filament.

3. Set the SSP on the leveling bench with the instrument center line in the vertical. Draw a vertical line from the center of the diffuser lens to the base of the SSP stand. This line will help keep the SSP in the proper position as it is rotated. Align the SSP square with the leveling bench. Draw a line across the leveling bench, parallel with the SSP stand. Set the front of the SSP stand on this new line. Mark the point on the leveling bench directly below the center of the diffuser lens. The angle of SSP rotation will be measured with respect to the leveling bench, so this must be as exact as possible.

4. Move the laser behind the light source. Adjust and level the laser beam to the height of the center of the light filament. Temporarily lower the source light.

5. Shoot the laser towards the SSP hitting the diffuser lens for channel 1. Adjust the laser so the reflected beam lines up with the incident beam. Do not move the SSP for this adjustment.

6. Move the light source into the path of the laser and adjust the height so the laser is centered on the filament.

7. Set black felt curtains to reduce reflection from the walls.

8. The SSP head is rotated from 0° (looking straight at the light) through 90° (looking perpendicular to the light). Intensity measurements are recorded as the angle is varied. The angle of the SSP was measured with a protractor. Care must be taken so the distance from the light source and the position of the center of the diffuser lens do not change as the SSP is rotated. Use the lines drawn in step 3 to keep the diffuser lens of the SSP in the proper position as it rotated.

9. Measurements were recorded every degree from 0° through 5°, then every 5° from 5° through 80°. Measurements between 0° are 5° important to define the forward transmission lobe for the NIR wavelengths.

B.4 Detector Response, Narrow Field of View Channels

This is the most critical part of the calibration. Equipment setup for this exercise is illustrated in Figure 3.17. This exercise was conducted in a large room. The radiance measured by a channel must be related to the radiance measured by the same channel at a different gain setting and to the radiance measured by the other channels at the same and different gain settings. To increase the accuracy of the intensity relationships all three NFOV channels detectors were calibrated at the same time. This introduces slightly different geometry for each channel. The measurements in Figure 3.17 are shown for the center of the SSP. Exact angles and distances must be calculated for each channel of the SSP.

B.4.1 NFOV Detector Response Measurement Procedure

1. Level table and leveling bench.

2. Set the SSP on the leveling bench, position and alignment are not critical.

3. Set the laser on a second table. Level the laser and adjust its height to the height of the center of the SSP.

4. Shoot the laser towards the lambertian plate. The lambertian plate worked just as advertised, the laser bean was reflected evenly in all directions. To align the lambertian plate, attach a plexiglass triangle to its front. Put a piece of tape on the back of the triangle where the laser bean hits. The laser beam will be reflected for aligning the equipment.

5. Adjust the height and position of the lambertian plate so the laser beam hits the center of the plate and then reflects from the plexiglass triangle towards the SSP.

6. Adjust the SSP position so the laser beam reflected from the lambertian plate hits it in the center. Align the SSP, by putting a second plexiglass triangle on the front of the SSP and reflect the laser beam along its incident path.

7. Measure the angles and distances between the center of the lambertian plate and SSP. Also measure the angle between the lambertian plate and laser.

8. Adjust the source lamp height and position so the laser hits the center of the element.

9. Measure the distance between the light source and the center of the lambertian plate.

10. Turn off the laser.

11. Measure the signal received by the SSP at each gain setting used to collect solar data.

Appendix C

DIFFUSER TRANSMISSION CURVES

Diffuser transmission curve parameters for the equation:

$$\frac{Receiver\,Power(\theta)}{Received\,Power(\theta=0)} = a\theta^2 + b\theta + c + d(exp[-e\theta]) \qquad (C.1)$$

Table C.1: Diffuser transmission coefficients for equation C-1.

Hole	Wavelength (nm)	a	b	c	d	e
81	509.00	-1.55E-04	1.07E-03	8.94E-01	0	0
82	521.50	-1.43E-04	-1.50E-03	9.48E-01	0	0
83	535.00	-1.25E-04	-1.42E-03	9.28E-01	0	0
84	548.00	-1.40E-04	-1.17E-03	9.82E-01	0	0
85	561.00	-1.33E-04	-1.45E-03	9.49E-01	0	0
86	575.00	-1.35E-04	-1.54E-03	9.76E-01	0	0
87	588.00	-1.34E-04	-1.71E-03	9.90E-01	0	0
88	601.00	-1.33E-04	-1.79E-03	9.90E-01	0	0
89	614.00	-1.32E-04	-1.94E-03	9.91E-01	0	0
90	627.00	-1.37E-04	-1.86E-03	1.00E+00	0	0
91	650.00	-1.31E-04	-2.21E-03	9.99E-01	0	0
92	673.00	-1.26E-04	-2.79E-03	1.00E+00	0	0
93	696.00	-1.20E-04	-3.26E-03	9.99E-01	0	0
94	718.00	-1.18E-04	-3.45E-03	1.00E+00	0	0
95	740.00	-1.18E-04	-3.53E-03	9.86E-01	0	0
68	664.00	-1.20E-04	-2.94E-03	9.97E-01	0	0
67	687.00	-1.28E-04	-2.94E-03	1.00E+00	0	0
66	712.50	-1.23E-04	-3.19E-03	1.01E+00	0	0

Table C.1 (cont)

Hole	Wavelength (nm)	a	b	c	d	e
65	737.50	-1.16E-04	-3.42E-03	9.84E-01	1.32E-02	0.90
64	761.50	-1.07E-04	-3.79E-03	9.54E-01	4.43E-02	0.90
63	788.50	-9.84E-05	-3.76E-03	9.00E-01	1.01E-01	0.90
62	814.50	-8.53E-05	-3.70E-03	8.17E-01	1.89E-01	0.90
61	842.00	-7.15E-05	-3.39E-03	7.04E-01	3.08E-01	0.90
60	867.00	-5.68E-05	-3.02E-03	5.83E-01	4.34E-01	0.90
59	892.00	-4.26E-05	-2.64E-03	4.70E-01	5.56E-01	0.90
58	918.00	-3.15E-05	-2.18E-03	3.62E-01	6.71E-01	0.90
57	944.00	-2.25E-05	-1.82E-03	2.81E-01	7.60E-01	0.90
56	971.00	-2.47E-05	-6.40E-04	1.99E-01	8.41E-01	0.80
55	993.00	-1.94E-05	-4.58E-04	1.52E-01	8.97E-01	0.80
54	1019.00	-1.35E-05	-5.51E-04	1.25E-01	9.37E-01	0.80
53	1041.00	-7.32E-06	-8.07E-04	1.09E-01	9.68E-01	0.80
52	1077.00	-1.77E-05	5.42E-04	6.36E-02	1.01E+00	0.70
51	1104.00	-1.62E-05	6.36E-04	4.89E-02	1.03E+00	0.70
50	1129.00	-1.20E-05	3.60E-04	4.63E-02	1.04E+00	0.70
49	1154.00	-1.41E-05	6.89E-04	3.78E-02	1.08E+00	0.65